THE UNIVERSITY OF CHICAGO

FINITE-AMPLITUDE LOCAL WAVE ACTIVITY AS A DIAGNOSTIC OF ANOMALOUS WEATHER EVENTS

A DISSERTATION SUBMITTED TO
THE FACULTY OF THE DIVISION OF THE PHYSICAL SCIENCES
IN CANDIDACY FOR THE DEGREE OF
DOCTOR OF PHILOSOPHY

DEPARTMENT OF THE GEOPHYSICAL SCIENCES

BY
SHAO YING HUANG

CHICAGO, ILLINOIS
DECEMBER 2017

To my parents, Ching-Wei Huang and Maria Suet-Ching Chong.

TABLE OF CONTENTS

LIST OF FIGURES

LIST OF TABLES

ACKNOWLEDGMENTS

First of all, I want to thank my supervisor Prof. Noboru Nakamura, who has given me great research ideas and unconditionally devoted a substantial amount of time to mentor me, both scientifically and personally. This thesis would not have existed without his guidance and support. I also want to express my gratitude to Prof. Tiffany Shaw, who has given insightful advice on my research work in these three years. I have learned a lot from the discussion with her. I would like to thank the rest of my advisory committee members: Prof. Malte Jansen, Prof. Dorian Abbot, and Prof. Douglas MacAyeal, who have given me valuable suggestions on my thesis, and have advised me on soft skills that are essential to academic success. I am grateful to my two former advisors, Prof. Raymond Pierrehumbert, who always brought up interesting research questions during our meetings and introduced me to the fun world of python programming, and Prof. Wendy Zhang, who gave me thought-provoking advice on how to communicate science.

This work would not have been possible without the help from the administrators in the Department of Geophysical Sciences. I especially want to thank David Taylor, who not only take care of my daily life in the department but also offer valuable advice personally at my difficult times. I also want to thank the system administrators, Thomas Indelli and Richard Dahringer, for setting up the coding environment for me to implement analyses smoothly.

Last but not least, I want to thank all my friends and my family for the company during my six years here. In particular, I want to thank Dr. Kit-Yan Choi, my guiding light since college times, for genuinely offering academic and technical advice. I also want to thank Dr. Levke Kööp, my best friend in the department, for getting my back throughout the years. Finally, I want to thank my parents, Ching-Wei Huang and Maria Suet-Ching Chong, for always being encouraging and supportive of my pursuit of academic career, my brother and good buddy Matthew Huang, and my partner in crime, Andy Li, who has been selflessly loving me, taking care of me, and helping me to be a better scholar and also a better person for nine years.

The research work presented in this thesis is support by the NSF grants AGS-1151790 and AGS-1563307.

ABSTRACT

Localized large-amplitude Rossby wave phenomena are often associated with adverse weather conditions in the midlatitudes. There has yet been a wave theory that can connect the evolution of extreme weather anomalies with the governing dynamical processes. This thesis provides a quasi-geostrophic framework for understanding the interaction between large-amplitude Rossby waves and the zonal flow on regional scales.

Central to the theory is finite-amplitude local wave activity (LWA), a longitude-dependent measure of amplitude and pseudomomentum density of Rossby waves, as a generalization of the finite-amplitude Rossby wave activity (FAWA) developed by Nakamura and collaborators. The budget of LWA preserves the familiar structure of the Transformed Eulerian Mean (TEM) formalism, and it is more succinct and interpretable compared with other existing wave metrics. LWA also captures individual large-amplitude events more faithfully than most other detection methods.

The bulk of the thesis concerns how the budget of wave activity may be closed with data when Rossby waves attain large amplitude and break, and how one interprets the budget. This includes the FAWA budget in a numerical simulation of barotropic decay on a sphere and the column budget of LWA in the storm track regions of the winter Northern Hemisphere with reanalysis data. The latter reveals subtle differences in the budget components between the Pacific and Atlantic storm tracks. Spectral analysis of the LWA budget also reveals the importance of the zonal LWA flux convergence and nonconservative LWA sources in synoptic- to intraseasonal timescales.

The thesis concludes by introducing a promising recent development on the mechanistic understanding of the onset of atmospheric blocking using the LWA framework.

CHAPTER 1

INTRODUCTION

1.1 Background

The migrations of cyclones and anticyclones along the jet streams govern the variations of local weather in the midlatitudes. They are responsible for the redistribution of momentum, energy, and moisture across latitudes and longitudes. Wavy jet streams are associated with extreme heat and moisture transport across latitudes. The dynamics of large-scale vortices have been understood in terms of wave theories, which are constructed by decomposing the fluid motions into a mean state and disturbance (known as waves or eddies). These large-scale waves in the midlatitudes are known as Rossby waves. Rossby waves are generated by orographic and thermal forcing at the surface or through baroclinic instability of the flow. They could be understood as perturbation of the flow under conservation of potential vorticity (PV), a materially conserved measure of both stratification and rotation of the fluid. Formulating fluid dynamics into a framework of wave-mean flow interaction not only provides an illuminative picture to understand fluid motions, but also, more importantly, provides a diagnostic framework to quantify the impact of eddies in terms of transfer of wave momentum. The formulation of a wave theory that precisely describes and diagnoses fluid motions has been an active research area.

To diagnose the evolution of waves, it is insightful to look into quantities that obey a conservation relation, or budget equation, such that one can evaluate what processes contribute to their growth and decay. For eddies that are generated through baroclinic instability, one candidate is the energetics of waves, wherein eddies grow by tapping into the available potential energy of the mean flow and the available eddy potential energy is converted to eddy kinetic energy (EKE). For example, to study the life cycle of a cyclone wave in the Southern Hemisphere, Orlanski and Katzfey (1991) derived the EKE budget in terms of horizontal velocity field $\mathbf{u}$, three-dimensional velocity field $\mathbf{v}$, ageostrophic wind

component $\mathbf{v}_a$, geopotential height Φ, vertical velocity in pressure coordinate $\omega = dp/dt$, and specific volume α:

$$\underbrace{\frac{\partial}{\partial t}\mathrm{K}}_{\substack{\text{EKE tendency}}} \approx \underbrace{-\nabla\cdot(\mathbf{u}K+\mathbf{v}_a\Phi^*)}_{\substack{\text{convergence}\\ \text{of total}\\ \text{energy flux}}} - \underbrace{\omega^*\alpha^*}_{\substack{\text{baroclinic}\\ \text{conversion}}} \underbrace{-\mathbf{u}\cdot(\mathbf{v}\cdot\nabla_3)[\mathbf{u}]}_{\substack{\text{barotropic}\\ \text{conversion}}}$$

$$+ \underbrace{\mathbf{u}^*\cdot[\mathbf{v}^*\cdot\nabla_3]\,\mathbf{u}^*}_{\substack{\text{barotropic conversion}\\ \text{between EKE and}\\ \text{trasient KE}}} - \underbrace{\frac{\partial}{\partial p}(\omega K)}_{\substack{\text{convergence of}\\ \text{vertical advective flux}\\ \text{of EKE}}} - \underbrace{\frac{\partial}{\partial p}(\omega^*\Phi^*)}_{\substack{\text{convergence of}\\ \text{vertical energy flux}\\ \text{associated with}\\ \text{pressure work}}} + \underbrace{\mathrm{RES}}_{\substack{\text{residual}}} . \tag{1.1}$$

Here [...] denotes time-mean, and $(...)^*$ denotes the transient component. ∇ and ∇_3 respectively denote the two-dimensional (horizontal) and three-dimensional gradient operators. Note that due to the presence of the conversion terms, the domain average of EKE is not conserved even when discarding the boundary terms and residuals.

Another option is to directly work on the Ertel potential vorticity (PV)

$$q = (f\mathbf{k}+\nabla\times\mathbf{v})\cdot\frac{\nabla\theta}{\rho}, \tag{1.2}$$

where f is the Coriolis parameter, $\mathbf{k}$ is the unit vector pointing in the increasing height direction, $\nabla\times$ is the three-dimensional curl operator, θ is potential temperature, and ρ is the density of air. The evolution of q is governed by

$$\frac{Dq}{Dt} = S - D, \tag{1.3}$$

where $\frac{D}{Dt}$ is the material derivative, S and D denote source and sink of PV. The budget equation of PV (1.3) is relatively easy to interpret: PV is materially conserved under adiabatic ($S = 0$) and frictionless ($D = 0$) dynamics. It is especially suited to quantify the role of diabatic heating (embedded in S), compared to (1.1) where conversion terms complicate the budget. However, eddy PV at any given location is not a positive definite quantity and may vanish upon time-averaging. When using PV as a metric, it is common to construct composites of events with PV anomalies of the same sign, usually obtained from a Lagrangian feature tracking (e.g. tracking the point with local minimum/maximum PV) (Hodges, 1995, 1999; Hodges et al., 2003; Hoskins and Hodges, 2002, 2005). This kind of technique is often applied to track cyclones (instead of anticyclones). For example, Tamarin and Kaspi (2016, 2017) analyzed PV budget of composites of extratropical cyclones to understand the mechanisms contributing to poleward deflection of storm tracks. Tracking of anticyclones, especially the slow moving ones associated with atmospheric blocking, has also been implemented using the isentropic PV field (i.e. PV on a constant potential temperature surface) (Altenhoff et al., 2008) or potential temperature field on a constant PV surface (Pelly and Hoskins, 2003). These approaches are more empirical in the sense that the PV budget is not utilized.

A candidate that is positive definite (i.e. a measure of wave amplitude) and related to the PV is the Rossby wave activity, A, or (the negative of) pseudomomentum. The concept of wave activity in meteorology first appeared in Eliassen and Palm (1961), where they derived a momentum flux equation for steady, non-dissipative waves in a meridionally and vertically varying zonal-mean flow. Charney and Drazin (1961) showed that in the linear quasi-geostrophic (QG) dynamics, the Rossby wave activity is solely written in terms of PV. They also showed that the zonal mean flow is unaltered up to the second order in eddy amplitude if the wave is steady and conservative, which is known as the non-acceleration theorem. The Eliassen-Palm (E-P) relation states that the tendency of wave activity A is

given by the divergence of the E-P flux $\mathbf{F}$:

$$\frac{\partial A}{\partial t} + \frac{1}{\rho}\nabla \cdot \mathbf{F} = \mathcal{O}\left(\eta^3\right). \tag{1.4}$$

For QG flows,

$$A = \frac{\overline{q'^2}}{2\partial\bar{q}/\partial y}, \tag{1.5}$$

where $\overline{(...)}$ and $(...)'$ respectively represent zonal mean and eddy, q is quasi-geostrophic PV (QGPV) defined by

$$q \equiv f + \zeta + \frac{f}{\rho_0}\frac{\partial}{\partial z}\left(\rho_0 \frac{\theta - \tilde{\theta}}{\partial\tilde{\theta}/\partial z}\right), \tag{1.6}$$

y is the meridional direction, z is the pressure pseudo-height, ζ is relative vorticity, θ is potential temperature, $\tilde{\theta}(z,t)$ is the area-weighted spatial domain average of θ, and $\partial\tilde{\theta}/\partial z$ is static stability. $\mathbf{F}$ is the E-P flux density given by

$$\mathbf{F} \equiv \left(0, -\rho_0\overline{u'v'}, \rho_0 f_0 \frac{\overline{v'\theta'}}{\partial\theta_0/\partial z}\right), \tag{1.7}$$

u and v are the zonal and meridional wind velocities, f_0 and $\rho_0 \sim e^{-z/H}$ are respectively the constant Coriolis parameter and the background density, with H being the scale height of the atmosphere. In (1.4), $\mathcal{O}\left(\eta^3\right)$ represents the nonlinear terms of third-order or higher in eddy amplitude η. The alternate name pseudomomentum is given to A because it is related to the translational invariance of the basic state (as opposed to the symmetry of coordinate itself, which gives rise to the momentum conservation), namely the zonal mean in this case.

The relation (1.4) was generalized by Andrews and McIntyre (1976) to include forcing and dissipation together with the residual circulation, so the relative roles of the conservative (advective / adiabatic) and non-conservative (diffusive / diabatic) processes are clarified. The formalism is named the Transformed Eulerian Mean (TEM) (Andrews and McIntyre, 1976) and has been widely used in the climate community.

For baroclinic QG flows, the generalized E-P relation and the zonal wind equation read

$$\frac{\partial A}{\partial t} + \frac{1}{\rho_0}\nabla \cdot \mathbf{F} = \bar{S}_A + \mathcal{O}\left(\eta^3\right), \tag{1.8}$$

$$\frac{\partial \bar{u}}{\partial t} - \frac{1}{\rho_0}\nabla \cdot \mathbf{F} - f_0 \bar{v}^* = \bar{X}, \tag{1.9}$$

where $\bar{v}^*$ is the meridional residual circulation, X is the frictional force, S_A is the non-conservative source/sink of wave activity, and the E-P flux vector $\mathbf{F}$ is defined by (1.7).

For linear waves that satisfy a dispersion relation, $\mathbf{F} = \mathbf{c}_g A$ (Andrews and McIntyre, 1976), where $\mathbf{c}_g$ is the group velocity of the wave. Therefore, $\mathbf{F}$ represents the flux of Rossby wave activity (or *radiation stress* of the waves) and the E-P theorem (1.8) describes how wave packets are migrating under the influence of sources and sinks.

In the absence of non-conservative forces, by eliminating the E-P flux divergence from (1.9) and (1.8), one obtains

$$\left(\frac{\partial}{\partial t} + \bar{v}^* \frac{\partial}{\partial y}\right)(\bar{u} - f_0 y) - \bar{v}^* \frac{\partial \bar{u}}{\partial y} = -\frac{\partial A}{\partial t} + O(\eta^3). \tag{1.10}$$

With the small Rossby number assumption $|f_0| \gg |\partial \bar{u}/\partial y|$ and $|\partial A/\partial y|$, this is formally indistinguishable from

$$\left(\frac{\partial}{\partial t} + \bar{v}^* \frac{\partial}{\partial y}\right)(\bar{u} - f_0 y) = -\left(\frac{\partial}{\partial t} + \bar{v}^* \frac{\partial}{\partial y}\right) A + O(\eta^3). \tag{1.11}$$

Thus for a small-amplitude wave $O(\eta^3) \sim 0$, one sees that the absolute zonal velocity $\bar{u} - f_0 y$ is unchanged following the residual circulation $\bar{v}^*$ if wave activity A is also unchanged. This result is called the (TEM) non-acceleration theorem and serves as the action-reaction relation between the zonal-mean state and the Rossby wave field.

The linear (small-amplitude) assumption limits the use of wave activity A [(1.5)] to situations where the zonal mean PV gradient is positive definite and non-vanishing. In the real atmosphere, nonlinear wave phenomena such as wave breaking (i.e. overturning of the

PV contour) and blocking (i.e. reversal of westerlies by large-amplitude waves) often modify the mean PV gradient significantly such that the value of A may be poorly constrained. Figure 1.1 shows an example of a blocking event over the Pacific. The local meridional PV gradient changes sign within the structure (not shown). If the zonal mean PV gradient is close to vanishing or even changes sign, A will blow up. If A is defined locally instead of using the zonal mean, A will be ill-behaved locally as soon as the PV contour overturns. This will be demonstrated for a locally defined wave activity for transient eddies in Chapter 4.

As an eddy diagnostic, the wave activity budget (1.8) is simpler than the EKE budget (1.1) in that the (conservative) source term of wave activity A is a flux divergence, so the tendency of volume integral of A is given solely by the boundary E-P fluxes and non-conservative sources and sinks. This is not the case in (1.1), where there are conversion terms that contribute to the EKE budget even after domain integral. Yet, the wave activity formalism is only amenable to *zonal-mean* statistics and is not suitable to diagnose longitudinally localized phenomena. **In this thesis, a framework for a longitudinally varying wave activity for waves of arbitrary amplitude is developed and applied to diagnose synoptic events and their climatology in the Northern Hemisphere storm track regions.** I will give a brief review on previously developed wave activity formalisms beyond the TEM in Section 1.2, followed by a review of studies on finite-amplitude wave phenomena and how they are associated with extreme weather conditions in Section 1.3.

1.2 The development of wave activity theory

Besides the TEM formalism (Andrews and McIntyre, 1976), there has been a variety of formalisms based on slightly different assumptions.

Formalisms applicable to finite-amplitude waves include Andrews and McIntyre (1978), who introduced the Generalized Lagrangian Mean (GLM) formalism that does not rely on small-amplitude assumption. The GLM wave activity satisfies a flux relation and a non-acceleration theorem exactly without neglecting higher-order eddy terms. This formalism,

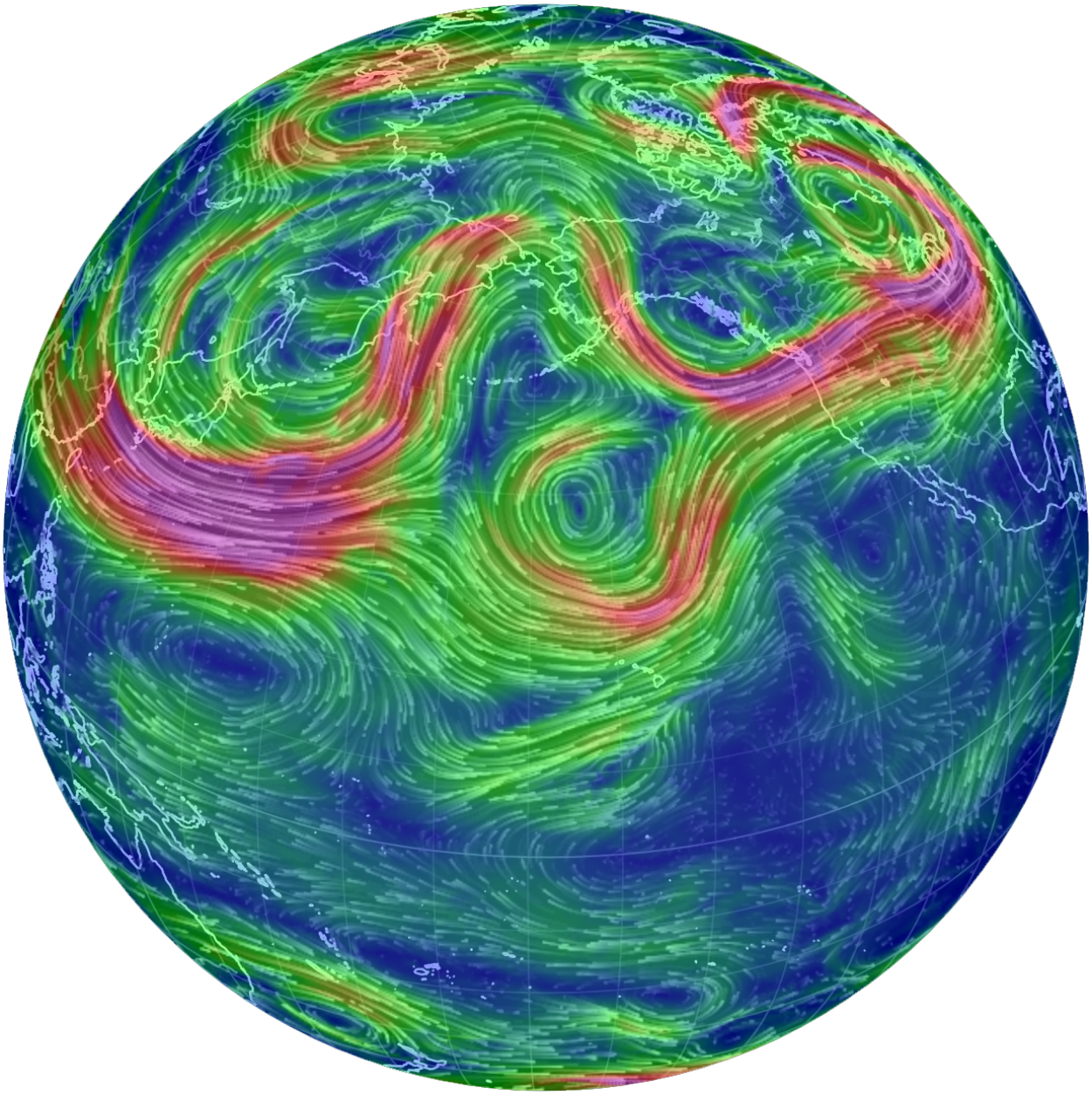

Figure 1.1: Color and white streaks: magnitude and direction of horizontal wind field at 500 hPa on Mar 8, 2017. There is a block over the Pacific that a stagnant dipole pattern with a high pressure cell formed to the north and low pressure cell to the south. The westerly flow between the two cells is reversed. Graphics retrieved from: http://earth.nullschool.net.

however, involves an averaging domain which evolves with the positions of the fluid parcels. This makes it impractical for application as parcel tracing in meteorological data is very difficult. As an alternative, an exact Eulerian formalism of wave activity in a 2D flow was introduced by Killworth and McIntyre (1985), where they combined Kelvin's impulse and

suitable functions of PV (Casimir invariants) to derive a form of wave activity with an arbitrary, steady zonally symmetric basic state. Haynes (1988) generalized the formalism to forced, dissipative flows with a zonally asymmetric basic state. This formalism has been rarely used compared to the TEM, likely because its computation being more complicated (though not as complicated as the GLM). Chapter 3 of this thesis will look into this Impulse-Casimir wave activity and highlight possible issues in interpretability that discourage its application to meteorological data, together with a proposal for a more attractive alternative.

More commonly used wave activity formalisms are extensions of the TEM, which do not focus on overcoming the small-amplitude assumption, but more on defining a meaningful 3D flux vector $\mathbf{F}$ that indicates the direction of wave propagation and its interaction with the mean flow. Hoskins et al. (1983) quantify the eddy feedback on the time-mean flow with an $\mathbf{E}$-vector that *approximates* the eddy vorticity flux for QG eddies, but it does not satisfy the E-P flux relation that relates to the conservation of wave activity. Plumb (1985) derived an E-P flux vector for stationary waves on the mean flow, while Plumb (1986) worked out the expression for transient QG eddies on a zonally asymmetric time-mean flow. In Plumb's work, there is phase dependence in the transient wave activity flux so the time-averaging is needed to eliminate it. Takaya and Nakamura (2001) used a combination of wave energy and pseudomomentum to arrive at a wave activity flux expression for stationary and migratory QG eddies that is phase independent.

Note that the choice of wave activity flux vector $\mathbf{F}$ is not unique due to the presence of gauge freedom in (1.4), such that any divergence-free vector added to $\mathbf{F}$ gives the same flux divergence. Different gauge leads to a different definition of wave activity density A particularly at finite amplitude. Solomon and Nakamura (2012) demonstrate that for a barotropic flow on a sphere, the TEM (Andrews and McIntyre, 1976), GLM (Andrews and McIntyre, 1978), and Impulse-Casimir wave activities (Killworth and McIntyre, 1985) are all related through gauge transformations.

The small-amplitude wave activity densities have various forms, but they all have the PV

gradient (either local or zonal-mean) in its denominator, so the value of A diverges whenever the PV gradient is close to vanishing, that is, when finite-amplitude wave phenomena take place. Because of this, only the wave activity flux has been used in diagnosing the flow. Previous meteorological studies have adopted widely the wave activity flux diagnostics but not the wave activity itself. In Chapters 2 and 4, I will demonstrate how small-amplitude wave activity directly evaluated with data tends to run into difficulties with a vanishing PV gradient when wave amplitude becomes large and how these difficulties may be avoided.

1.3 Understanding of finite-amplitude wave phenomena

As mentioned in the previous section, overturning of the PV contours (i.e. vanishing of local meridional PV gradient, $\partial q/\partial y = 0$) is referred to as Rossby wave breaking. In the troposphere, it may be associated with a blocking event if the feature is stagnant for a few days and the zonal wind, or the gradient of mid-tropospheric (500 hPa) geopotential height, is reversed. Note that the zonal mean PV gradient $\partial \bar{q}/\partial y$ can still be positive when the breaking wave is zonally confined. Blocking is associated with persistent heat/cold waves and drought (Sillmann et al., 2011; Schubert et al., 2014; Whan et al., 2016) while Rossby wave breaking is associated with extreme heat/moisture transport (Hanley and Caballero, 2012; Liu and Barnes, 2015). There has not been a clear distinction between wave breaking and blocking in the literature, but only remarks that they are closely associated with each other (Berrisford et al., 2007), or that Rossby wave breaking being part of the blocking process (Masato et al., 2012). Empirical detection methods have been proposed for Rossby wave breaking (Strong and Magnusdottir, 2008; Wernli and Sprenger, 2007; Barnes and Hartmann, 2012) and for blocking (Tibaldi and Molteni, 1990; Lejenäs and Økland, 1983; Pelly and Hoskins, 2003; Barriopedro et al., 2006) from meteorological data. Barnes et al. (2012) show that detecting blocking by searching for 500 hPa geopotential height (Z500) gradient reversal, zonal wind reversal and potential temperature reversal on 2 PVU surface are simply different ways of looking into the same physical process. Barnes et al. (2014) revealed the issues with the

arbitrariness of blocking indices by comparing detection methods based on Z500 gradient reversal with slightly different algorithms: they give inconsistent climatology and trends based on the same reanalysis dataset. The lack of an objective metric for the generators of extreme weather makes the comparison of model simulation output difficult. It would be useful to characterize Rossby wave breaking (and other finite-amplitude phenomena) using a fundamental quantity that drives it.

1.3.1 Rossby wave breaking and the critical line theory

To understand wave breaking, one needs to move past the small-amplitude (linear) theory. Linear wave theory predicts its own breakdown when a monochromatic wave with phase speed c propagates into a latitude and height at which $\bar{u}(\phi, z) = c$, or the critical line. The wave becomes stagnant and wave activity accumulates into a critical layer, the region surrounding the critical line. The work of Dickinson (1970) and a follow-up study by Warn and Warn (1976) for a barotropic Rossby wave showed that under the long-wave approximation and assuming that the waves are steady, linear and conservative, the critical layer is a perfect absorber of eddy momentum flux within a time scale given by the inverse square root of the forced wave amplitude. Beyond this time scale, the dynamics becomes highly nonlinear. An exact, nonlinear "Kelvin's cat's eye" solution of the critical layer beyond this time scale is given by Stewartson (1977) and Warn and Warn (1978) (SWW). They studied the dynamics of Rossby wave breaking by solving the barotropic vorticity equation for a two-dimensional incompressible flow on a beta-plane, providing a self-consistent and complete analytical solution for Rossby wave critical layer in an inviscid medium. This nonlinear solution has provided a quantitative description of the development of critical layer out to a very large time, when linear theory breaks down and numerical methods fail due to the exponentially large vorticity gradients that develop on exponentially small scales (Killworth and McIntyre, 1985). Moreover, it resembles wave breaking observed by McIntyre and Palmer (1983) and McIntyre and Palmer (1984) in the isentropic PV maps of the stratosphere, including

the rapid and irreversible deformation of material lines. The critical layer theory may thus provide a useful idealization of planetary wave breaking.

Later studies show that finite-amplitude waves can actually break without reaching the critical line or even without a pre-existing critical line at all. A numerical study by Feldstein and Held (1989) on a two-layer QG model showed that waves can break far from the critical latitude when the wave amplitude is large, suggesting that the critical latitude is not an essential element of finite-amplitude wave breaking. Fyfe and Held (1990) studied a two-dimensional nondivergent Rossby wave propagating meridionally through a shear flow that has no critical line. They derived a predictive criterion for the onset of wave breaking in a quasi-linear framework, and showed that the wave breaks before the criterion is satisfied when the prescribed forcing has amplitude beyond quasi-linear limit. The critical line therefore only predicts where waves of *infinitesimally small amplitude* break.

1.3.2 The Wave-mean flow interaction and the PV mixing

The interaction between breaking waves and the mean flow is qualitatively encapsulated in (1.8) and (1.9) for small-amplitude waves, but it can also be understood in terms of PV 'mixing' (in this context, mixing does not necessarily mean diffusive mixing but simply exchange across latitudes) discussed by Dritschel and McIntyre (2008). The transport of angular momentum by large-scale waves can be described in terms of spatially inhomogeneous rearrangement of PV across its background gradient. The resultant change in the zonal flow may be inferred from the *invertibility relation* between PV and the streamfunction under suitable balance. Rossby waves 'exchange' PV across latitudes such that the eddy vorticity flux $\overline{v'q'} < 0$ in their growing phase (see Fig.1.2). Through Taylor's identity (Taylor, 1932; Bretherton, 1966)

$$\overline{v'q'} = \frac{1}{\rho_0}\nabla \cdot \mathbf{F}, \tag{1.12}$$

therefore $\overline{v'q'} < 0$ implies a convergence of E-P flux, and thus the zonal-mean zonal wind is decelerated according to (1.9). When the rearrangement of PV is localized meridionally, PV gradients are enhanced at the edges of this 'mixing region', which, through the invertibility principle, causes the zonal jet to be displaced and sharpened. This idea is illustrated in the modeling work of McIntyre (1982), who studies the effect of the stratospheric wave breaking on polar night jets. The PV mixing picture is a heuristic description of how the mean flow and the homogenization of PV shape each other. The finite-amplitude wave activity formalism by Nakamura and collaborators that I will present in the next section provides a quantitative framework to understand such phenomena by **extending the definition of wave activity to include finite-amplitude, potentially breaking, Rossby waves.** It generalizes the non-acceleration theorem to waves of arbitrary amplitude, so that the deceleration and sharpening of the jet core can be quantified in terms of the growth of finite-amplitude wave activity.

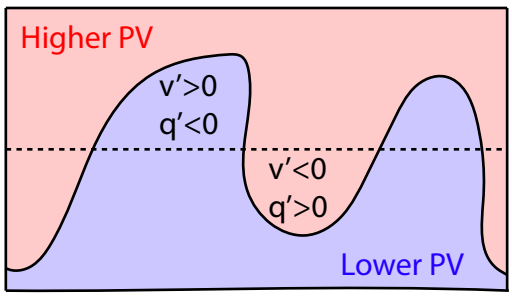

Figure 1.2: Schematic diagram of Rossby waves 'mixing' (or exchanging meridionally) PV on the longitude-latitude plane. Fluid parcels with higher PV (red) are transported equatorward, while those with lower PV are transported poleward across the latitude circle (dashed line) as the amplitude of the Rossby waves grows. In both cases, the local $v'q'$ and also its zonal mean are negative.

1.4 Review of finite-amplitude wave activity formalism by Nakamura and collaborators

The finite-amplitude wave activity (FAWA) diagnostic developed by Nakamura and collaborators is designed to extend the TEM formalism to finite-amplitude waves and QG eddies.

It is based on the facts that: (1) advection (reversible arrangement by 2D nondivergent flow) conserves PV and area, and (2) small-scale mixing homogenizes PV irreversibly.

1.4.1 Equivalent latitude

To describe the evolution of finite-amplitude wave fronts, a Lagrangian coordinate based on the contours of QGPV (1.6) (or possibly other quasi-conservative tracers, depending on the application) will be used. For convenience, it is converted to equivalent latitude (Butchart and Remsberg, 1986; Allen and Nakamura, 2003). Given a 2D spatial distribution of PV field as a function of longitude λ and latitude ϕ, for each contour of $q(\lambda, \phi) = Q$, where $q_{min} \leq Q \leq q_{max}$, there is a circle of latitude at ϕ that encloses the same area to the north as the contour. This latitude ϕ is the equivalent latitude of the PV value $q = Q$ (see Figs. 1.3a and b below). The contour can be multiply connected, in which case summation is taken for all closed elements. Given that the region enclosed by the contour of value Q contains PV in the range $Q < q \leq q_{max}$, the relationship $Q(\phi)$, or the equivalent latitude $\phi(Q)$, is a **monotonically increasing** function. The equivalent latitude $\phi(Q)$ is a time invariant to the extent that PV advected by the nondivergent 2D flow is material, i.e., the RHS of (1.3) is zero, since a 2D nondivergent flow is area-preserving. Therefore, the change in $\phi(Q)$ quantifies how irreversible mixing and other non-conservative processes modify the PV distribution.

1.4.2 Effective diffusivity

A related quantity is effective diffusivity K_{eff} (Nakamura, 1996) that measures microscale diffusion magnified by stirring. Physically, it measures the geometrical complexity of the tracer contour. A contour of a purely advective tracer is a material line. For a tracer under advection and diffusion, the movement of the tracer contour is an advective (reversible, at least in principle) process, while the material exchange across the contour is diffusive (irreversible mixing). As the tracer is stirred by large-scale eddies, a more deformed contour

gives a larger 'cross-section' for material exchange through diffusion. Effective diffusivity is a measure of the ratio of the square of equivalent length of the tracer contour (which can be multiply connected) to its lower bound (i.e. square of the minimum length). The specific form of $K_{\rm eff}$ depends on the way small-scale mixing is represented, and I will discuss this in more detail in Chapter 2. $K_{\rm eff}(\phi, z, t)$ quantifies the effect of irreversible mixing, and it is connected to the change in tracer in equivalent latitude by

$$\frac{\partial Q}{\partial t} = \frac{1}{a^2 \cos\phi} \frac{\partial}{\partial \phi} \left(K_{\rm eff}(\phi, z, t) \cos\phi \frac{\partial Q}{\partial \phi} \right) \tag{1.13}$$

Note that (1.13) is a purely diffusive equation (Nakamura, 1996): the role of advection (stirring) is absorbed in the behavior of $K_{\rm eff}$.

1.4.3 Finite-amplitude wave activity (FAWA)

Finite-amplitude wave activity (FAWA) $A^*(\phi, z, t)$ is defined on the equivalent latitude $\phi(Q)$ as the difference of surface integrals of q over the red and blue regions in Fig.1.3 divided by the length of the latitude circle:

$$A^*(\phi, z, t) \equiv \frac{1}{2\pi a \cos\phi} \left[\iint_{S_{red}} q dA - \iint_{S_{blue}} q dA \right]. \tag{1.14}$$

It is easily verified that the bracket on the RHS of (1.14) equals the difference of the surface integrals over the red and blue lobes in Fig.1.3c. Since PV in the red lobes is everywhere higher than PV in the blue lobes, A^* is always positive definite. Nakamura and Solomon (2010) demonstrate that A^* approaches the linear wave activity A in the small-amplitude limit.

To start deriving the governing equation of FAWA, consider a simpler problem of non-divergent barotropic flow on a sphere. In this case, q is reduced to absolute vorticity. In adiabatic and frictionless 2D barotropic flows, q is materially conserved [i.e.(1.3)] and thus Kelvin's circulation theorem is obeyed, namely, the line integral of absolute velocity $\mathbf{u}_A$ along

a closed q contour $q = Q$ is conserved:

$$\frac{\mathrm{d}}{\mathrm{d}t} \oint_{q=Q} \mathbf{u}_A \cdot d\mathbf{l} = 0, \tag{1.15}$$

where $\mathbf{u}_A = (\Omega a \cos\phi' + u, v, 0)$ and Ω, a, and ϕ' are Earth's rotation rate, radius, and latitude, respectively. In Fig.1.3a below, this contour is the curve enclosing the red region. Again the curve can be multiply connected.

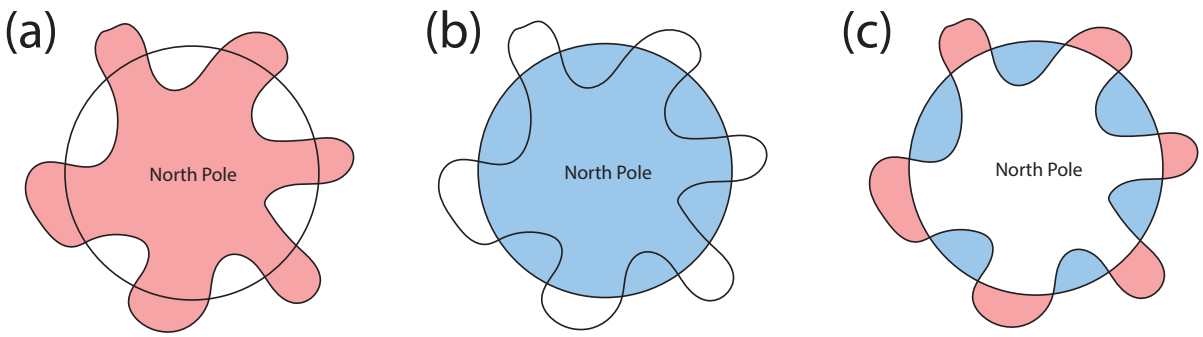

Figure 1.3: Schematics of calculating FAWA

By the Stokes theorem, (1.15) can be rewritten as

$$\frac{\mathrm{d}}{\mathrm{d}t} \iint_{S_{red}} (f\mathbf{k} + \nabla \times \mathbf{u}) \cdot \mathbf{k} dA = \frac{\mathrm{d}}{\mathrm{d}t} \iint_{S_{red}} q dA = 0, \tag{1.16}$$

where $f = 2\Omega \sin\phi$, $\mathbf{k}$ is the unit vertical vector, $\mathbf{u} = (u, v, 0)$, and S_{red} is the area bounded by the closed curve $q = Q$. The surface integral of q within the latitude circle $\phi(Q)$, by the Stokes theorem, satisfies

$$\iint_{S_{blue}} q dA = \iint_{S_{blue}} (f\mathbf{k} + \nabla \times \mathbf{u}) \cdot \mathbf{k} dA = \oint_{C_{blue}} \mathbf{u}_A \cdot d\mathbf{l} = 2\pi a \cos\phi(\bar{u} + \Omega a \cos\phi), \tag{1.17}$$

where ϕ is the equivalent latitude at which the enclosing circle is located.

Because of (1.16) and (1.17), the time derivative of (1.14) leads to the non-acceleration

relation *without small amplitude assumption*:

$$\frac{\partial}{\partial t}\left(\bar{u}+A^{*}\right)=\frac{1}{2\pi a\cos\phi}\frac{\mathrm{d}}{\mathrm{d}t}\iint_{S_{red}}qdA=0, \tag{1.18}$$

where the partial derivative on the LHS is performed at a fixed equivalent latitude. (The material derivative on the RHS emphasizes the contour-following operation, but since the area enclosed by the contour is unchanged, it is actually still done on a fixed equivalent latitude.) Note that in the barotropic flow the residual circulation $\bar{v}^{*}$ in (1.11) vanishes. Therefore, (1.11) and (1.18) become identical except that the latter does not have the extra $\mathcal{O}\left(\eta^{3}\right)$ term. As a result of (1.18), a reference state of zonal wind u_{REF}, namely, a hypothetical zonal wind when all eddies are removed conservatively, can be defined:

$$u_{\mathrm{REF}}(\phi)=\bar{u}(\phi,t)+A^{*}(\phi,t). \tag{1.19}$$

u_{REF} is a time-invariant under conservative dynamics. Equation (1.19) essentially represents the partitioning of circulation into angular momentum and wave activity. Since u_{REF} is conserved, any increase in A^{*} must be compensated by a decrease in the zonal mean flow by the same amount and vice versa.

For baroclinic QG eddies, FAWA satisfies the E-P relation (1.8) with $\mathbf{F}$ defined in (1.7), but without the cubic eddy term:

$$\frac{\partial A}{\partial t}+\frac{1}{\rho_{0}}\nabla\cdot\mathbf{F}=S_{A}. \tag{1.20}$$

Note also that the RHS term is evaluated as an average over the red and blue lobes in Fig.1.3c (Nakamura and Zhu, 2010). Using (1.9) and (1.20), together with the continuity and thermodynamic equations, one can obtain the non-acceleration relation (in the absence of non-conservative processes). In spherical coordinates this reads (Nakamura and Solomon,

2010):

$$\frac{\partial}{\partial t}\left[\frac{\partial^2}{\partial \mu^2}\frac{(\bar{u}_g + A^*)\cos\phi}{f} + \frac{1}{\rho_0}\frac{\partial}{\partial z}\left(\rho_0 \epsilon \frac{\partial}{\partial z}\frac{\bar{u}_g \cos\phi}{f}\right)\right] = 0, \tag{1.21}$$

where $\mu \equiv \sin\phi$, $\bar{u}_g$ is the geostrophic zonal-mean zonal wind, $\epsilon \equiv \frac{4\Omega^2 \mu^2 a^2 H e^{\kappa z/H}}{R(1-\mu^2)\partial\tilde{\theta}/\partial z}$. Here $\kappa = R/c_p$, where R is gas constant, c_p is specific heat at constant pressure, H is the scale height, Ω is the rotation rate of the planet. An eddy-free reference state analogous to (1.19) can be defined by:

$$\frac{\partial^2}{\partial \mu^2}\frac{u_{\mathrm{REF}}\cos\phi}{f} + \frac{1}{\rho_0}\frac{\partial}{\partial z}\left(\rho_0 \epsilon \frac{\partial}{\partial z}\frac{u_{\mathrm{REF}}\cos\phi}{f}\right) \equiv \frac{\partial^2}{\partial \mu^2}\frac{(\bar{u}_g + A^*)\cos\phi}{f} + \frac{1}{\rho_0}\frac{\partial}{\partial z}\left(\rho_0 \epsilon \frac{\partial}{\partial z}\frac{\bar{u}_g \cos\phi}{f}\right). \tag{1.22}$$

Nakamura and Zhu (2010) and Nakamura and Solomon (2011) show that the RHS of (1.22) is closely related to the meridional PV gradient in equivalent latitude, $\frac{\partial Q}{\partial \phi}$. Therefore, $u_{\mathrm{REF}}(\phi, z, t)$ may be obtained by numerically inverting the equation with suitable boundary conditions, just as $\bar{u}_g$ may be inverted from the meridional gradient of the zonal-mean PV $\bar{q}$. It is necessary to solve these elliptic equations to compute the response of the zonal-mean flow to FAWA or the structure of the reference state, since wave forcing in the meridional plane has a nonlocal influence through the wave-induced residual circulation.

When there are non-conservative processes, the RHS of the E-P relation (1.20) is nonzero. Nakamura and Zhu (2010) show that when there is small-scale turbulent mixing of PV, the RHS of (1.20) is dominated by the diffusive flux of PV driven by effective diffusivity, which acts as a sink of wave activity. In this case u_{REF} is no longer conserved but slowly responds to the mixing of PV. This will be demonstrated in a numerical experiment in Chapter 2.

FAWA has proven to be a suitable diagnostic for wave breaking events that take place *globally* and do not have a longitudinal preference. For example, Solomon (2014) uses the characteristics of evolution in FAWA to classify sudden stratospheric warming events. Wang and Nakamura (2015, 2016) study the 25-day cycle of eddy activity over the Southern Ocean using the FAWA budget.

1.5 Scope and goals of this thesis

The Northern Hemisphere is covered by more continental masses with human activities compared to the Southern Hemisphere. This introduces strong longitudinal variation in the boundary conditions, and as a result, weather statistics of the Northern Hemisphere is zonally inhomogeneous. For example, storm activities are organized into Atlantic and Pacific storm tracks. Frequency of large wave events such as blocking also shows preferred longitudes. To quantify and understand these phenomena with marked regional characteristics, a longitude-dependent metric that has a well-constrained value is needed. The goal of this thesis is to generalize the FAWA formalism discussed above to be a function of longitude, so it can be used to study localized nonlinear wave phenomena such as wave breaking (associated with extreme moisture transport), or blocking, which is often associated with heat waves. The main goal will be the **local** budget analysis, at least on the conservative part of the local wave activity evolution, which was not feasible with previous wave activity formalisms. I will outline in detail the theoretical framework of the local finite-amplitude wave diagnostic, and practically how this can be applied to gridded climate data.

Note that the scope of this thesis is confined to the baroclinic QG flow. Only results in the midlatitudes, where the QG approximation being valid, will be analyzed and interpreted. No attempt is made to generalize the diagnostic beyond the domain of validity of QG approximation. Moreover, as a first step to understand the atmospheric dynamics using the local wave activity formalism, when looking into reanalysis data, only the barotropic component of the budget is studied. Layer-by-layer analysis will be deferred to future work.

1.6 Thesis outline

This thesis develops a framework for using finite-amplitude local Rossby wave activity (LWA) and its flux equation to understand the regional behaviors of Rossby wave packets.

Before addressing longitudinal variation in the Rossby wave packets, I will start in Chap-

ter 2 by comparing FAWA to the linear Rossby wave activity / pseudomomentum (Andrews and McIntyre, 1976) in a numerical simulation of *barotropic decay* in a shear flow. This shows how the finite-amplitude formalism overcomes the inadequacy of the linear formalism. Although the linear wave activity and FAWA converge at small amplitudes, only FAWA remains well-behaved when the zonal-mean vorticity gradient is reversed whereas its linear counterpart breaks down. The budget of FAWA is demonstrably closed with the meridional eddy momentum flux convergence and the diffusive flux of vorticity. The simulation also demonstrates the limitation of the linear critical line theory in predicting the latitudes of wave breaking, and how the quasi-invariant eddy-free reference state constrains the evolution of waves.

Chapter 3 generalizes FAWA and its fluxes as functions of longitude, that is, I introduce the LWA. The LWA expression and its flux equation will be compared with the exact Impulse-Casimir wave activity (ICWA) flux relation from Killworth and McIntyre (1985). It will be demonstrated that LWA attains maxima at locations with a vorticity gradient reversal, while ICWA vanishes there. Furthermore, an approximate local non-acceleration theorem holds for LWA but not for ICWA. A blocking episode over the Atlantic is examined in terms of the covariation of barotropic zonal wind and LWA to test the validity of the local non-acceleration relation.

Chapter 4 demonstrates the application of the barotropic LWA budget to analyze meteorological data. The LWA budgets over the Pacific and Atlantic Oceans in reanalysis data are examined in terms of spatial distribution in the winter climatology as well as the term-by-term spectra in the frequency domain. The LWA budget terms differ significantly between the two regions in seasonal climatology. Relative importance of the wave activity flux terms over synoptic to intraseasonal timescales is revealed in the co-spectral analyses. The importance of the zonal component of the LWA flux is emphasized.

The final chapter summarizes the preceding results and outlines the onset mechanisms of atmospheric blocking as a promising area of application of the proposed analysis framework.

This thesis enables budget analyses using both wave activity and its flux divergence on waves of arbitrary amplitudes and geometry, which was not feasible with the previously developed wave theories.

Chapter 2 is based on the unpublished poster presentation at the AMS 19th AOFD Conference (2013) at Newport, RI. Chapter 3 is based on Huang and Nakamura (2016). Chapter 4 is based on Huang and Nakamura (2017). Chapter 5 contains some preliminary analysis as well as the results from Nakamura and Huang (2017).

CHAPTER 2

BUDGET OF FINITE-AMPLITUDE WAVE ACTIVITY IN A BAROTROPIC DECAY MODEL

2.1 Introduction

Atmospheric Rossby waves propagate both horizontally and vertically from regions where they are generated. In the upper troposphere, during their horizontal propagation, the Rossby waves can grow in amplitude, break, and eventually disintegrate irreversibly into turbulence. Simultaneously, the zonal wind is decelerated according to the non-acceleration theorem [(1.18) and (1.21)], and this disrupts the migration of the waves and weather systems. As discussed in Section 1.1, early linear wave theory, derived on the small-amplitude assumption, has provided a framework to understand the Rossby waves and their interactions with the zonal mean flow, as well as their group propagation through the E-P flux vectors (Andrews and McIntyre, 1976). However, such formalism only addresses the dynamics of waves when they are of small amplitude (i.e. linear).

Understanding of finite-amplitude Rossby waves (e.g. when waves grow in amplitude and break) with the linear theory is rather limited. The Wentzel-Kramers-Brillouin (WKB) approximation predicts that as a monochromatic Rossby wave propagates in a slowly varying shear flow toward a critical line, where its phase speed equals the zonal mean flow, the meridional wave number l grows infinitely. Since this makes the meridional group velocity vanish, wave activity will pile up. Eventually the linear theory breaks down without nonlinear effects or dissipation (Dickinson, 1968; Lindzen and Tung, 1978). Randel and Held (1991) verified with meteorological data that the spectra of the eddy momentum flux (meridional component of the negative E-P flux) are indeed confined in the domain bounded by the line where zonal wind equals the phase speed. However, nonlinear numerical simulations show that waves can actually break **before** arriving at the critical lines, especially in the finite-amplitude scenarios. Therefore, the critical line is more of a heuristic measure of the

limit to which waves can propagate instead of a precise predictive measure.

The finite-amplitude Rossby wave activity (FAWA) theory introduced by Nakamura and Zhu (2010) (NZ10) provides a new framework to study nonlinear wave phenomena mentioned in Section 1.3. NZ10 derive an exact conservation law for finite-amplitude wave activity density applicable to Rossby waves and balanced eddies. More importantly, it provides a framework to precisely quantify both the impacts of advective transport (conservative arrangement) and irreversible dissipation due to mixing on the mean flow. Solomon and Nakamura (2012) compares the formalism of NZ10 with that of Killworth and McIntyre (1985) in a simple jet forcing numerical experiment and find that the domain averages of the two wave activities are consistent with each other but they differ locally. Yet, there has not been a study that demonstrates numerically how the budget of FAWA is closed in terms of the generalized E-P flux and dissipation due to mixing.

The goal of this chapter is to compare FAWA with the linear pseudomomentum in a simulation of barotropic decay in a shear flow and to illustrate how FAWA is well-behaved and bounded for finite-amplitude waves when linear theory breaks down. I also demonstrate the inadequacy of the critical line theory in that finite-amplitude waves break before reaching the critical latitude. More importantly, I demonstrate how the budget of FAWA can be closed using the E-P flux and effective diffusivity, which has not been demonstrated in any of the previous studies.

2.2 Small-amplitude wave activity theory in a barotropic flow

Consider a two-domensional (2D) barotropic flow on a Cartesian plane in a rotating frame with angular velocity $\Omega(y)$. In this case, PV is equivalent to absolute vorticity $\omega_a = 2\Omega + (\nabla \times \mathbf{v}) \cdot \hat{\mathbf{k}} = 2\Omega + \frac{\partial v}{\partial x} - \frac{\partial u}{\partial y}$ (where u is the zonal velocity and v is the meridional velocity). In the absence of non-conservative forces, the PV equation (1.3) may be linearized about the zonal-mean state [indicated by $\overline{(...)}$] to obtain the equation for the eddy PV q':

$$\frac{\partial q'}{\partial t} + \bar{u}\frac{\partial q'}{\partial x} + v'\frac{\partial \bar{q}}{\partial y} = \mathcal{O}\left(\eta^2\right), \tag{2.1}$$

where $q \equiv \bar{q} + q'$ and η denotes the eddy amplitude.

Multiplying (2.1) by q' and taking zonal average, one obtains the (linearized) eddy enstrophy equation:

$$\frac{1}{2}\frac{\partial \overline{q'}^2}{\partial t} + \overline{v'q'}\frac{\partial \bar{q}}{\partial y} = \mathcal{O}\left(\eta^3\right). \tag{2.2}$$

As mentioned in Chapter 1, global conservation and being sign-definite are two of the desirable properties for a wave diagnostic. Eddy enstrophy $\frac{1}{2}\overline{q'^2}$ is not globally conserved, although the total enstrophy $\frac{1}{2}\overline{q^2}$ is, as derived from (1.3) without the assumption of small-amplitude waves. Using the divergence-free property, multiplying (1.3) by q and integrate over a closed domain S with the condition that the boundary fluxes add up to zero, one obtains:

$$\begin{aligned} \frac{\partial q^2}{\partial t} + \nabla \cdot (\mathbf{u}q^2) &= 0, \\ \frac{\partial}{\partial t}\iint\limits_S q^2 dA + \iint\limits_S \nabla \cdot (\mathbf{u}q^2) dA &= 0, \\ \Rightarrow \frac{\partial}{\partial t}\iint\limits_S q^2 dA &= 0. \end{aligned} \tag{2.3}$$

I will illustrate in Chapter 3 with a realistic example why wave activity is a better metric than eddy enstrophy.

The equation for the linear wave activity A (1.4) becomes, for the barotropic flow,

$$\frac{\partial A}{\partial t} - \frac{\partial}{\partial y}\overline{u'v'} = \mathcal{O}\left(\eta^3\right). \tag{2.4}$$

where A is given by (1.5). Linear wave activity A, together with the zonal mean wind $\bar{u}$

satisfy the non-acceleration equation up to second order in eddy amplitude:

$$\begin{aligned}
&\frac{\partial A}{\partial t} - \frac{\partial}{\partial y}\overline{u'v'} = \mathcal{O}\left(\eta^3\right), \\
&\frac{\partial \bar{u}}{\partial t} + \frac{\partial}{\partial y}\overline{u'v'} = 0, \\
&\Rightarrow \frac{\partial A}{\partial t} + \frac{\partial \bar{u}}{\partial t} = \mathcal{O}\left(\eta^3\right).
\end{aligned} \tag{2.5}$$

Note that this barotropic result simplifies the baroclinic formula (1.11) since the residual circulation is zero.

The wave activity A could hardly be used to diagnose realistic Rossby waves. When the amplitude of wave is large and overturning of PV contours occurs over a significant portion of the zonal length of the domain, the PV gradient in the demonimator of (1.5) vanishes. A then diverges and its value becomes hard to interpret. In the next section, I will illustrate with outputs from an idealized simulation how FAWA described in Section 1.4 serves as a better diagnostic than (1.5).

In the next section, I will use the barotropic decay model in Held (1985) (H85) and Held and Phillipps (1987) (HP87) to demonstrate the application of the FAWA formalism and how it addresses the inadequacy of the linear theory in diagnosing the wave-mean flow interaction when wave amplitudes are beyond the small-amplitude regime.

2.3 Barotropic decay in a shear flow on a sphere

2.3.1 Model setup

The barotropic decay problem studied by H85 and HP87 is an initial value problem for which the governing barotropic vorticity equation (BVE) reads:

$$\frac{\partial \zeta}{\partial t} + J(\psi, f + \zeta) = -\nu \nabla^4 \zeta, \tag{2.6}$$

where $f = 2\Omega \sin\phi$ is the Coriolis parameter, ζ is relative vorticity, J is Jacobian, ψ is streamfunction and ν is hyperviscosity, which I choose to damp the shortest resolved wave by a factor of 1/48 daily. The viscosity term artificially removes the small-scale filaments generated in wave breaking events. This is the only non-conservative mechanism in the model.

The initial zonal-mean flow is prescribed as in HP87:

$$\bar{u}(\phi, t=0) = 25\cos\phi - 30\cos^3\phi + 300\sin^2\phi\cos^6\phi, \tag{2.7}$$

which mimics the zonal-mean wind in the upper troposphere with westerlies in the mid-latitudes and an easterly at the equator. In addition, a gaussian wave packet meridionally centered at $\phi_m = 45°$N with zonal wavenumber $m = 6$

$$\zeta' = \zeta_\circ e^{-\left[\frac{\phi-\phi_m}{\sigma}\right]^2} \cos\phi\cos m\lambda \tag{2.8}$$

is imposed on the shear flow, where $\zeta_\circ$ is a parameter determining wave amplitude, $\phi_m = 45°$N and $\sigma = 10°$.

2.3.2 Linear eigenvalue problem

To evaluate the validity of linear wave theory, it is useful to calculate latitudes of critical lines. To this end one must first solve an eigenvalue problem. As discussed in H85, for a small-amplitude ζ', (2.6) can be linearized about the zonal flow $\bar{u}(\phi) = a\omega\mu_c$ [(3.1) of H85], with a denoting the Earth's radius, ω the angular velocity of the flow, and $\mu_c \equiv \cos\phi$:

$$\frac{\partial\zeta'}{\partial t} + \frac{\bar{u}}{a\mu_c}\frac{\partial\zeta'}{\partial\lambda} = -\frac{\gamma}{a\mu_c}\frac{\partial\psi'}{\partial\lambda}, \tag{2.9}$$

where $\gamma \equiv \frac{1}{a}\frac{\partial}{\partial\phi}(f + \bar{\zeta})$ is the mean meridional vorticity gradient, ψ' is the perturbation streamfunction ($\zeta' = \nabla^2\psi'$). The hyperviscosity term in (2.6) is neglected here, as the

dissipation it causes does not affect large-scale dynamics. Assuming a form of plane wave $\zeta' = \zeta_v(\phi)e^{im(\lambda - ct)}$, where m is the zonal wave number and c is the (angular) phase speed of the wave (and subscript v is used to identify ζ_v as the eigenvector to be solved), (2.9) can be rewritten as an eigenvalue problem [(3.2) of H85]:

$$\left[\frac{\bar{u}}{a\mu_c} + \frac{\gamma}{a\mu_c}\nabla_m^{-2}\right]\zeta_v = c\zeta_v, \tag{2.10}$$

where

$$\nabla_m^2 \equiv \frac{1}{(a\mu_c)^2}\left[\mu_c\frac{\partial}{\partial\phi}\left(\mu_c\frac{\partial}{\partial\phi}\right) - m^2\right]. \tag{2.11}$$

The eigenvectors ζ_v and the corresponding eigenvalues c (phase speed in s^{-1}) can be solved. In this setup where meridional shear is present (i.e. $\frac{\partial\bar{u}}{\partial\mu_c} \neq 0$), eigenvectors with $c > \max\left[\frac{\bar{u}(\mu_c)}{a\mu_c}\right]$ are discrete modes, whereas those with $\min\left[\frac{\bar{u}(\mu_c)}{a\mu_c}\right] < c < \max\left[\frac{\bar{u}(\mu_c)}{a\mu_c}\right]$ are singular neutral modes that belong to a continuum spectrum. Since γ is everywhere positive, there are no exponentially growing or damping modes. By projecting (2.8) onto the eigenvectors, one could tell how much of the initial wave activity would persist (as discrete modes), and how much would get sheared and dissipated (as continuum modes).

Equation (2.10) is discretized with a spatial resolution ten times higher than HP87 (i.e. using 1001 grid points along the meridian from 0° to 90°N) and the eigenvalue problem is solved numerically. With $m = 6$, the initial pseudomomentum is almost entirely contained in the continuum mode (H85). Figure 2.1 shows the histogram of angular phase speed ca (eigenvalues c multiplied by Earth's radius a). The dominant angular phase speed is found to be 24 ms^{-1}. The critical line theory [e.g. Held (1983); Randel and Held (1991)] predicts that waves with angular phase speed ca cannot propagate beyond the critical line, namely, the latitude where $u(\phi)/\cos\phi = ca$. For this eigenvalue problem, there are three critical lines: one on the subtropical flank of the jet at 20°N, the other two on the poleward flank at 61°N and 79°N (Fig.2.2). The position of the critical line on the subtropical flank is consistent with the results in HP87 (while they did not mention any results about the critical

lines on the poleward flank). Since the eigenvalues and eigenvectors are independent of the wave amplitude $\zeta_\circ$, so are the predicted critical latitudes. As one will see in the following numerical simulation, when the wave amplitude in the initial condition is large, the wave packets migrating from the source toward the equator break on the subtropical flank of the jet before reaching the predicted critical latitude. Therefore the critical latitudes given by the linear theory are of limited value as a predictor of the wave breaking location when the wave amplitude is large.

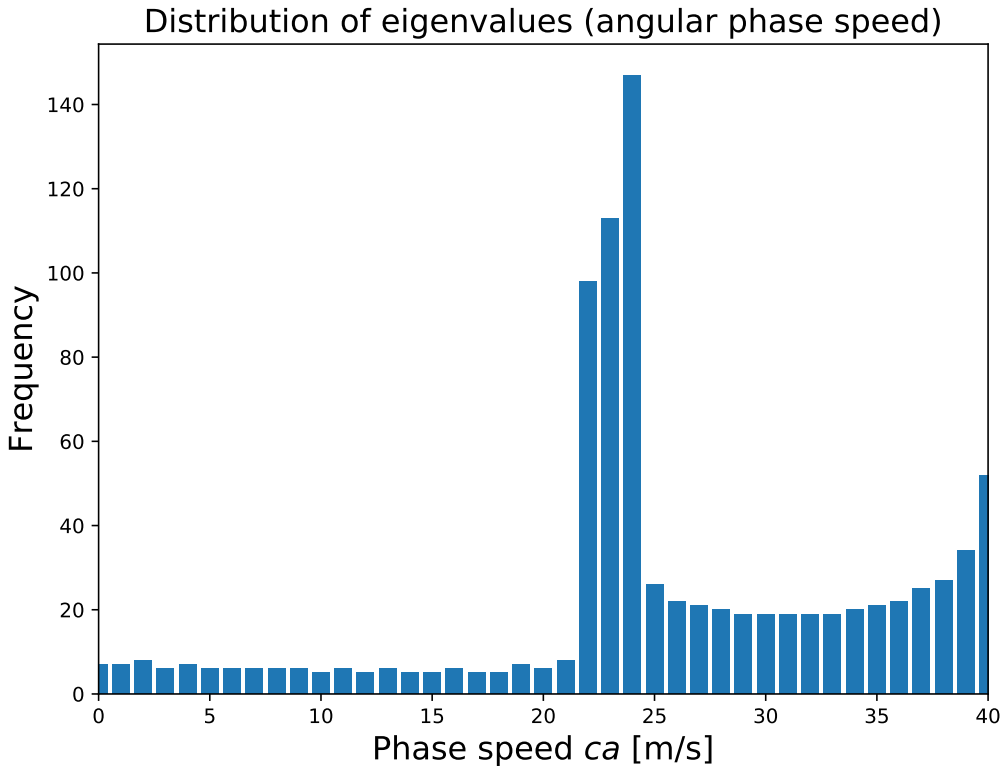

Figure 2.1: The histogram of eigenvalues (multiplied by Earth's radius a) obtained by solving the eigenvalue problem (2.10) numerically. There are 1001 grid points in the latitude grid used in the numerical solver, and thus the total number of eigenvalues obtained is 1001. Only positive values of ca ranging from 0 to 40 ms^{-1} are displayed here. The values of ca are binned into 1 ms^{-1} intervals.

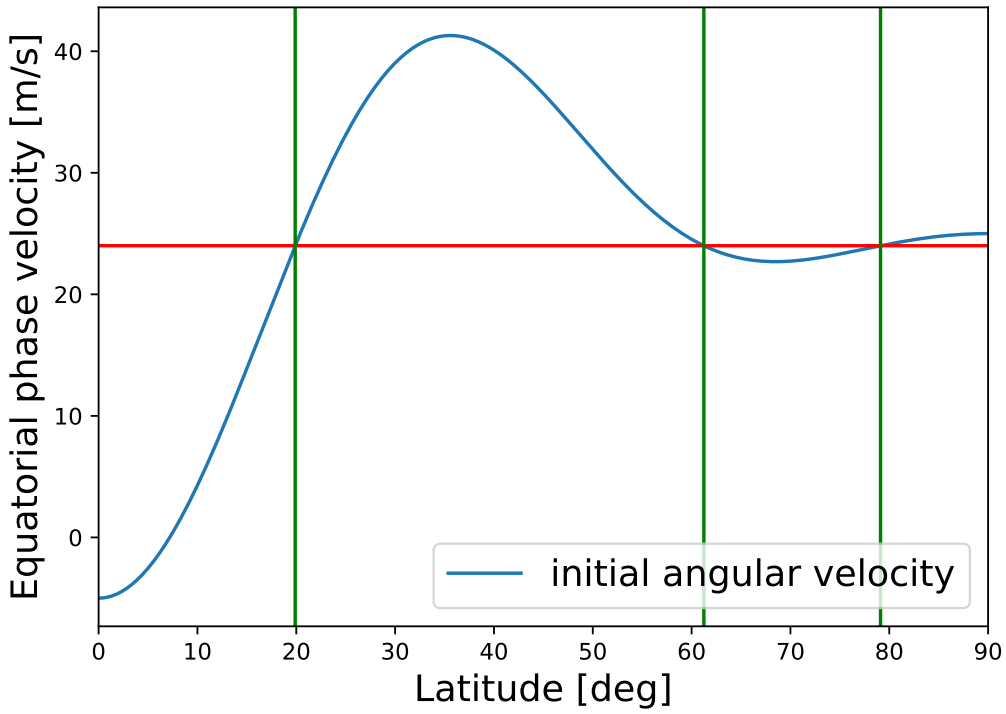

Figure 2.2: The initial angular velocity (blue) in the HP87, i.e. (2.7) divided by $\cos\phi$. The dominant angular phase speed obtained from the eigenvalue problem is 24 ms^{-1} (red). There are three latitudes at which $u/\cos\phi = ca$ (green): 20°N, 61° N and 79° N.

2.3.3 Numerical Simulation

Here I solve numerically the fully nonlinear initial value problem with the initial conditions (2.7) and (2.8). Spectral method with triangular truncation at wavenumber 170 is used to integrate the BVE (2.6) for 30 days with time increment $\Delta t = 0.1$ hour. Figure 2.3 shows the evolution of absolute vorticity q for model runs with ζ_o =1, 5, and 8 $\cdot 10^{-5}\mathrm{s}^{-1}$. As discussed above, the linear theory predicts three critical lines on both flanks of the jet in the initial background shear flow. In all cases, the Gaussian wave packet initially centered at $\phi = 45°$ splits into poleward and equatorward traveling packets, both of which eventually get dissipated.

Figures 2.4 and 2.5 show the latitude-time plot of (left column) linear wave activity A [(1.5)] and (right column) FAWA A^* in [(1.14)] for various ζ_o (with a $10^{-5}\mathrm{s}^{-1}$ increment).

In the plots of A, the dark shades indicate values exceeding the color range, while the green shades indicate where the zonal-mean PV gradient ≤ 0. Those are instants when wave breaking occurs that PV contours overturn. As the PV gradient almost vanishes, the magnitude of A becomes large and unbounded. In comparison, A^* is positive-definite and its magnitude is well-constrained, thus it is a better candidate than A to diagnose wave-mean flow interaction when small-amplitude wave assumption breaks down (at $\zeta_o = 1 \cdot 10^{-5}\mathrm{s}^{-1}$ as derived in HP87). Only A^* can give a closed budget for finite-amplitude waves since A has its value unbounded, as discussed in the next subsection.

2.3.4 Budget of FAWA in spherical coordinates

The budget equation for A^* can be obtained by differentiating (1.14) with respect to time and making use of PV conservation. NZ10 derived in their equation (24a) the budget of A^* on the beta-plane. For the barotropic decay model on a sphere, it reads:

$$\underbrace{\frac{\partial}{\partial t}A^*\cos\phi}_{\text{FAWA tendency}} = \underbrace{-\overline{v'q'}\cos\phi}_{\substack{\text{meridional eddy}\\ \text{vorticity flux}}} - \underbrace{K_{\text{eff}}\frac{\cos\phi}{a}\frac{\partial Q}{\partial\phi}}_{\substack{\text{effective diffusive flux}\\ \text{of vorticity}}} - \underbrace{\frac{\nu\cos\phi}{a^3}\frac{\partial}{\partial\phi}\left[\frac{1}{\cos\phi}\frac{\partial}{\partial\phi}\left(\cos\phi\frac{\partial\bar{q}}{\partial\phi}\right)\right]}_{\substack{\text{meridional flux of}\\ \text{zonal-mean vorticity due to}\\ \text{hyperviscosiy}}}, \tag{2.12}$$

where K_{eff} is the effective diffusivity introduced in Section 1.4.2 and is related to hyperviscosity and vorticity through

$$\mathrm{K}_{\text{eff}}(\phi,t) \equiv \frac{-\nu a^2\left\langle\nabla(\nabla^2 q)\cdot\nabla q\right\rangle_Q}{(\partial Q/\partial\phi)^2}. \tag{2.13}$$

Here ∇ is the horizontal gradient operator and $\langle \cdots \rangle_Q$ denotes the area-weighted average around the vorticity contour $q = Q$ [Nakamura (1996), NZ10 Appendix D]. $\frac{\partial Q}{\partial \phi}$ gives the meridional gradient of vorticity in equivalent latitude. Their product, $K_{\rm eff}\frac{\cos\phi}{a}\frac{\partial Q}{\partial \phi}$ (e.g. Fig.2.6d) is the effective diffusive flux of vorticity through its wavy contour and it gives the rate of dissipation of A^* due to mixing. It attains a large value when wave breaking sheds small-scale filaments that are subsequently dissipated by hyperviscosity. The last term in (2.12) gives the diffusive flux of vorticity through the line of equivalent latitude, which is usually much smaller than the diffusion through the wavy contour. Note that the meridional eddy vorticity flux is related to the divergence of eddy momentum flux through Taylor's identity (1.12):

$$-\overline{v'q'}\cos\phi = \frac{1}{a\cos\phi}\frac{\partial}{\partial\phi}\left(\overline{u'v'}\cos^2\phi\right). \tag{2.14}$$

The zonal-mean zonal wind (relative angular momentum) equation reads

$$\underbrace{\frac{\partial}{\partial t}\bar{u}\cos\phi}_{\substack{\text{zonal wind (angular}\\ \text{momentum) tendency}}} = \underbrace{\overline{v'q'}\cos\phi}_{\substack{\text{meridional eddy}\\ \text{vorticity flux}}} + \underbrace{\frac{\nu\cos\phi}{a^3}\frac{\partial}{\partial\phi}\left[\frac{1}{\cos\phi}\frac{\partial}{\partial\phi}\left(\cos\phi\frac{\partial\bar{q}}{\partial\phi}\right)\right]}_{\substack{\text{meridional flux of}\\ \text{zonal-mean vorticity due to}\\ \text{hyperviscosiy}}}. \tag{2.15}$$

The meridional eddy vorticity flux is present in both (2.12) and (2.15) but with opposite signs. This term indicates exchange of angular momentum between the zonal flow and eddies by advection, which is a conservative process. Such exchange is apparent in the large amplitude cases (e.g. $\zeta_{\rm o} \geq 7\cdot 10^{-5}{\rm s}^{-1}$, Fig.2.6): pulsing and wobbling (between $27^\circ - 37^\circ$N) are observed in $A^*\cos\phi$ (Fig.2.6b) and less apparently in $\bar{u}\cos\phi$ (Fig.2.6a) on the subtropical flank of the zonal jet. The meridional dipole patterns appearing from Day 5 onward in the meridional eddy vorticity flux $\overline{v'q'}\cos\phi$ (Fig.2.6e) largely explains the evolution of $A^*\cos\phi$ and $\bar{u}\cos\phi$. On the other hand, the effective diffusive flux of vorticity provides a slow damping on $A^*\cos\phi$.

As seen from Fig.2.5 (right column), $A^* \cos\phi$ is damped gradually, with a time-scale much longer than oscillation due to $\overline{v'q'}\cos\phi$ (or equivalently, the divergence of eddy momentum flux).

The global wave activity budget is examined by integrating (2.12) over the spatial domain, upon which only the effective diffusive flux term is non-vanishing:

$$\frac{\partial}{\partial t}\int_{-\pi/2}^{\pi/2} A^* \cos^2\phi d\phi = -\int_{-\pi/2}^{\pi/2} K_{\rm eff}\frac{\cos^2\phi}{a}\frac{\partial Q}{\partial \phi}d\phi. \tag{2.16}$$

Integrate further with respect to time gives:

$$\int_{-\pi/2}^{\pi/2} (A^*(t) - A^*(0))\cos^2\phi d\phi = -\int_{-\pi/2}^{\pi/2}\left[\int_0^t K_{\rm eff}\frac{\cos^2\phi}{a}\frac{\partial Q}{\partial \phi}dt\right]d\phi. \tag{2.17}$$

Figure 2.7 shows FAWA (left), effective diffusive flux (middle), and the comparison of LHS (blue) and RHS (red) of (2.17) (right). Large values in the effective diffusive flux indicates enstrophy cascade (stirring) due to wave breaking events. For $\zeta_{\rm o} \geq 7 \cdot 10^{-5}{\rm s}^{-1}$, significant global damping of $A^* \cos\phi$ starts on Day 5 (Fig.2.7, right). When the initial wave amplitude is increased, wave breaking occurs earlier with greater intensity. Note that a minimum in the effective diffusive flux is observed at the latitude where the axis of the zonal jet resides (Fig.2.7, middle). This is consistent with the 'wave-turbulence jigsaw' described by McIntyre (1982) and by Dritschel and McIntyre (2008) in that the jet self-sharpening is a result of PV mixing on the flank(s) of the jet.

For larger-amplitude wave simulations, the two curves in the right column of Fig.2.7 overlap closely, indicating that the formalism is capable of giving a closed budget of wave activity. In the small-amplitude cases, relative discrepencies are large especially after $t = 10$ days when the mixing process has ended. By this time, the shear flow becomes more or less zonal and the wave amplitude is very small. This poses a numerical challenge to the box-counting calculation of A^* [which approximates the surface integrals in (1.16)]. When wave amplitude is small and the meridional contour displacement is comparable to the grid size,

such method can hardly be accurate computing the budget. [This also causes small-scale wiggles in the curve of A^* in the top right panel of Fig.2.7 and a visible noise (white areas) in the right panels of Fig.2.4.] Note that this discrepancy is unrelated to intrinsic properties of A^* – rather it is purely a numerical issue, which can be improved by increasing resolution (tested; not shown).

2.3.5 The eddy-free zonal wind reference state u_{REF}

As mentioned in Section 1.4.3, an eddy-free zonal wind reference state u_{REF} can be defined by $\bar{u}$ and A^* (in this barotropic case, $u_{\mathrm{REF}} = \bar{u} + A^*$) such that u_{REF} is time-invariant under conservative dynamics (i.e. intact upon advection). The modification in u_{REF} for this barotropic decay model is solely due to the dissipation of wave activity by hyperviscosity. Figure 2.8 shows u_{REF} for the cases of $\zeta_{\mathrm{o}} = 1 \cdot 10^{-5}\mathrm{s}^{-1}$ (left) and $7 \cdot 10^{-5}\mathrm{s}^{-1}$ (right). Note that u_{REF} for the latter case is displaced to the north, because the peak amplitude of A^* is located north to the axis of the jet. With no wave breaking (i.e. no vorticity contour overturning, as indicated in Fig.2.4), u_{REF} in the small-amplitude case is almost constant in time. When the wave amplitude is large, the reference state is permanently 'eroded' by the wave breaking events on the jet flank. As quantified by the effective diffusive flux (Fig.2.7, middle), the dissipation of A^* and thus of u_{REF} is greater on the subtropical flank.

Compared to the time-scale of variability of the zonal wind $\bar{u}$ in Fig.2.6a [$\sim$8 days/cycle, also inferred from Fig.2.6e], that of u_{REF} is much longer. Since u_{REF} only responds to slower non-conservative forces, it is a cleaner (i.e. less noisy) basic state for comparison among climate states involving transient events, such as when comparing composites of eddy life cycles lasting for < 20 days. In short, u_{REF} captures variability longer than the synoptic time-scale, and it provides a quantitative measure of how the zonal flow is affected by non-conservative processes.

2.3.6 Latitudes of wave breaking

As shown in Figs. 2.4 and 2.5, the bands of large A^* on the flanks of the zonal jet, which indicate breaking of waves at those latitudes, shift poleward when the initial wave packet imposes a larger amplitude. This shows the limitation in the critical line theory based on the linear wave dynamics mentioned in Section 2.3.2, which predicts that a critical layer (region of wave breaking) develops around the critical line (Stewartson, 1977; Warn and Warn, 1978).

2.4 Chapter conclusion

This chapter examines the behaviors of the small-amplitude wave activity and FAWA in the idealized barotropic decay simulation of HP87 with various amplitudes of wave packets prescribed. The FAWA is shown to be a better metric of wave amplitude at large amplitude in that it remains well-defined at instances of PV gradient reversal, while the small-amplitude wave activity becomes unbounded (Figs. 2.4 and 2.5). The decomposition of wave activity budget (Fig.2.6) illustrates how one can understand the 'wave-turbulence jigsaw' in terms of angular momentum exchange between the eddies and the mean flow and irreversible mixing of vorticity. More importantly, the budget of FAWA is shown to be closed (Fig.2.7) with effective diffusivity in this barotropic decay problem where no forcing is imposed on the flow. Such a clean budget analysis has not been shown in any previous studies. Lastly, the simulation results highlight the inadequacy of linear critical line theory in predicting the latitudes of wave breaking. The use of FAWA formalism and its extension (to be discussed in Chapter 3) to predict the onset and location of wave breaking / blocking is not addressed here, but will be discussed in Chapter 5 as potential areas of application.

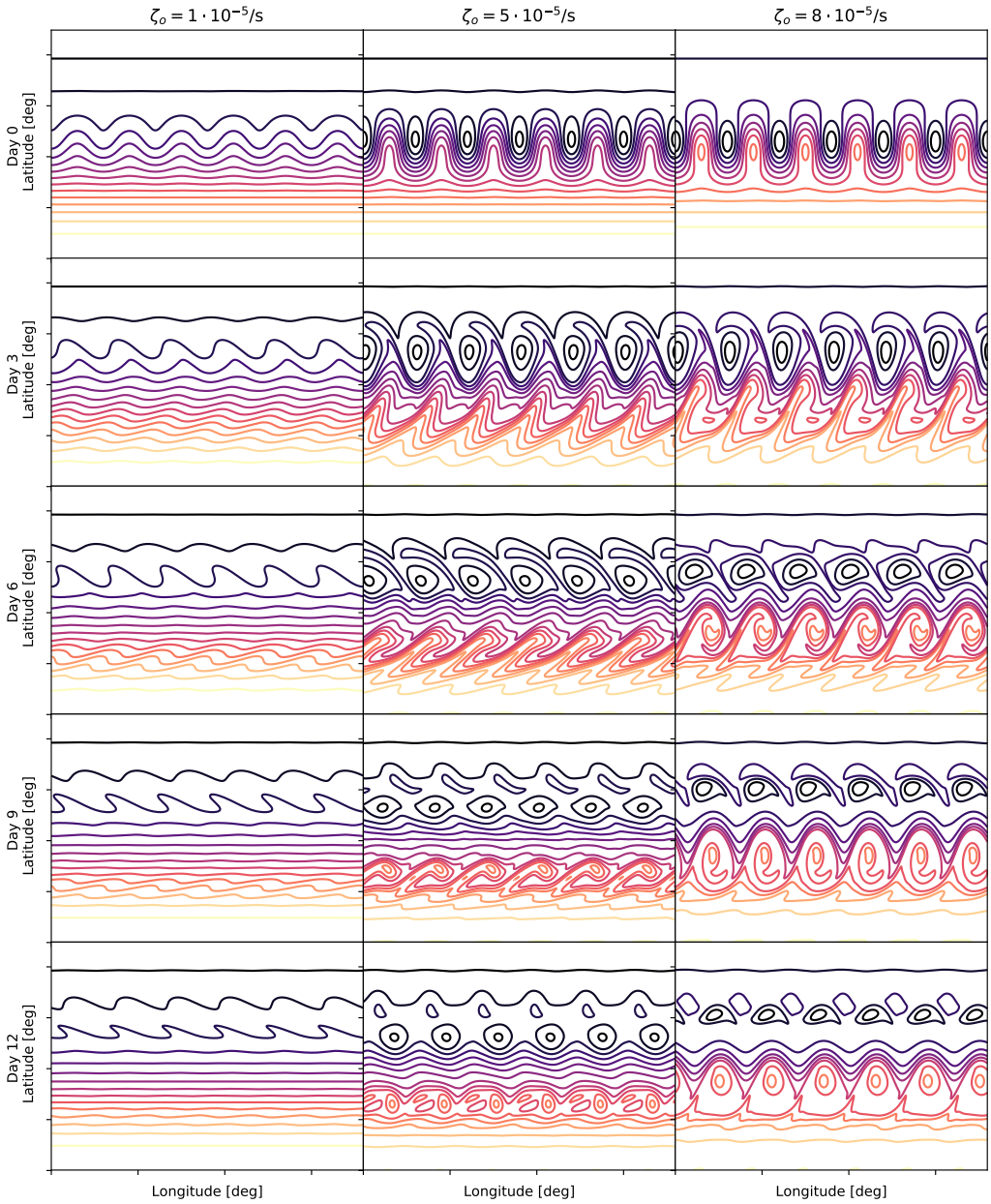

Figure 2.3: Snapshots of absolute vorticity q from the model runs with ζ_o =1, 5, and 8 $\cdot 10^{-5}$s^{-1} on Days 0, 3, 6, 9 and 12. Darker vorticity contours indicate higher vorticity values.

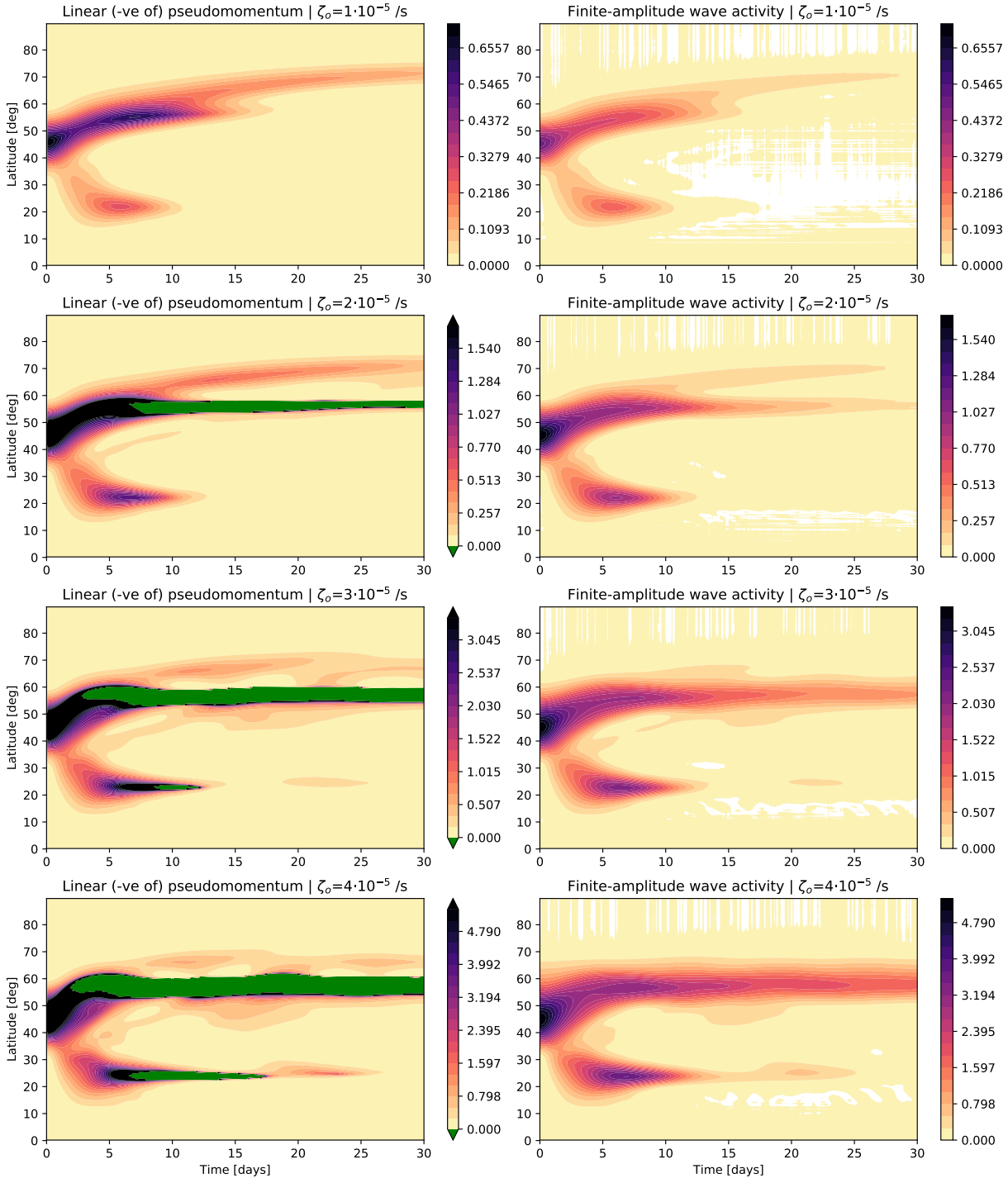

Figure 2.4: Latitude-time plot of (left) $A\cos\phi$ and (right) $A^*\cos\phi$ from the simulation with ζ_o =1, 2, 3, and 4·10^{-5}s^{-1}. The color scale is set according to the range of A^*. In the plots of A, dark regions indicate values exceeding the color range, while green regions indicate instants when vorticity gradient turns negative (and almost vanishing) such that A becomes unbounded.

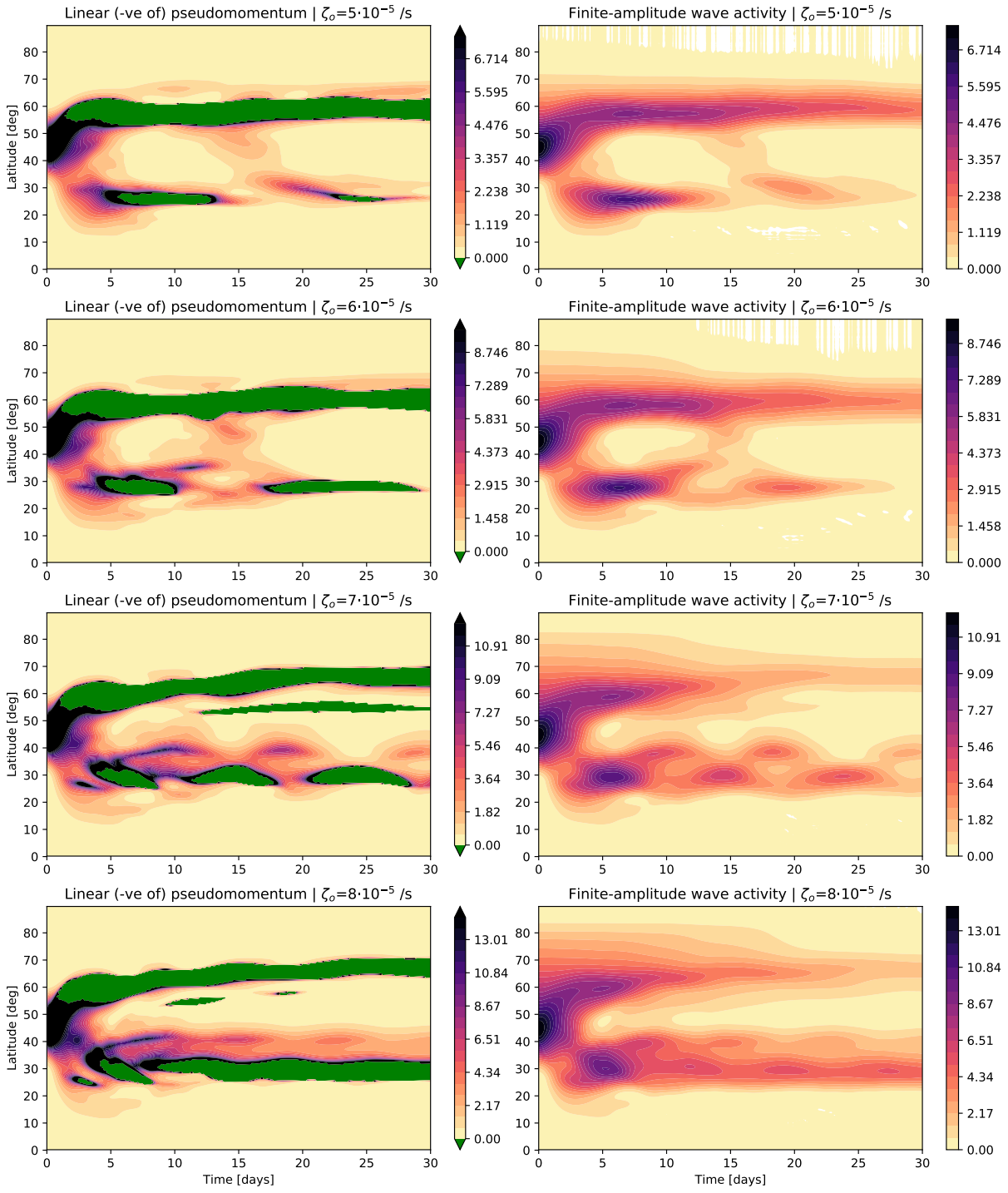

Figure 2.5: Same as 2.4 but for ζ_o =5, 6, 7, and 8·10^{-5}s^{-1}.

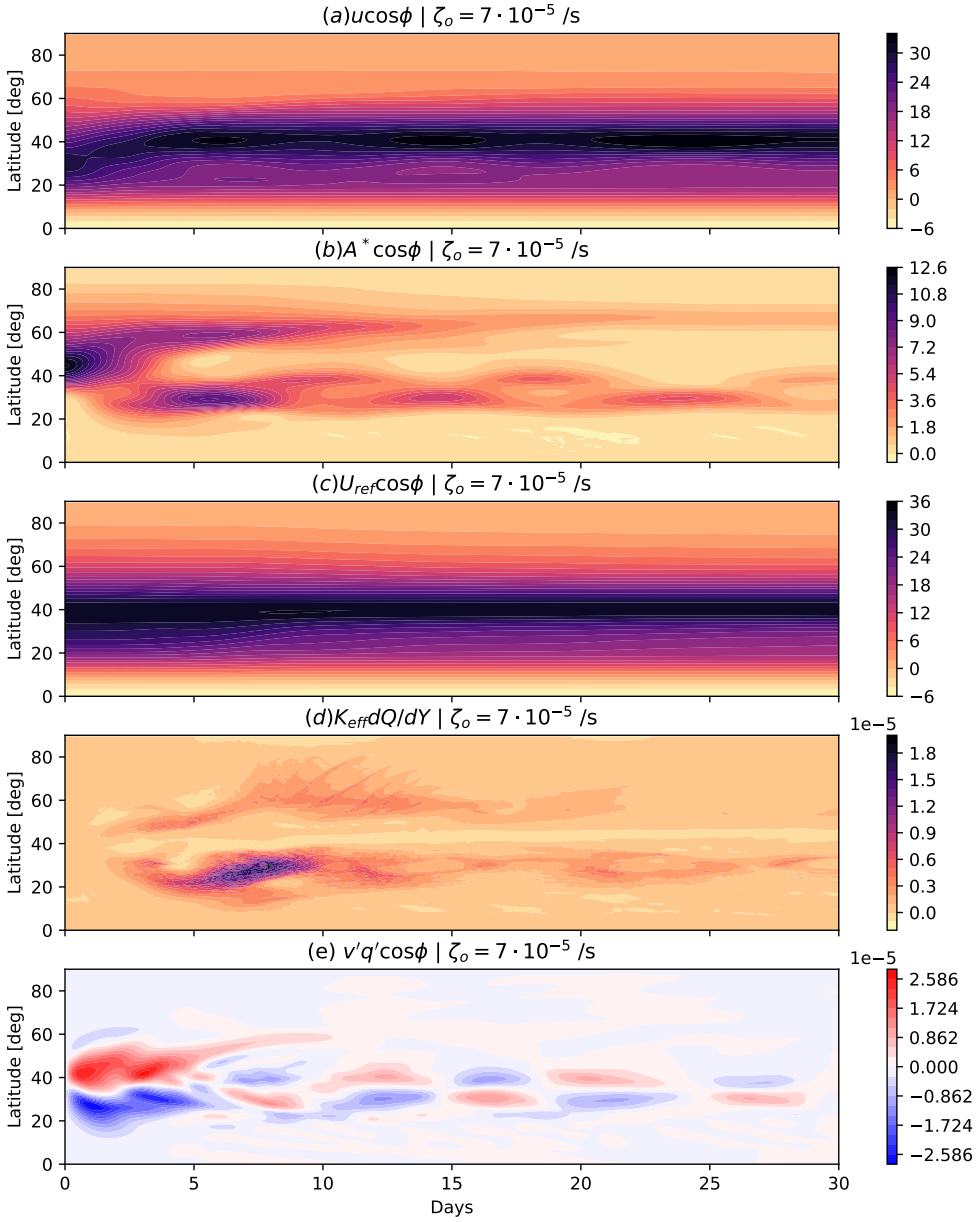

Figure 2.6: From the simulation with $\zeta_o = 7 \cdot 10^{-5} s^{-1}$ latitude-time plots of (a) zonal wind $\bar{u} \cos \phi$, (b) FAWA $A^* \cos \phi$, (c) eddy-free reference state $u_{\mathrm{REF}} \cos \phi$, which is equal to $(\bar{u} + A^*) \cos \phi$ in this barotropic case, (d) effective diffusive flux, and (e) meridional eddy vorticity flux $\overline{v'q'} \cos \phi$.

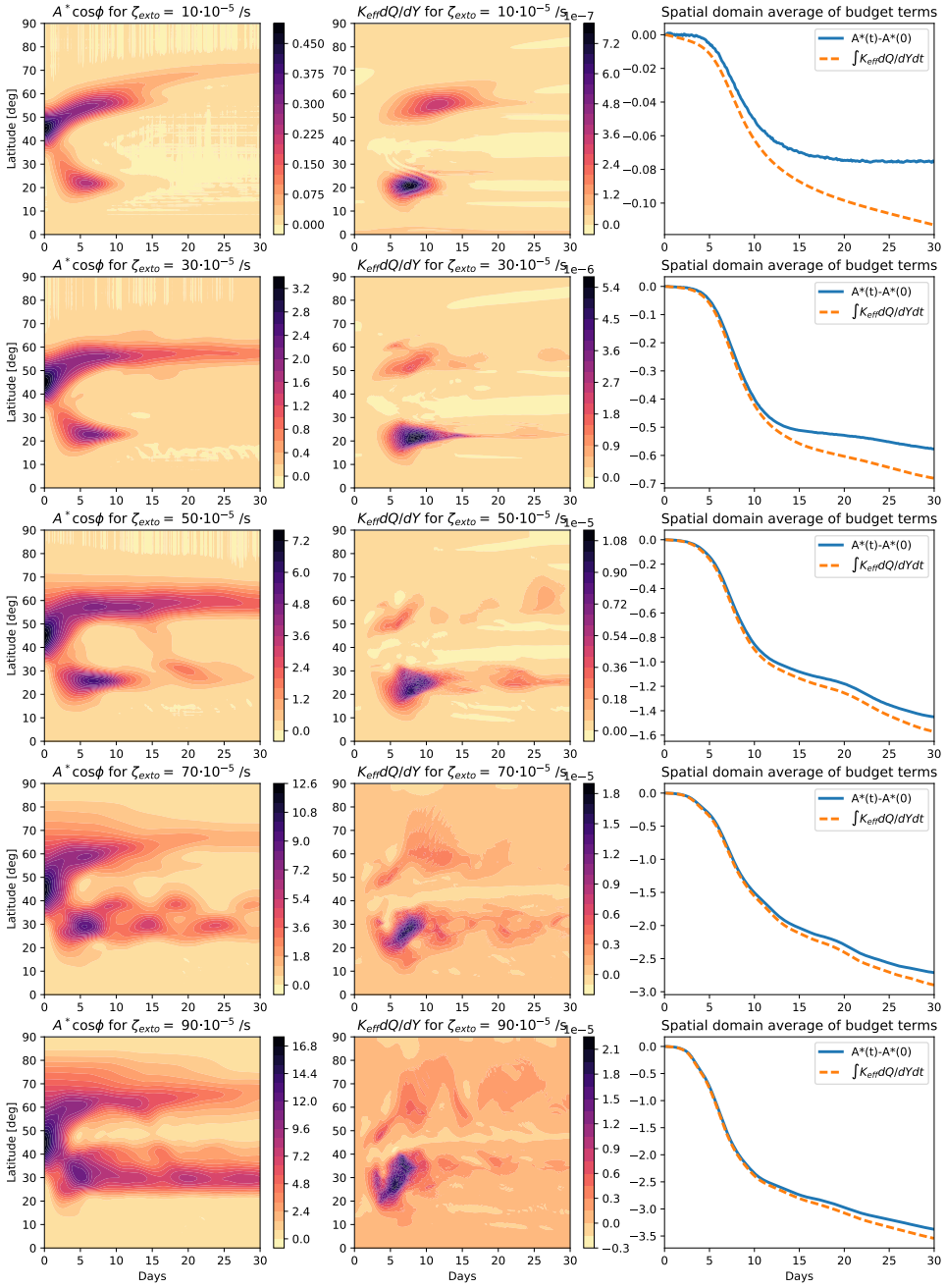

Figure 2.7: (Left column) FAWA, (middle column) effective diffusive flux, and (right column) the domain integral of (1) change in FAWA (blue line) and (2) cumulative dissipation (dashed orange line) as a function of time for various wave amplitudes imposed.

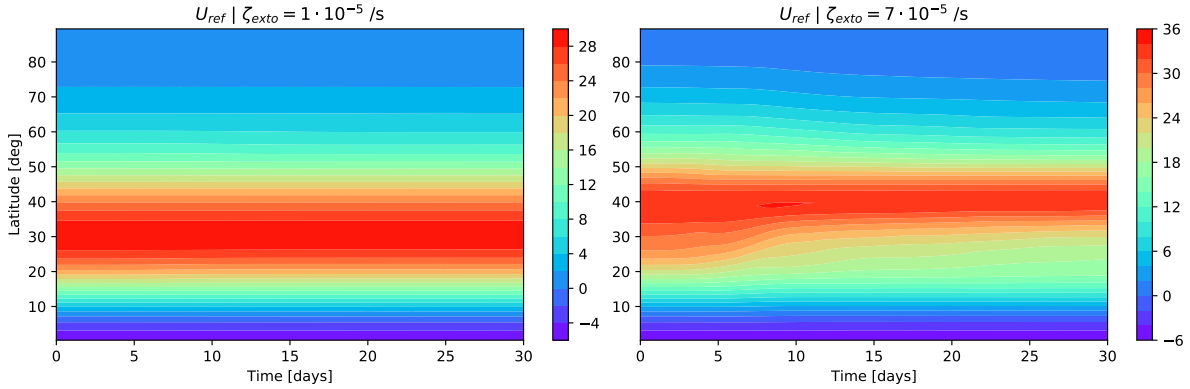

Figure 2.8: The evolution of eddy free reference states u_{REF} from the simulation with $\zeta_{\mathrm{o}} = 1 \cdot 10^{-5}\mathrm{s}^{-1}$ (left) and $\zeta_{\mathrm{o}} = 7 \cdot 10^{-5}\mathrm{s}^{-1}$ (right) from Day 0 to 30. Note that the initial u_{REF} for $\zeta_{\mathrm{o}} = 7 \cdot 10^{-5}\mathrm{s}^{-1}$ (right) is displaced to the north, because the peak amplitude of initial A^* is located north to the axis of the jet.

CHAPTER 3

THE FINITE-AMPLITUDE LOCAL WAVE ACTIVITY (LWA) FORMULATION

3.1 Introduction

Waves play an important role of rearranging angular momentum in the atmosphere. This process is summarized by the generalized Eliassen-Palm (E-P) relation (1.8) (Andrews and McIntyre, 1976). For a small-amplitude, conservative wave, the RHS terms of (1.8) are negligible and wave activity density changes only where there is nonzero E-P flux divergence. The E-P flux divergence in turn drives the angular momentum of the mean flow, thus acting as the agent of wave-mean flow interaction [(1.9)].

As reviewed in Chapter 1, Nakamura and Zhu (2010) (NZ10 hereafter) extended (1.8) for finite-amplitude Rossby waves and balanced eddies by introducing the *finite-amplitude wave activity* (FAWA) based on the meridional displacement of quasi-geostrophic potential vorticity (QGPV) from zonal symmetry. The formalism eliminates the cubic term from the right-hand side of (1.8) and extends the non-acceleration theorem (Charney and Drazin, 1961) for an arbitrary eddy amplitude. This allows one to quantify the amount of the mean flow modification by the eddy [Nakamura and Solomon (2010, 2011), see also (1.21)].

Furthermore, the PV-equivalent latitude relation $Q(y, z)$ may be exploited to define a zonally symmetric, time-invariant 'reference state'. It is a hypothetical distribution of PV that arises from 'zonalizing' the wavy PV contours on the z surface without changing the enclosed areas (Fig.1.3a and b). The corresponding flow $u_{\rm REF}(y, z)$ and temperature field $\theta_{REF}(y, z)$ may be inverted from $Q(y, z)$ assuming geostrophic balance: for the barotropic case, simply $u_{REF} = \bar{u} + A^*$. The notion of reference state may be generalized to a 'slowly varying state' under non-conservative dynamics.

Despite its amenability to data, FAWA is a zonally averaged quantity and incapable of distinguishing longitudinally isolated events such as atmospheric blocking. In this chapter, I

will address this shortcoming by introducing the *finite-amplitude local wave activity* (LWA). In essence, LWA quantifies longitude-by-longitude contributions to FAWA and as such recovers FAWA upon zonal averaging. As a first step into this topic, the present chapter concerns primarily the conservative dynamics of local eddy-mean flow interaction. Explicit representation of non-conservative dynamics (such as local diffusive flux of PV) will be deferred to a future work. However, when observed data deviates from the theory, it may be readily interpreted as an indication of non-conservative effects. The material is organized as follows: Sections 3.2 to 3.4 lay out the theory. Section 3.5 demonstrates the utility of LWA using idealized simulations with barotropic vorticity equation on a sphere. I will compare LWA with one of the existing local metrics of finite-amplitude wave activity: Impulse-Casimir wave activity [ICWA, Killworth and McIntyre (1985); McIntyre and Shepherd (1987); Haynes (1988)]. As an application of LWA, a blocking episode that steered Superstorm Sandy to the East Coast of the US in 2012 will be studied in Section 3.6. Discussion and concluding remarks will follow in Section 3.7.

3.2 Generalization of FAWA to longitude-dependent wave activity (LWA)

3.2.1 Definitions

Although the FAWA formalism quantifies waviness in the PV contours and the associated mean flow modification [see for example Solomon (2014) for stratospheric wave activity events], it is not suited to distinguish the longitudinal location of an isolated large-amplitude event such as blocking. To achieve this, $A^*(y, z, t)$ needs to be generalized to a function of longitude as well. In the following I assume that it is only the eddy properties that vary in longitude and continue to use $Q(y, z)$, $u_{\mathrm{REF}}(y, z)$, and $\theta_{\mathrm{REF}}(y, z)$ as a reference state to define the eddy fields. A zonally symmetric reference state may not reflect the zonally asymmetric nature of the time-mean flow, but it is a required construct for the conservation

of wave activity. (I will describe a method to separate the stationary-eddy component of LWA from the time-mean state in Section 4.2.2.) Keep in mind that despite the enforced zonal symmetry, the reference state shares the same PV-area relation $Q(y,z)$ with the full wavy state so it is strongly constrained to the actual climate state (Nakamura and Solomon, 2010, 2011; Methven and Berrisford, 2015).

Because of the waviness in the flow, the PV contour of value Q is displaced locally from (x,y,z) to $(x,y+\eta(x,y,z,t),z)$, where $\eta(x,y,z,t)$ is defined positive northward. (As we will see below, η can be multivalued in y.) Now let $0 \le y' \le \eta$ or $0 \ge y' \ge \eta$ depending on the sign of η. The eddy field is defined between (x,y,z) and $(x,y+\eta,z)$ as

$$u_e(x,y+y',z,t) \equiv u(x,y+y',z,t) - u_{\mathrm{REF}}(y,z), \tag{3.1}$$

$$v_e(x,y+y',z,t) \equiv v(x,y+y',z,t), \tag{3.2}$$

$$\theta_e(x,y+y',z,t) \equiv \theta(x,y+y',z,t) - \theta_{\mathrm{REF}}(y,z), \tag{3.3}$$

$$q_e(x,y+y',z,t) \equiv q(x,y+y',z,t) - Q(y,z). \tag{3.4}$$

In the baroclinic QG framework, QGPV defined in (1.6) is used. Notice that the displacement coordinate y' is independent of y; in other words the eddy field is *not* defined globally as the total field minus the reference state but it needs to be redefined for each y. By definition

$$q(x,y+\eta(x,y,z,t),z,t) = Q(y,z), \qquad q_e(x,y+\eta(x,y,z,t),z,t) = 0 \tag{3.5}$$

and

$$0 = \frac{1}{L_x}\left(\iint_{D_1} dxdy' - \iint_{D_2} dxdy'\right) \quad \Rightarrow \quad \frac{1}{L_x}\int_0^{L_x}\left(\int_0^{\eta(x,y,z,t)} dy'\right)dx = \overline{\eta} = 0. \tag{3.6}$$

Here D_1 and D_2 denote the domains of surface integrals used to compute FAWA (red and blue areas in Figs. 3.1 and 1.3), and L_x is the length of the equivalent latitude circle.

The definition of LWA, $\tilde{A}^*(x,y,z,t)$, follows most naturally by rewriting the expression of FAWA on a beta-plane [NZ10 Eqn.(11)] as:

$$\begin{aligned}
A^*(y,z,t) &= \frac{1}{L_x}\int_0^{L_x}\left(\int_{y+\eta(x,y,z,t)}^{y_{\max}} q(x,y',z,t)dy' - \int_y^{y_{\max}} q(x,y',z,t)dy'\right)dx \\
&= -\frac{1}{L_x}\int_0^{L_x}\left(\int_y^{y+\eta} q(x,y',z,t)dy'\right)dx \\
&= -\frac{1}{L_x}\int_0^{L_x}\left(\int_0^{\eta} (q_e(x,y+y',z,t)+Q(y,z))dy'\right)dx \\
&= \frac{1}{L_x}\int_0^{L_x}\left(\tilde{A}^*(x,y,z,t)-\eta Q(y,z)\right)dx \\
&= \overline{\tilde{A}^*(x,y,z,t)} - \overline{\eta(x,y,z,t)}Q(y,z) \\
&= \overline{\tilde{A}^*(x,y,z,t)}, \qquad (3.7)
\end{aligned}$$

where the last line used (3.6). I define LWA, $\tilde{A}^*(x,y,z,t)$, as

$$\boxed{\tilde{A}^*(x,y,z,t) \equiv -\int_0^{\eta(x,y,z,t)} q_e(x,y+y',z,t)dy'} \qquad (3.8)$$

or equivalently

$$\boxed{\tilde{A}^*(x,y,z,t) \equiv \int\limits_{W_-} q_e(x,y+y',z,t)dy' - \int\limits_{W_+} q_e(x,y+y',z,t)dy'} \qquad (3.9)$$

$$W_+ : \;\; 0 \le y' \le \eta_+(x,y,z,t), \;\; q \le Q(y,z); \qquad W_- : \;\; 0 \ge y' \ge \eta_-(x,y,z,t), \;\; q \ge Q(y,z). \qquad (3.10)$$

In the above I use $\tilde{(...)}$ to denote wave activity that is a function of both longitude and latitude. It is evident from (3.7) that the zonal average of LWA recovers FAWA. In practice LWA is computed by evaluating (3.9) and (3.10). When there are multiple crossings of the PV contour with the meridian at a given x, I take the furthest crossings from equivalent latitude as $\eta_+ > 0$ and $\eta_- < 0$ in (3.10) and use the PV constraint in (3.10) to sample the correct

segments along the integral path. (Numerically this amounts to a conditional box counting along the meridian.) Computation of $\tilde{A}^*$ is illustrated in Fig.3.1b. On a given z-surface, PV is generally greater on the northern side of the wavy contour than on the southern side, such that $q_e \geq 0$ in the red lobes and $q_e \leq 0$ in the blue lobes. The line integral of q_e over the red area and minus the line integral of q_e over the blue are both positive, which makes $\tilde{A}^*$ a positive definite quantity. By construction, $\tilde{A}^*(x, y, z, t)$ is Lagrangian (nonlocal) in y and Eulerian (local) in x. Notice that since LWA vanishes at the nodes (i.e., crossing of the PV contour and equivalent latitude), it contains the phase structure of the waves in addition to the amplitude. In the small-amplitude, conservative limit (3.8) becomes

$$\tilde{A}^*(x, y, z, t) \quad \rightarrow \quad \tilde{A}_s = \frac{1}{2}\frac{{q'}^2}{\partial\bar{q}/\partial y}. \tag{3.11}$$

3.2.2 Local wave activity and PV gradient

NZ10 shows in their Eqn. (18) that FAWA bridges the Lagrangian- and Eulerian-mean PV via

$$\frac{\partial A^*}{\partial y}(y, z, t) = \bar{q}(y, z, t) - Q(y, z). \tag{3.12}$$

Analogous result may be obtained for LWA when differentiating (3.8) with respect to y. Starting from (3.8)

$$\begin{aligned}
\tilde{A}^*(x, y, z, t) &= -\int_0^{\eta(x,y,z,t)} q_e(x, y + y', z, t)\, dy' \\
&= -\int_y^{y+\eta(x,y,z,t)} \big[q(x, y', z, t) - Q(y, z)\big]\, dy' \\
&= -\int_y^{y+\eta(x,y,z,t)} q(x, y', z, t)\, dy' + Q(y, z)\eta(x, y, z, t).
\end{aligned} \tag{3.13}$$

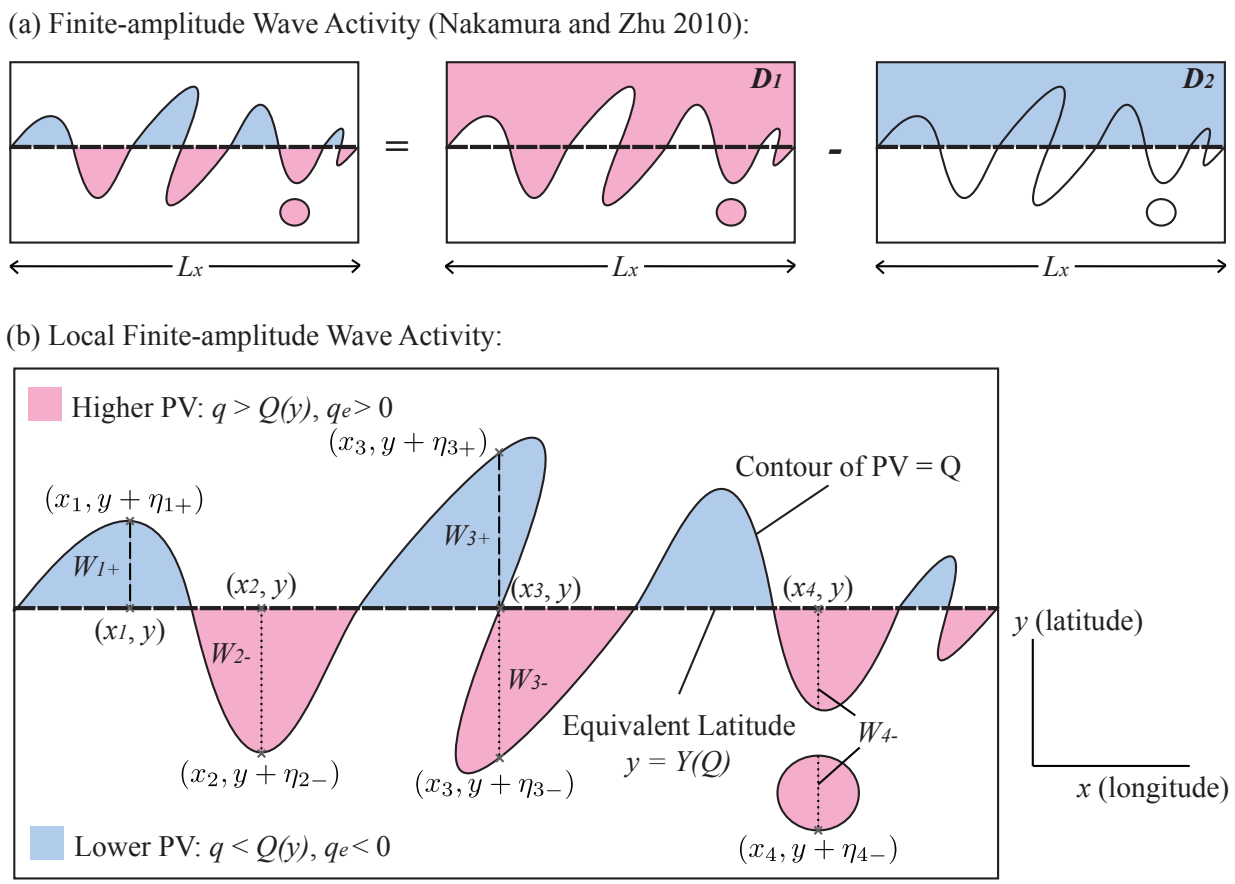

Figure 3.1: (a) A schematic diagram showing (on the x-y plane) the surface integral domains D_1 and D_2 in (3.6), the definition of finite-amplitude wave activity (FAWA) of Nakamura and Zhu (2010). The horizontal dashed lines indicate the equivalent latitude corresponding to the PV contour shown, such that the pink and blue areas are the same. (b) A schematic diagram illustrating how to compute the local finite-amplitude wave activity in (3.9)-(3.10). The wavy curve indicates a contour of PV, above which the PV values are greater than below. Inside the red lobes $q_e \geq 0$ and inside the blue lobes $q_e \leq 0$. Four points are chosen to illustrate how the domain of integral is chosen. $\tilde{A}^*(x_1, y) = -\int\limits_{W_{1+}} q_e(x, y + y', z, t)dy'$; $\tilde{A}^*(x_2, y) = \int\limits_{W_{2-}} q_e(x, y + y', z, t)dy'$; $\tilde{A}^*(x_3, y) = \int\limits_{W_{3-}} q_e(x, y + y', z, t)dy' - \int\limits_{W_{3+}} q_e(x, y + y', z, t)dy'$; $\tilde{A}^*(x_4, y) = \int\limits_{W_{4-}} q_e(x, y + y', z, t)dy'$.

Then by taking the derivative with respect to y and using the Leibniz rule and (3.5), one

obtains

$$\begin{aligned}\frac{\partial \tilde{A}^*}{\partial y} &= -\left(1+\frac{\partial \eta}{\partial y}\right) q(x, y+\eta, z, t) + q(x, y, z, t) + \frac{\partial Q}{\partial y}\eta + Q(y, z)\frac{\partial \eta}{\partial y} \\ &= -\left(1+\frac{\partial \eta}{\partial y}\right) Q(y, z) + q(x, y, z, t) + \frac{\partial Q}{\partial y}\eta + Q(y, z)\frac{\partial \eta}{\partial y} \\ &= q(x, y, z, t) - Q(y, z) + \frac{\partial Q}{\partial y}\eta(x, y, z, t). \end{aligned} \tag{3.14}$$

When η is multivalued, the sum of all values is used. Zonally averaging (3.14) and using (3.6) recovers (3.12). Differentiating this with respect to y again yields

$$\frac{\partial q}{\partial y} = \frac{\partial Q}{\partial y} + \frac{\partial}{\partial y}\left(\frac{\partial \tilde{A}^*}{\partial y} - \frac{\partial Q}{\partial y}\eta\right), \tag{3.15}$$

which generalizes the relation (19) in NZ10. Thus the criterion for local reversal of PV gradient is

$$\frac{\partial Q}{\partial y} + \frac{\partial}{\partial y}\left(\frac{\partial \tilde{A}^*}{\partial y} - \frac{\partial Q}{\partial y}\eta\right) < 0. \tag{3.16}$$

Polvani and Plumb (1992) discuss two regimes of wave breaking in the context of vortex dynamics: major Rossby wave breaking that disrupts the vortex dynamics and microbreaking that only sheds filaments and does not affect the vortex significantly. [See also Dritschel (1988).] In terms of LWA, a major breaking would satisfy (3.16) as well as a large amplification in LWA $\Delta\tilde{A}^* \approx u$, whereas microbreaking would satisfy (3.16) without significant changes in $\tilde{A}^*$.

3.2.3 Local wave activity budget

The governing equation for LWA may be obtained by taking the time derivative of (3.8), together with the Leibniz rule and (3.5):

$$\frac{\partial}{\partial t}\tilde{A}^*(x,y,z,t) = -\frac{\partial \eta}{\partial t} q_e(x, y+\eta, z) - \int_0^\eta \frac{\partial q(x, y+y', z, t)}{\partial t} dy' = -\int_0^\eta \frac{\partial q(x, y+y', z, t)}{\partial t} dy'. \tag{3.17}$$

Conservation of PV in (x, y') is

$$\begin{aligned} 0 = \frac{Dq}{Dt} &= \frac{\partial q}{\partial t} + (u_{\mathrm{REF}}(y,z) + u_e)\frac{\partial q_e}{\partial x} + v_e \frac{\partial}{\partial y'}(q_e + Q(y,z)) \\ &= \frac{\partial q}{\partial t} + u_{\mathrm{REF}}(y,z)\frac{\partial q_e}{\partial x} + \frac{\partial}{\partial x}\left(u_e q_e\right) + \frac{\partial}{\partial y'}\left(v_e q_e\right). \end{aligned} \tag{3.18}$$

Note that the spatial derivative of the eddy quantities is taken with respect to the coordinates (x, y'), and I used nondivergence of (u_e, v_e). Substituting (3.18) into (3.17) yields [with repeated use of the Leibniz rule and (3.5)]

$$\begin{aligned} \frac{\partial}{\partial t}\tilde{A}^*(x,y,z,t) &= \int_0^\eta \left(u_{\mathrm{REF}}(y,z)\frac{\partial q_e}{\partial x} + \frac{\partial (u_e q_e)}{\partial x} + \frac{\partial (v_e q_e)}{\partial y'} \right) dy' \\ &= u_{\mathrm{REF}} \int_0^\eta \frac{\partial q_e}{\partial x} dy' + \int_0^\eta \frac{\partial (u_e q_e)}{\partial x} dy' + (v_e q_e)_{y'=\eta} - (v_e q_e)_{y'=0} \\ &= u_{\mathrm{REF}} \frac{\partial}{\partial x}\int_0^\eta q_e dy' + \frac{\partial}{\partial x}\int_0^\eta u_e q_e dy' - (v_e q_e)_{y'=0} \\ &\quad - \frac{\partial \eta}{\partial x}\left(u_{\mathrm{REF}}(y,z) + u_e(x, y+\eta, z)\right) q_e(x, y+\eta, z) \\ &= -u_{\mathrm{REF}} \frac{\partial \tilde{A}^*}{\partial x} + \frac{\partial}{\partial x}\int_0^\eta u_e q_e dy' - (v_e q_e)_{y'=0}. \end{aligned} \tag{3.19}$$

Rewriting the last term with Taylor's identity and thermal wind balance relation,

$$\begin{aligned} \frac{\partial}{\partial t}\tilde{A}^*(x,y,t) = -u_{\mathrm{REF}}\frac{\partial \tilde{A}^*}{\partial x} + \frac{\partial}{\partial x}\int_0^\eta u_e q_e dy' - \frac{\partial}{\partial x}\left[\frac{1}{2}\left(v_e^2 - u_e^2 - \frac{R}{H}\frac{e^{-\kappa z/H}\theta_e^2}{\partial \tilde{\theta}/\partial z}\right)\right] \\ + \frac{\partial}{\partial y}\left(u_e v_e\right) - e^{z/H}\frac{\partial}{\partial z}\left(\frac{f\, e^{-z/H} v_e \theta_e}{\partial \tilde{\theta}/\partial z}\right), \end{aligned} \tag{3.20}$$

from which one obtains:

$$\frac{\partial \tilde{A}^*}{\partial t} = -e^{z/H} \nabla \cdot (\mathbf{F}_{\text{adv}} + \mathbf{F}_{\text{EP}}), \tag{3.21}$$

where

$$\mathbf{F}_{\text{adv}} \equiv e^{-z/H} \left(u_{\text{REF}}(y,z)\tilde{A}^* - \int_0^\eta (u_e q_e) dy', \quad 0, \quad 0 \right) \tag{3.22}$$

denotes the advective flux of LWA, whereas

$$\mathbf{F}_{\text{EP}} \equiv e^{-z/H} \left(\frac{1}{2} \left(v_e^2 - u_e^2 - \frac{R}{H} \frac{e^{-\kappa z/H} \theta_e^2}{\partial \tilde{\theta}/\partial z} \right), \quad -u_e v_e, \quad \frac{f\, v_e \theta_e}{\partial \tilde{\theta}/\partial z} \right) \tag{3.23}$$

is the generalized E-P flux (Plumb, 1985). Here $\kappa = R/c_p$, R is gas constant, and c_p is specific heat at constant pressure. The first term in the x-component of (3.22) is of $\mathcal{O}\left(\eta^2\right)$ at small amplitude and converges to $e^{-z/H}\bar{u}\tilde{A}_s$. The second term, which is of $\mathcal{O}\left(\eta^3\right)$ and represents the Stokes drift flux of $\tilde{A}^*$, only becomes significant at finite amplitude. In this chapter, no further effort will be made to remove phase information from $\tilde{A}^*$ and fluxes other than averaging over a longitudinal-window. [The methods described in Plumb (1985) and Takaya and Nakamura (2001) are not readily applicable to finite-amplitude wave activity.]

3.3 Relationship to Impulse-Casimir wave activity

Another well-known measure of finite-amplitude local wave activity is Impulse-Casimir wave activity (ICWA), first introduced by Killworth and McIntyre (1985) and further developed by McIntyre and Shepherd (1987) and Haynes (1988). ICWA may be defined with respect to any zonally uniform, time-independent reference state in which PV (q_0) is a monotonic function of y. It is defined as

$$\tilde{A}_{\text{IC}}(x,y,z,t) = \int_0^{q^*(x,y,z,t)} \left(Y(q_0 + \hat{q}^*) - Y(q_0) \right) d\hat{q}^*, \tag{3.24}$$

where $q(x,y,z,t) \equiv q^*(x,y,z,t) + q_0(y,z)$, and $Y(q_0,z)$ is an inverse function of $q_0(y,z)$ for a given z. $\tilde{A}_{\rm IC}(x,y,z,t)$ obeys (Killworth and McIntyre, 1985; Haynes, 1988)

$$\frac{\partial \tilde{A}_{\rm IC}}{\partial t} = -e^{z/H} \nabla \cdot \left(\mathbf{F}^*_{\rm adv} + \mathbf{F}^*_{\rm EP} \right), \tag{3.25}$$

$$\mathbf{F}^*_{\rm adv} \equiv e^{-z/H} \left((u_0(y,z) + u^*) \tilde{A}_{\rm IC}, \quad v^* \tilde{A}_{\rm IC}, \quad 0 \right), \tag{3.26}$$

$$\mathbf{F}^*_{\rm EP} \equiv e^{-z/H} \left(\frac{1}{2} \left(v^{*2} - u^{*2} - \frac{R}{H} \frac{e^{-\kappa z/H} {\theta^*}^2}{\partial \tilde{\theta}/\partial z} \right), \quad -u^* v^*, \quad \frac{f\, v^* \theta^*}{\partial \tilde{\theta}/\partial z} \right), \tag{3.27}$$

where the asterisk denotes the local departure from the reference state. If q_0 is chosen to be identical with $Q(y,z)$, there is a close relationship between $\tilde{A}^*$ and $\tilde{A}_{\rm IC}$. As illustrated in Fig.3.2, on the y-q plane $\tilde{A}^*(x,y_1,z,t)$ is given by the area bounded by $q = Q(y_1,z)$, $y = y_1$ and the curve $q = q(x,y,z,t)$ (Fig.3.2a), whereas $\tilde{A}_{\rm IC}(x,y_1,z,t)$ is given by the area bounded by $q = q(x,y_1,z,t)$, $y = y_1$ and the curve $q = Q(y,z)$ (Fig.3.2b). When the eddy is of small-amplitude (i.e. $q(x,y,z,t) \approx Q(y,z)$), these two areas are similar and both converge to (3.11). At where $q(x,y,z,t) = Q(y,z)$ (nodes), they both vanish. However, once the PV gradient $\frac{\partial q}{\partial y}$ is reversed, $\tilde{A}^*$ becomes positive even at $q = Q(y,z)$ (Fig.3.2c), whereas $\tilde{A}_{\rm IC}$ remains zero (Fig.3.2d). In fact, $\tilde{A}^*$ tends to be greatest around the gradient reversal because both red and blue lobes in Fig.3.1b ($x = x_3$) contribute to it. Consequently, $\tilde{A}^*$ emphasizes the region of wave breaking more than $\tilde{A}_{\rm IC}$ does, as I will see in the next section.

Both wave activities obey similar equations [(3.21) and (3.25)] but while the ICWA equation is written entirely in terms of Eulerian quantities, the LWA equation involves line integrals and hence Lagrangian in the meridional. A crucial difference arising from this is an extra meridional advection term $\frac{\partial}{\partial y}(v^* \tilde{A}_{\rm IC}))$ in (3.26) which does not have a counterpart in (3.22). The meridional advection of $\tilde{A}^*$ is absorbed in the movement of PV contour and does not appear in (3.22). The extra term in (3.26) prevents $\tilde{A}_{\rm IC}$ from possessing an exact non-acceleration theorem (NZ10).

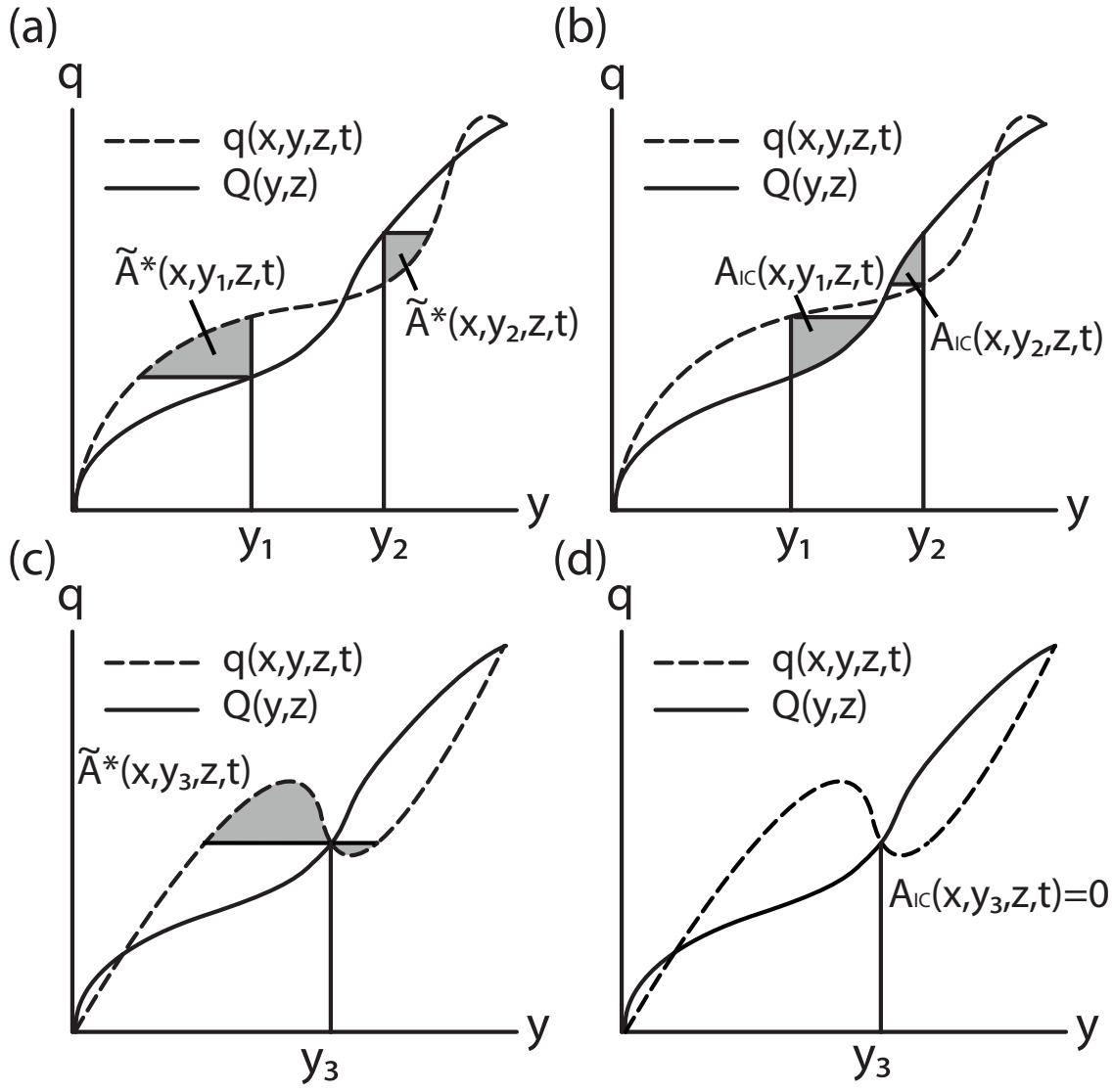

Figure 3.2: Comparison of $\tilde{A}^*$ and $\tilde{A}_{\rm IC}$. Curves indicate latitudinal cross sections of PV at fixed x and z. Solid curves: $Q(y,z)$. Dashed curves: $q(x,y,z,t)$. (a) Shaded areas indicate $\tilde{A}^*$ at $y=y_1$ and $y=y_2$. See (3.8). (b) Same as (a) but for $\tilde{A}_{\rm IC}$. See (3.24). (c) $q(x,y,z,t)$ involves gradient reversal. Shaded areas indicate $\tilde{A}^*$ at $y=y_3$. (d) Same as (c) but for $\tilde{A}_{\rm IC}$. $\tilde{A}_{\rm IC}$ at $y=y_3$ is zero.

3.4 Approximate local non-acceleration relation in the WKB regime

The non-acceleration relation (1.18) shows conservation of the sum of zonal-mean zonal wind and wave activity in a frictionless barotropic flow, but it does not tell whether the deceler-

ation of the zonal-mean wind is due to growth of a localized wave packet or simultaneous growth of multiple wave packets over longitudes. To understand the dynamics of a localized phenomenon such as blocking, it is desirable to characterize eddy-mean flow interaction over a regional scale.

To formulate local eddy-mean flow interaction in a form analogous to (1.18), I start by taking the density weighted vertical average of (3.21):

$$\frac{\partial}{\partial t}\left\langle \tilde{A}^* \right\rangle = -\frac{\partial}{\partial x}\left(\left\langle u_{\mathrm{REF}} \tilde{A}^* \right\rangle - \left\langle \int_0^\eta (u_e q_e) dy' \right\rangle + \frac{\left\langle v_e^2 \right\rangle - \left\langle u_e^2 \right\rangle}{2} - \frac{R}{2H}\left\langle \frac{e^{-\kappa z/H}\theta_e^2}{\partial \tilde{\theta}/\partial z} \right\rangle \right) - \frac{\partial}{\partial y}\left(-\left\langle u_e v_e \right\rangle \right) + \left. \frac{f\, v_e \theta_e}{H \partial \tilde{\theta}/\partial z} \right|_{z=0}, \tag{3.28}$$

where the angle bracket denotes the density weighted vertical average

$$\langle \cdots \rangle \equiv \frac{\int_0^\infty (\cdots) e^{-z/H} dz}{\int_0^\infty e^{-z/H} dz} = \frac{\int_0^\infty (\cdots) e^{-z/H} dz}{H}. \tag{3.29}$$

As will be shown in Section 3.6, because of the density weighting this column average mainly samples the troposphere. The corresponding vertically averaged zonal momentum equation is

$$\frac{\partial}{\partial t}\langle u \rangle = -\frac{\partial}{\partial x}\left\langle u_{\mathrm{REF}} u_e + u_e^2 \right\rangle - \frac{\partial}{\partial y}\langle u_e v_e \rangle + f \langle v_e \rangle - \frac{\partial}{\partial x}\langle \Phi_e \rangle, \tag{3.30}$$

where Φ_e is the eddy geopotential. I also introduce *local surface wave activity* $\tilde{B}^*$

$$\tilde{B}^*(x,y,t) \equiv -\frac{f}{H \partial \tilde{\theta}/\partial z} \int_0^{\eta(x,y,t)} \theta_e(x, y+y', t) dy' \Big|_{z=0}, \tag{3.31}$$

which is analogous to (3.8) but defined based on the meridional displacement of surface potential temperature contour. Note by definition $\tilde{B}^* \leq 0$ and its zonal average recovers the surface FAWA [NZ10, Wang and Nakamura (2015)]. $\tilde{B}^*$ obeys the equation

$$\frac{\partial \tilde{B}^*}{\partial t} = -\frac{\partial}{\partial x}\left(u_{\mathrm{REF}}(y,0)\tilde{B}^* - \frac{f}{H \partial \tilde{\theta}/\partial z} \int_0^{\eta(x,y,t)} (u_e \theta_e) dy' \Big|_{z=0} \right) - \left. \frac{f v_e \theta_e}{H \partial \tilde{\theta}/\partial z} \right|_{z=0}. \tag{3.32}$$

Adding (3.28), (3.30), and (3.32) one obtains

$$\begin{aligned}
&\frac{\partial}{\partial t}\left(\langle u\rangle + \langle \tilde{A}^*\rangle + \tilde{B}^*\right) \\
=&-\frac{\partial}{\partial x}\left(\langle u_{\mathrm{REF}}(u_e+\tilde{A}^*)\rangle + u_{\mathrm{REF}}(y,0)\tilde{B}^* - \left\langle \int_0^{\eta} (u_e q_e)dy' \right\rangle \right. \\
&\left. -\frac{f}{H\partial\tilde{\theta}/\partial z}\int_0^{\eta(x,y,t)} (u_e\theta_e)dy'\bigg|_{z=0} + \frac{1}{2}\left\langle u_e^2+v_e^2\right\rangle - \frac{R}{2H}\left\langle \frac{e^{-\kappa z/H}\theta_e^2}{\partial\tilde{\theta}/\partial z}\right\rangle + f\psi_e - \langle\Phi_e\rangle\right)
\end{aligned} \tag{3.33}$$

where ψ_e is barotropic streamfunction such that $\langle v_e\rangle = \frac{\partial\psi_e}{\partial x}$. Notice the zonal average of (3.33) gives

$$\frac{\partial}{\partial t}\left(\langle\bar{u}\rangle + \langle A^*\rangle + B^*\right) = 0, \tag{3.34}$$

a baroclinic extension of (1.18). Now define *regional average* over a longitudinal window of Δx, denoted by $[...]_{\Delta x}$

$$[g(x,y,t)]_{\Delta x} \equiv \frac{1}{\Delta x}\int_{x-\Delta x/2}^{x+\Delta x/2} g(x',y,t)dx'. \tag{3.35}$$

Averaging (3.33) over Δx would give

$$\frac{\partial}{\partial t}\left[\langle u\rangle + \left\langle \tilde{A}^*\right\rangle + \tilde{B}^*\right]_{\Delta x} = -\frac{1}{\Delta x}\left(\cdots\cdots\right)\Big|_{x-\Delta x/2}^{x+\Delta x/2}. \tag{3.36}$$

If the atmospheric wave packets satisfy the Wentzel-Kramers-Brillouin (WKB) approximation [Bühler (2014) Ch. 2] such that the wavelength is much smaller than the length-scale of the packet, by choosing Δx to be the wavelength, the right-hand side of (3.36) would be a small residual due to the slow modulation of wave properties in x. Thus on short timescales

$$\frac{\partial}{\partial t}\left[\langle u\rangle + \left\langle \tilde{A}^*\right\rangle + \tilde{B}^*\right]_{\Delta x} \approx 0. \tag{3.37}$$

This is the approximate local non-acceleration theorem in the WKB sense: the sum of the

phase-averaged barotropic LWA, surface LWA, and zonal wind remains unchanged in the conservative limit. If this is the case, growth of wave amplitude occurs at the expense of local zonal wind and vice versa. A migratory wave tends to slow down as it grows in amplitude because it decelerates the local westerly wind and weakens zonal advection. Furthermore, positive feedback might arise because the locally weakened westerly will arrest and accumulate more LWA from upstream, leading to even more deceleration of the flow (Swanson, 2000). Note that a corresponding non-acceleration theorem does not hold for $\tilde{A}_{\rm IC}$ because of the additional meridional flux term in (3.25). In the next section, I will compare LWA and ICWA using idealized numerical simulations in which finite-amplitude Rossby waves are allowed to interact with shear flow on a rotating sphere. The extent to which the above conservation law for LWA is satisfied will be examined. In Section 3.6, the LWA diagnostic is applied to meteorological reanalysis data to identify and analyze an atmospheric blocking event.

3.5 Numerical experiment

3.5.1 Experimental setup

The utility of the LWA diagnostic will be tested in a barotropic decay simulation of finite-amplitude Rossby waves as described by Held and Phillipps (1987) (hereafter HP87) and in Section 2.3.1 except that I impose, on top of the vorticity anomaly in (2.8), another wave with wavenumbers (m,n) = (4,6) to break the zonal symmetry and allow merging of wave packets. Here m and n are the zonal and total wavenumbers, respectively. The explicit form of ζ' (see Fig.3.3, top) is

$$\zeta' = \zeta_0 \cos\phi e^{-\left[\frac{\phi-\phi_m}{\sigma}\right]^2} \cos 6\lambda + \zeta_1(\sin^2\phi - 1)^2(11\sin^2\phi - 1)\cos 4\lambda, \qquad (3.38)$$

where ϕ is latitude, λ is longitude, $\zeta_0 = 8 \times 10^{-5}\mathrm{s}^{-1}$, $\zeta_1 = -9 \times 10^{-6}\mathrm{s}^{-1}$, $\phi_m = 45°\mathrm{N}$ and $\sigma = 10°$.

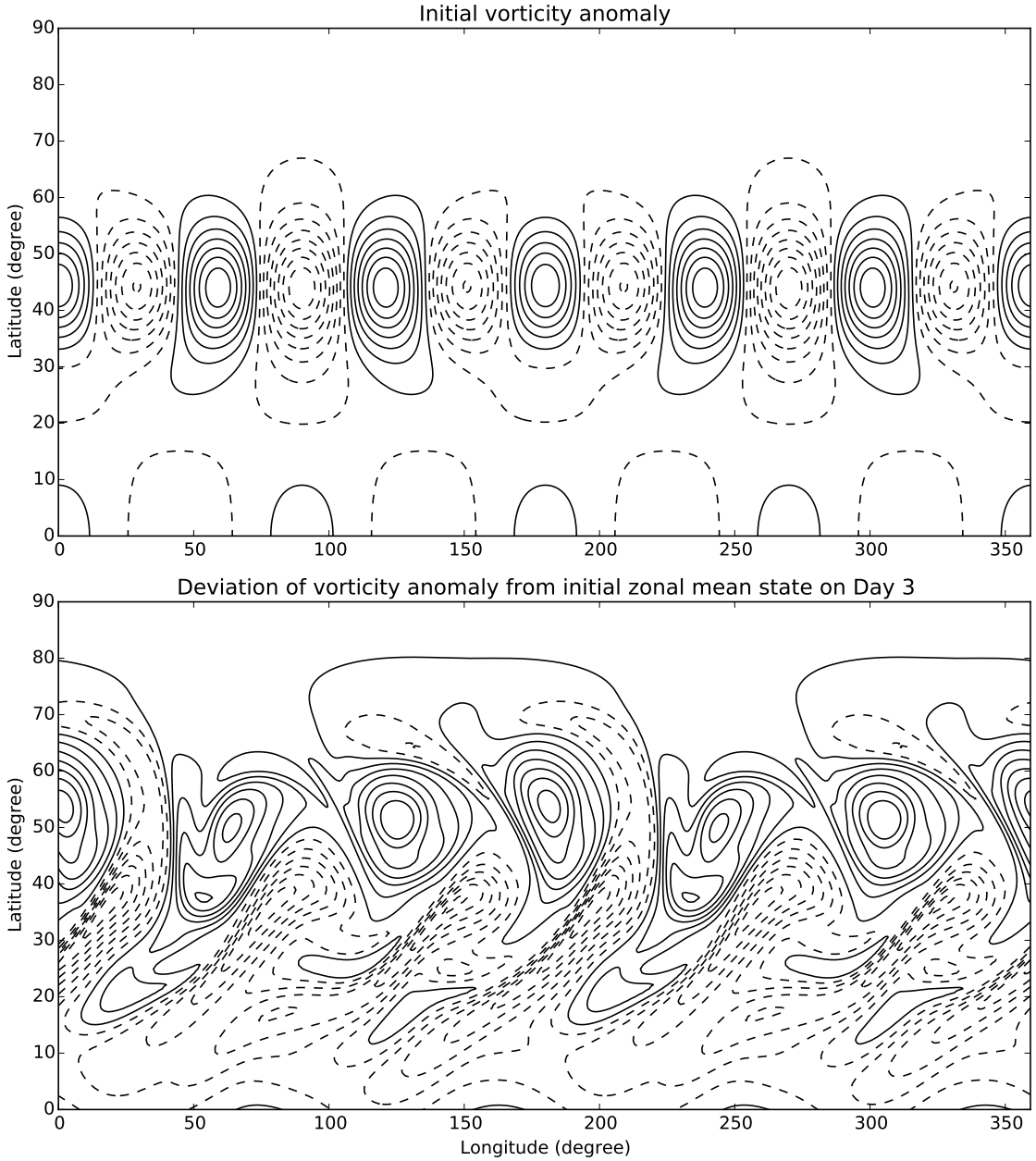

Figure 3.3: Top: Initial vorticity anomaly (3.38) for the barotropic decay experiment (contour interval: 8.25×10^{-6} s^{-1}; negative values are dashed). Bottom: Same as top but for the difference between the relative vorticity on Day 3 and the initial zonal-mean relative vorticity.

I discretize the equation with a standard spectral transform method truncated at T170

on a Gaussian grid with a resolution of 512×256. The Adams-Bashforth third-order scheme [see Durran (2013) Chapter 2.4] is used to integrate the equation with a time increment of $\Delta t = 360$ s until the major wave packet decays completely. The computation of $\tilde{A}^*$ and $\tilde{A}_{\mathrm{IC}}$ is implemented on instantaneous snapshots of vorticity field obtained from the simulation. Since the model is barotropic, the third dimension in the fluxes (3.22), (3.23), (3.26) and (3.27) is ignored, and potential temperature and surface LWA $\tilde{B}^*$ are set to zero. The local non-acceleration relation (3.37) is simplified to

$$\frac{\partial}{\partial t}\Big[u + \tilde{A}^*\Big]_{\Delta x} \approx 0. \tag{3.39}$$

3.5.2 Comparison between $\tilde{A}^*$ and $\tilde{A}_{\mathrm{IC}}$

The overall flow evolution is similar to that in HP87: the wave packet initially located on the north side of the jet axis splits into poleward- and equatorward migrating tracks, and as they approach critical lines on the flanks of the jet they produce wave breaking. The initial vorticity pattern consists of six pairs of positive and negative anomalies (Fig.3.3, top), but their strengths are not symmetric due to the addition of small-amplitude, secondary wave $(m, n) = (4, 6)$. As the wave packet begins to separate meridionally, six positive vorticity anomalies move northward whereas six negative anomalies move southward, and by day 3 the vorticity contours begin to overturn on the flanks of the jet. (Here, anomalies are defined as departures from the zonal mean of the initial state. See Fig.3.3, bottom.)

The snapshots of absolute vorticity, LWA ($\tilde{A}^*$) and ICWA ($\tilde{A}_{\mathrm{IC}}$), are shown for day 3 and 6 in Fig.3.4 over the Northern Hemisphere. The positive anomalies form isolated vortices around 50°N, whereas the negative anomalies develop marked anticyclonic tilt on the equatorward flank of the jet (Fig.3.4, top left). Both $\tilde{A}^*$ and $\tilde{A}_{\mathrm{IC}}$ identify large vorticity anomalies but there are substantial differences between their spatial distribution. $\tilde{A}^*$ emphasizes the largest positive anomalies, although they are shifted and elongated poleward from the actual locations of the vorticity anomalies (Fig.3.4, center left). This is a nonlocal effect

of $\tilde{A}^*$: the isolated vortices are indeed associated with a higher equivalent latitude. $\tilde{A}_{\rm IC}$ also picks up the isolated vortices but they tend to be much more compact and intense than $\tilde{A}^*$. Also, the structure of $\tilde{A}_{\rm IC}$ around the negative anomalies appears more filamentary than $\tilde{A}^*$. Part of this difference is due, as explained in the previous section (in Fig.3.2), to the fact that $\tilde{A}_{\rm IC}$ tends to suppress wave amplitude in the region of reversed vorticity gradient: for example, the value of $\tilde{A}_{\rm IC}$ drops from a maximum to zero to the north and south of isolated vortices. By day 6 (Fig.3.4, right), a pair of vortices start to merge poleward of the jet around $10^\circ - 110^\circ$ and $190^\circ - 290^\circ$E. In the $\tilde{A}^*$ plot, the merging vortices appear as one bulk structure, whereas in $\tilde{A}_{\rm IC}$ they are more fragmented. On the equatorward flank of the jet, wave breaking causes the negative vorticity anomalies to roll up. $\tilde{A}^*$ captures these emerging vortices faithfully but $\tilde{A}_{\rm IC}$ is highly filamentary around them. Similar filamentary structures of $\tilde{A}_{\rm IC}$ have been observed in previous analyses related to baroclinic life cycles and Rossby wave breaking (Magnusdottir and Haynes, 1996; Thuburn and Lagneau, 1999).

3.5.3 Local negative correlation between $\tilde{A}^*(x, y, t)$ and $u(x, y, t)$

For a zonal-mean state, the non-acceleration relation (1.18) describes conservative eddy-mean flow interaction: $\bar{u}$ accelerates at the expense of A^* and vice versa, thus their variation is antiphase. $u_{\rm REF} \equiv \bar{u} + A^*$ is constant in time if the dynamics is conservative, so any changes in $u_{\rm REF}$ are due to non-conservative processes; in the present case, they represent damping of FAWA through vorticity mixing (enstrophy dissipation by hyperviscosity). Since the initial condition (3.38) creates interference of zonal wavenumbers 4 and 6, the resultant flow has a zonal periodicity π. It is expected $[\chi(x, y, t)]_\pi$ [cf. (3.35)] for any physical quantity χ to be identical with the zonal mean. The question is whether the non-acceleration relation holds at a more regional scale $\Delta x < \pi$ as in (3.37). Although there is no strict periodicity below π due to the presence of multiple waves, $m = 6$ still remains a dominant zonal wavenumber so $\Delta x = \pi/3$ would be a reasonable choice of the averaging window. The values of $[u(x, y, t)]_{\Delta x}$ and $[\tilde{A}^*(x, y, t)]_{\Delta x}$ are computed between $x = 0^\circ$ and 60°E at 30°N and plotted as functions

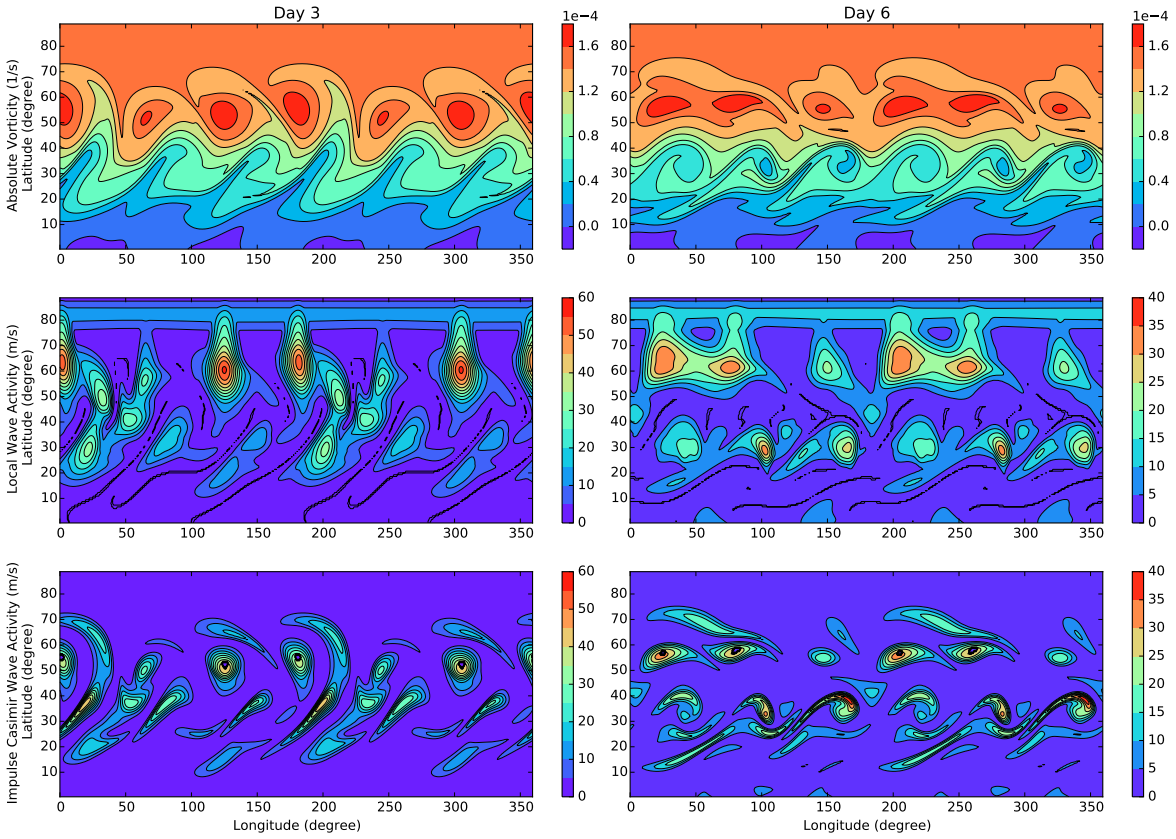

Figure 3.4: Longitude-latitude distributions of absolute vorticity (top, unit s^{-1}), $\tilde{A}^*$ (center, unit ms^{-1}) and $\tilde{A}_{IC}$ (bottom, ms^{-1}) from the barotropic decay experiment. Left column: day 3. Right column: day 6.

of time in the top panel of Fig.3.5. This particular latitude is chosen because a prominent wave breaking occurs around here (Fig.3.4).

The opposite tendency of the two quantities is evident, particularly during the early stage of simulation. Also plotted in the top panel are the sum $[u + \tilde{A}^*]_{\Delta x}$ and $u_{\mathrm{REF}}(y, t)$. The zonal averages of the two quantities are identical. The slow variation of u_{REF} reflects rearrangement of angular momentum by vorticity mixing (Fig.2.8), which is not included in (1.19). $[u + \tilde{A}^*]_{\Delta x}$ follows u_{REF} generally well, suggesting that the long-term changes in $[u+\tilde{A}^*]_{\Delta x}$ are due to mixing. The early disagreements are largely due to periodic modulation of $[\tilde{A}^*]_{\Delta x}$ by waves with wavelengths greater than $\pi/3$, but the range of fluctuation in $[u + \tilde{A}^*]_{\Delta x}$ is generally smaller than that of $[u]_{\Delta x}$ or $[\tilde{A}^*]_{\Delta x}$ alone, attesting to the overall

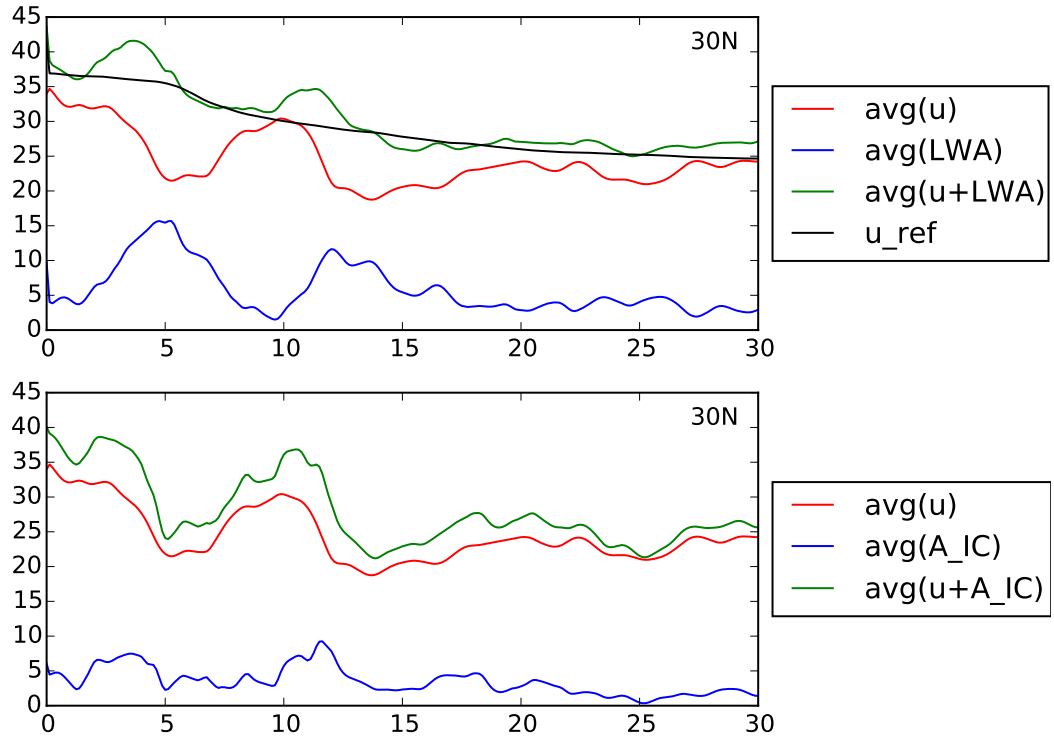

Figure 3.5: Top: Evolution of u (red) and $\tilde{A}^*$ (blue), $(u + \tilde{A}^*)$ (green) averaged over a fixed longitudinal window of 60° at 30° during the barotropic decay simulation. Also plotted is u_{REF} (black). Bottom: same as top but for $\tilde{A}_{\mathrm{IC}}$ (blue) and $u + \tilde{A}_{\mathrm{IC}}$ (green). The unit of the vertical axis is ms^{-1}.

validity of (3.37). Similar analysis is performed for $[\tilde{A}_{\mathrm{IC}}]_{\Delta x}$ in the bottom panel of Fig.3.5. Compared to $[\tilde{A}^*]_{\Delta x}$, $[\tilde{A}_{\mathrm{IC}}]_{\Delta x}$ varies much less, and its anticorrelation with $[u]_{\Delta x}$ is far less evident. Accordingly, the sum of $[\tilde{A}_{\mathrm{IC}}]_{\Delta x}$ and $[u]_{\Delta x}$ varies more in time. This demonstrates that the local non-acceleration relation (3.37) is generally not applicable to $\tilde{A}_{\mathrm{IC}}$.

Figure 3.6 extends the above analysis to the entire latitude circle by showing the longitude-time (Hovmöller) cross sections (Hovmöller, 1949) of $[u]_{\Delta x}$, $[\tilde{A}^*]_{\Delta x}$, and $[u+\tilde{A}^*]_{\Delta x}$ anomalies (departure from the time mean) at 30°N ($\Delta x = \pi/3$). Because of the averaging the fields are devoid of zonal wavenumber 6, the predominant structure in the unfiltered data. Instead, the analysis picks out the emerging wavenumber 2, which modulates the averaged quantities. The negative correlation between $[u]_{\Delta x}$ and $[\tilde{A}^*]_{\Delta x}$ is again evident, and it holds not

only in time but also in longitude (particularly strong in the early stage). This is important because it suggests that the non-acceleration relation (3.39) is applicable regionally. On the other hand, (3.39) is not perfect: $[u + \tilde{A}^*]_{\Delta x}$ shows significant residual in the bottom panel. As mentioned above, it is partly due to non-conservative effects (vorticity mixing). It also contains a wavenumber 2 component, which represents 'group propagation' of $[u+\tilde{A}^*]_{\Delta x}$ expressed by the right-hand side of (3.36). Although the amplitude of this variation is smaller than the amplitude of u or $\tilde{A}^*$, its non-negligible magnitude suggests that the scale separation required for (3.39) is insufficient. (In the present case the wavelength of the dominant wave is $\pi/3$ whereas the packet size is π.)

I have repeated the analysis varying Δx ($\pi/6$ and $2\pi/3$) and found (not surprisingly) that $[u+\tilde{A}^*]_{\Delta x}$ deviates from u_{REF} more when I reduce Δx further. Arguably this simulation is a special case in which the wave spectra are highly discrete. In a sense it is even less obvious how best to choose an optimal Δx when the waves have broader spectra. It will be shown in the next section that dealing with the real atmospheric data, horizontal averaging may actually be forgone.

3.6 Analysis of a blocking episode

Blocking is a phenomenon at midlatitudes in which a large-scale pressure anomaly remains stationary. The normal westerly winds in the mid- to upper troposphere are diverted meridionally along the blocking pattern and the wind within the block is often replaced by easterlies. Lejenäs and Økland (1983) observed that blocking occurs at longitudes where the latitudinal average of the zonal wind at 500 hPa is easterly. Tibaldi and Molteni (1990) added an additional requirement that the average wind be westerly poleward of the block. Such description of blocking based on reversal of zonal wind is a kinematic statement. Given the potential of (3.37) to quantify the slowing down of the flow by finite-amplitude eddies, the formalism is well suited for identifying and investigating blocking events with meteorological data based on dynamics.

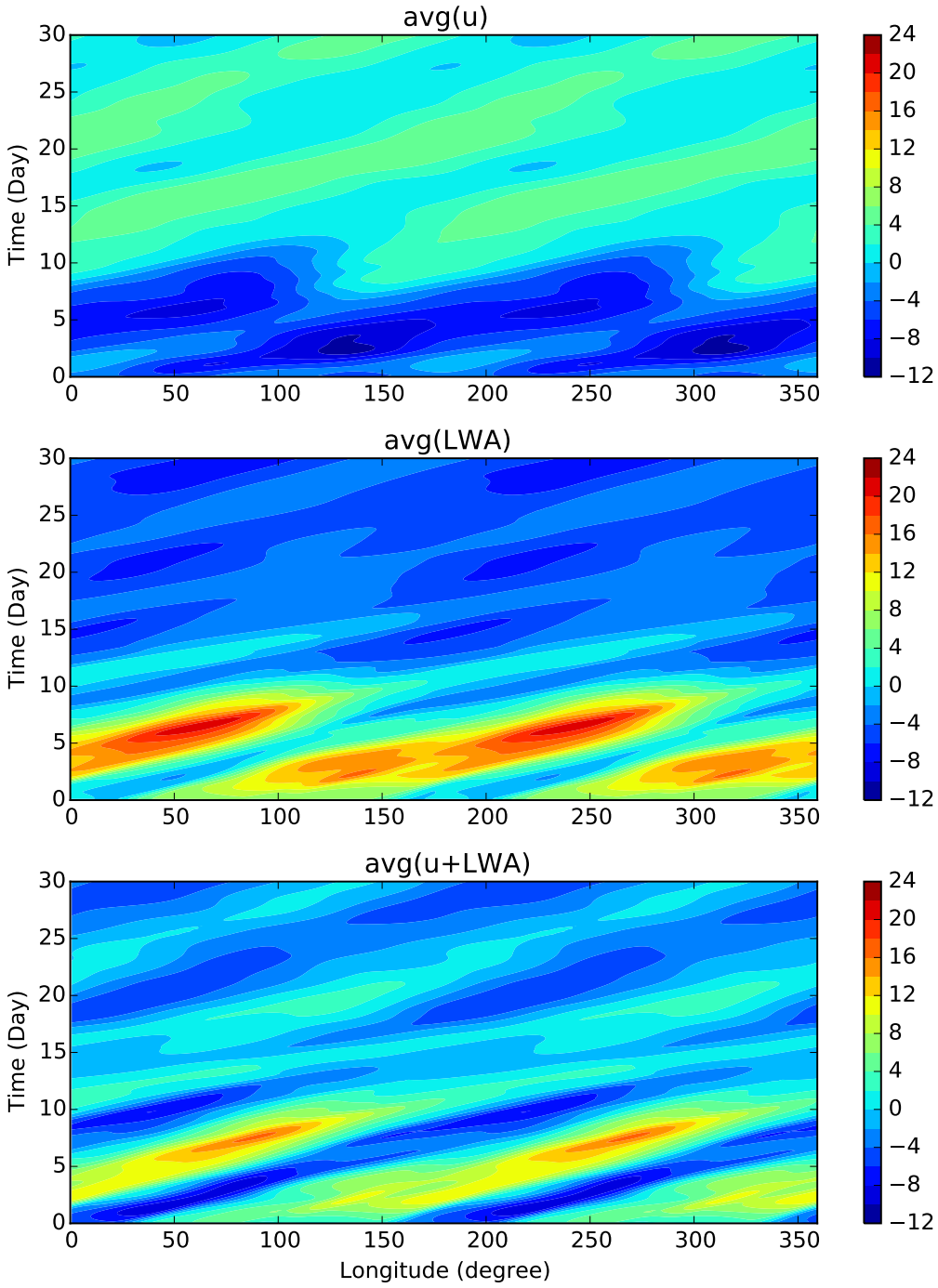

Figure 3.6: Top: Longitude-time (Hovmöller) cross section of u anomaly (departure from time-mean) at 30° during the barotropic decay simulation. At each instant the quantity is averaged over 60° window in longitude [$\Delta x = 60°$ in (3.35)]. Middle: same as top but for $\tilde{A}^*$. Bottom: same as top but for $(u + \tilde{A}^*)$. Unit: ms^{-1}.

In this section, I explore the extent to which the dynamics of a real blocking episode may be characterized based on the conservation relation (3.37). In particular, I will study the blocking episode that steered the Superstorm Sandy to the East Coast of US during October 2012 with the LWA formalism. The interior- and surface LWA as well as the zonal wind are evaluated from the European Centre for Medium-Range Weather Forecasts ERA-Interim reanalysis product (Dee et al., 2011) at a horizontal resolution of $1.5^\circ \times 1.5^\circ$.

First, I evaluate PV from (1.6) on 49 equally spaced pressure pseudoheight as described in Nakamura and Solomon (2010) (assuming $H = 7$ km). Then, I compute $\tilde{A}^*$ from (3.9). $\tilde{B}^*$ is computed from (3.31) except I have replaced the surface potential temperature with the potential temperature at 866 hPa to avoid the non QG effects in the boundary layer.

3.6.1 Overview of zonal wind and LWA in Northern Autumn 2012

Longitude-time (Hovmöller) diagrams for the barotropic components of zonal wind $\langle u \rangle$, LWA $\langle \tilde{A}^* \rangle + \tilde{B}^*$ and their sum at 42°N during this season are shown in Fig.3.7. Notice that in this analysis I am not using any horizontal average defined by (3.35). Indeed, the prevalent short streaks in LWA (middle panel) suggest an average eastward migration of LWA at about 11ms^{-1}, consistent with the phase speed of baroclinic waves (Williams and Colucci, 2010). Thus, I believe that the streak pattern in LWA partly reflects the phase structure. However, the eastward migration of LWA is occasionally interrupted by large-amplitude, quasi-stationary features. A close correspondence is observed between these large LWA events and the reversal of zonal wind (i.e. negative $\langle u \rangle$) in the left panel, although the magnitude of fluctuation in LWA is about twice as large as that of the zonal wind (notice the different color scales for the two quantities). The fluctuation of their sum (Fig.3.7, right column) has a smaller variation than $\langle \tilde{A}^* \rangle + \tilde{B}^*$. The simultaneous growth of LWA and the deceleration of zonal flow are characteristic of blocking. Remarkably neither does the unfiltered phase signal hinder the detection of blocking nor does removal of the phase by averaging improve the result significantly. It appears that LWA has no problem detecting the

packet structure of blocks without regional averaging (3.35). Part of the reason is that the last two terms in (3.33) nearly cancel in geostrophic balance and that the vertical averaging in the other right-hand side terms, when the phase surfaces are tilted vertically, achieves the same effect as the phase averaging.

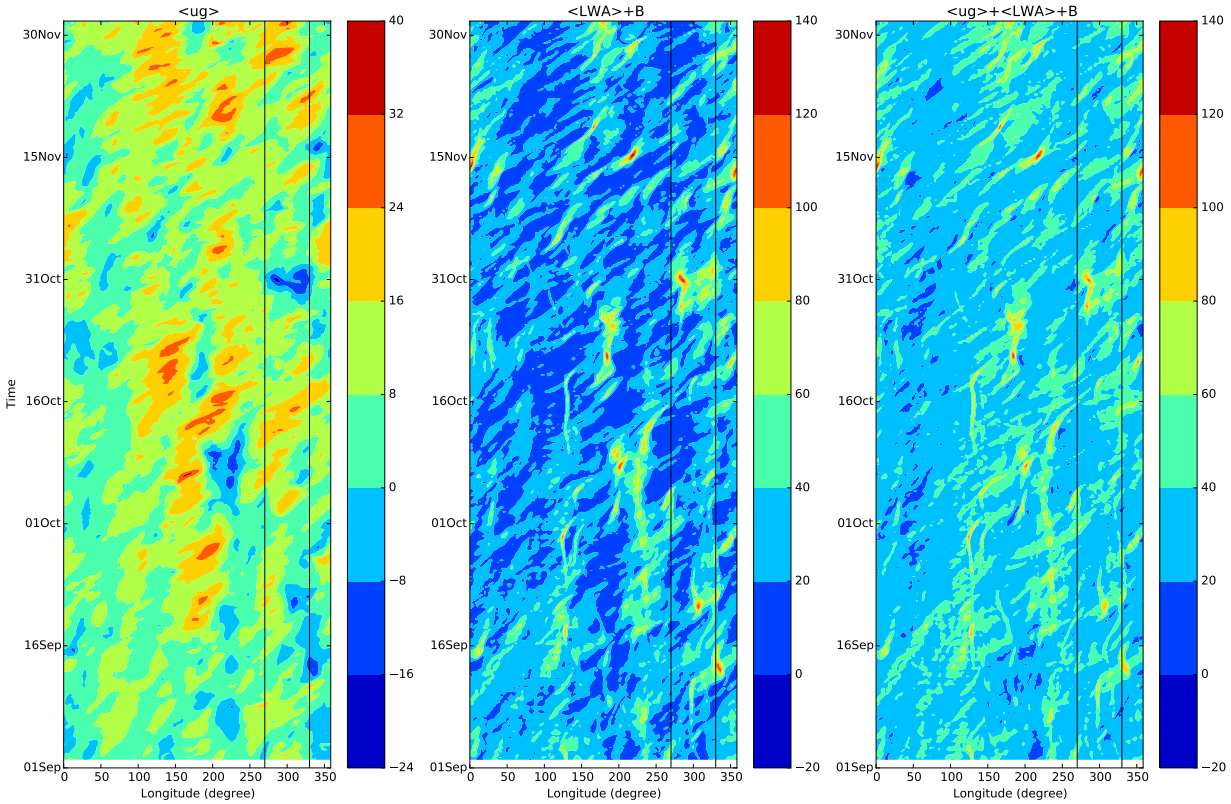

Figure 3.7: Hovmöller cross section of $\langle u \rangle$ (left), $\langle \tilde{A}^* \rangle + \tilde{B}$ (middle) and $\langle u \rangle + \langle \tilde{A}^* \rangle + \tilde{B}$ (right) at 42°N from September 1 to November 31, 2012. The vertical black lines bound the range of longitudes where the zonal average is taken to obtain the local non-acceleration relation. Unit: ms^{-1}.

3.6.2 Blocking episode around North American East Coast during 27 Oct - 2 Nov 2012

Now I focus on a single blocking episode that occurred during Oct 27-Nov 2 over the North Atlantic. (The longitudinal range of concern is marked by the black lines in Fig.3.7.) This episode was characterized by a persistent blocking pattern in the mid- to upper troposphere

and contributed to the steering of Superstorm Sandy at right angle to the East Coast of US (Blake et al., 2013). Figures 3.8 and 3.9 respectively show PV and the corresponding LWA ($\tilde{A}^*$) at 240 hPa. There is an intrusion of low-PV air poleward at 290°E and 40°N which remains stagnant longitudinally (relative to other eastward migrating features) for 2 days and eventually split into two asymmetric vortices. The smaller vortex that moves westward accompanied Sandy in-shore. The location and magnitude of the block are well-captured by high values of $\tilde{A}^*$ in Fig.3.9.

One might ask how the barotropic component (density-weighted vertical average) samples the vertical distribution of LWA associated with blocking. Figure 3.10 shows the vertical structure of $\tilde{A}^*$ (left) and density weighted LWA ($e^{-z/H}\tilde{A}^*$, right). Even though the pattern of blocking is apparent in $\tilde{A}^*$ only at the upper levels (i.e. 300-150 hPa), density weighting indeed brings out a vertically coherent structure of high LWA as shown in Fig.3.10 (right). Thus, what is observed in Fig.3.7 represents a persistent block affecting an entire troposphere and not just upper levels, both in terms of the accumulation of LWA and the deceleration of the flow.

To examine the extent to which the local non-acceleration relation accounts for the simultaneous accumulation of LWA and deceleration of zonal flow, in Fig.3.11, I show $\Delta\langle u\rangle$ (red), $\Delta(\langle\tilde{A}^*\rangle+\tilde{B}^*)$ (blue), and their sum (green), averaged longitudinally over $270°-330°$E (the longitudes bounded by the black lines in 3.7) at different latitudes within the meridional extent of the blocking episode. Here Δ denotes departure from the seasonal average. This graph is analogous to Fig.3.5 for the barotropic decay simulation. The correlation coefficient of the time series of $\langle u\rangle$ and $\langle\tilde{A}^*\rangle + \tilde{B}^*$ throughout the analysis period is displayed at the top left hand corners of each plot.

There are several remarkable features from the plots. First, there is a strong negative correlation in the time series of $\Delta\langle u\rangle$ (red) and $\Delta(\langle\tilde{A}^*\rangle + \tilde{B}^*)$ (blue), clearly indicating the antiphase covariation of the two quantities expected from the non-acceleration relation. This relation is particularly visible during the block (27 Oct - 2 Nov) when the amplitude

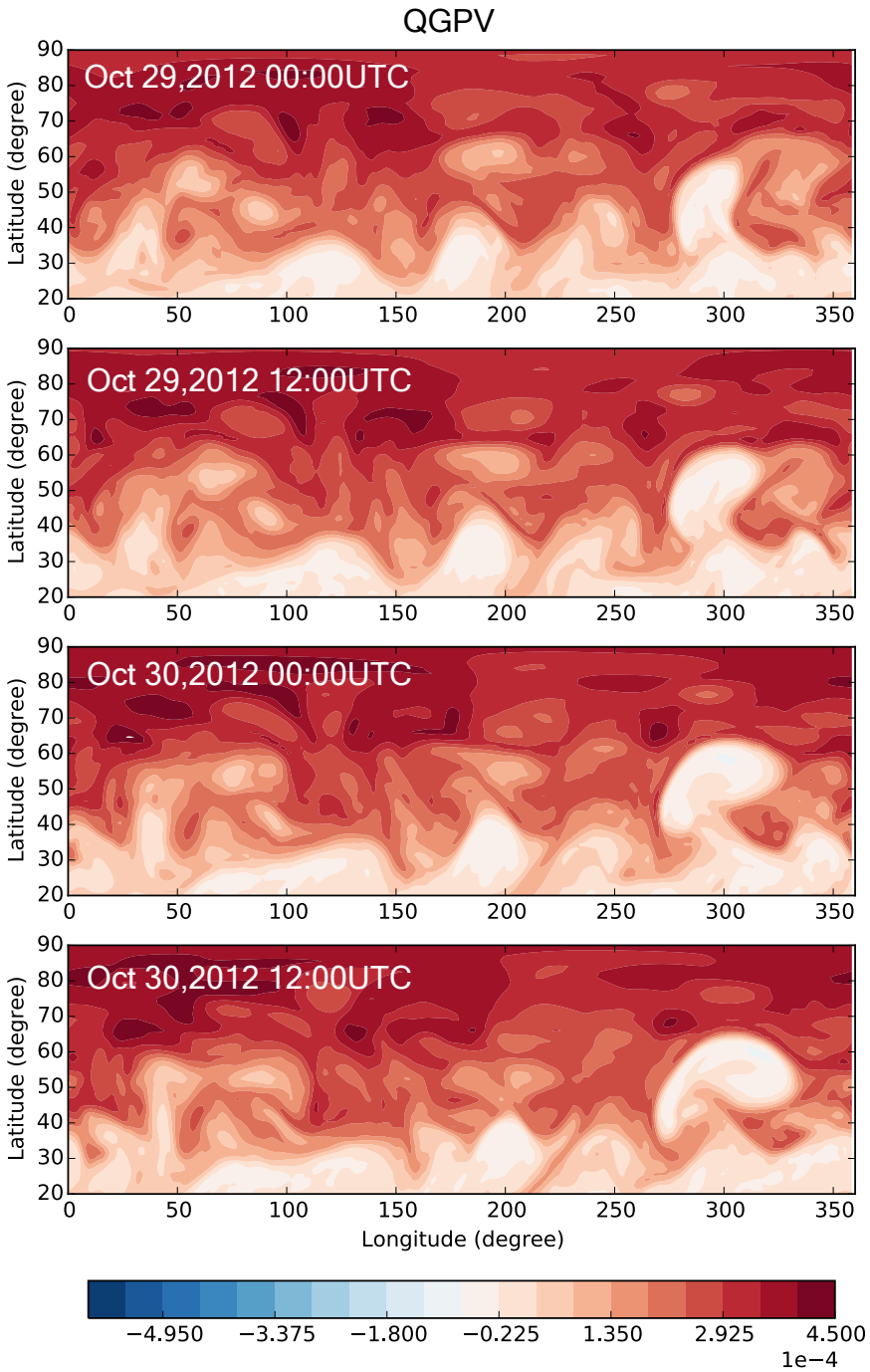

Figure 3.8: Evolution of QGPV at 240 hPa from 29 Oct 00:00 UTC to 30 Oct, 2012 12:00 UTC (with 12-hour interval). Unit: s^{-1}.

of the wave is large. Second, the 60°-longitudinal average of $\Delta(\langle u \rangle + \langle \tilde{A}^* \rangle + \tilde{B}^*)$ (green) weakly oscillates about zero except during the time of blocking formation when LWA grows

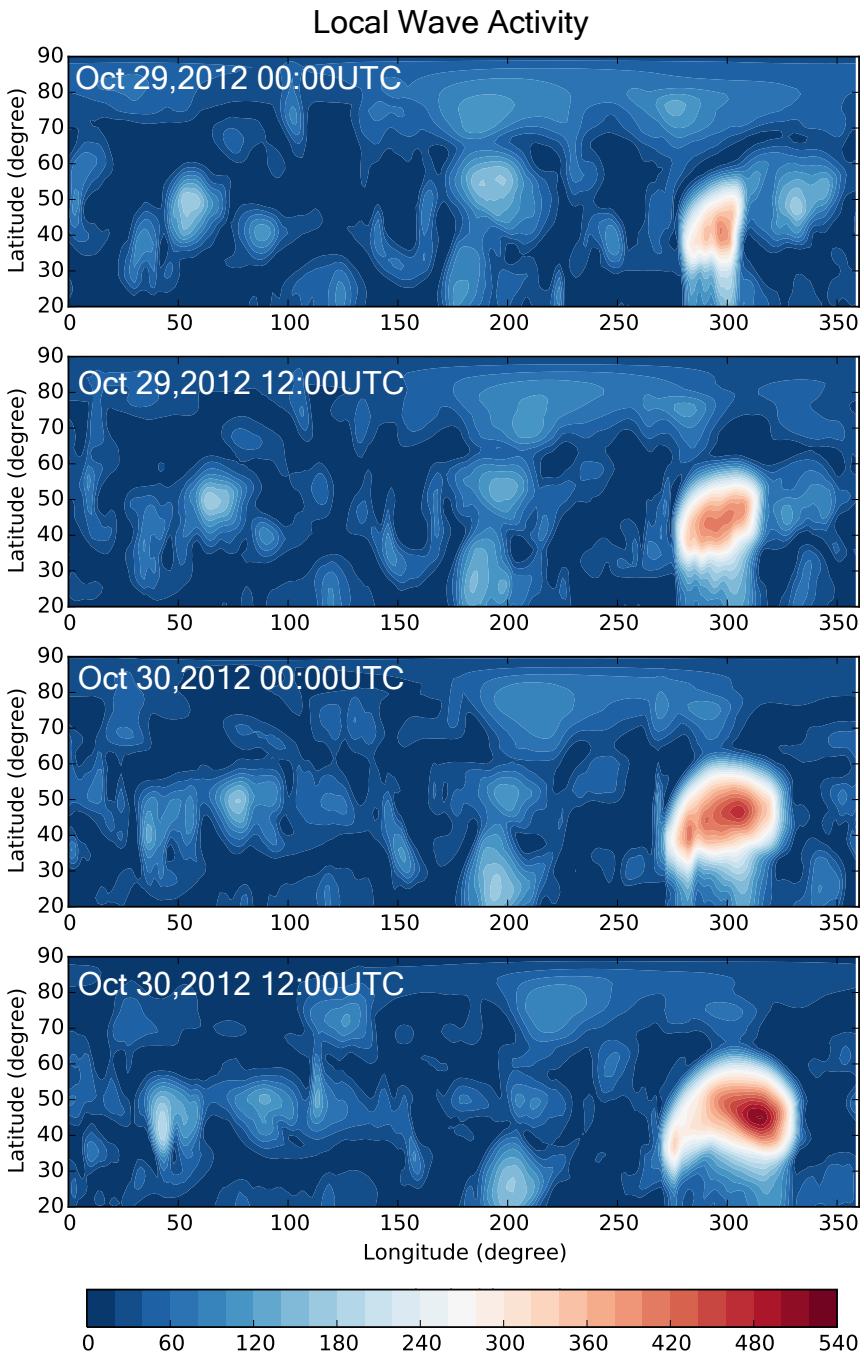

Figure 3.9: Evolution of local wave activity ($\tilde{A}^*$) at 240 hPa from 29 Oct 00:00 UTC to 30 Oct, 2012 12:00 UTC (with 12-hour interval). Unit: ms^{-1}.

large. Its peak value exceeds 20 ms^{-1}. Since (3.37) states that this quantity is approximately invariant in time under conservative dynamics, it suggests that conservative dynamics cannot

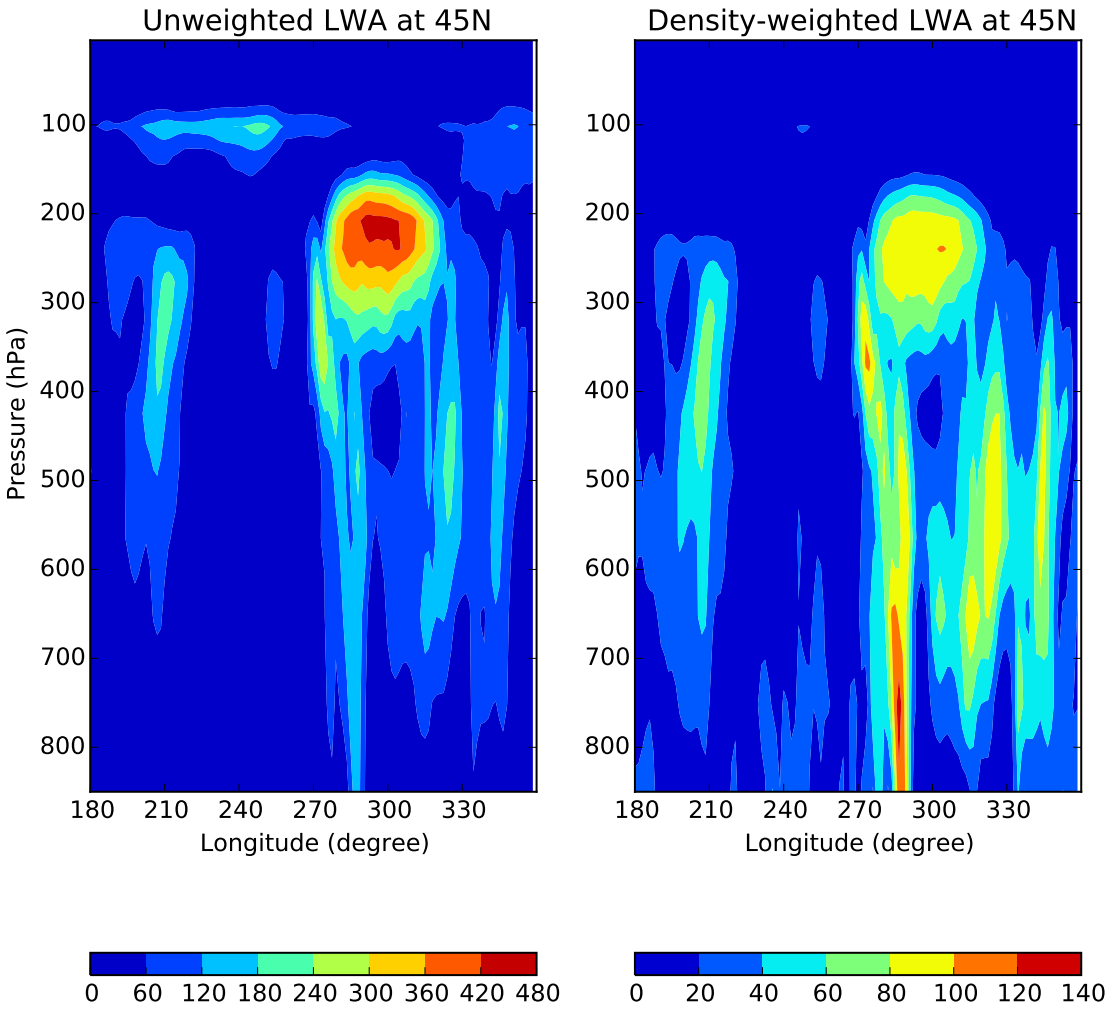

Figure 3.10: The vertical structures of (left) local wave activity ($\tilde{A}^*$) computed with (3.9) on each pressure surface and (right) density-weighted $\tilde{A}^*$ on 29 Oct, 2012 at 18:00 UTC at 45°N. The surface wave activity is obtained from data on the $p = 866$hPa level. Unit: ms^{-1}. Note different color scales for the two panels.

fully account for the occurrence of blocking. Given that the deceleration of the zonal flow has only half of the magnitude of the LWA anomaly, diabatic heating or other non-conservative processes are necessary to fuel the remainder of LWA anomaly associated with this block. The discrepancy does not depend strongly on the averaging window, suggesting that the violation of the WKB condition is not the primary cause of the deviation from (3.37).

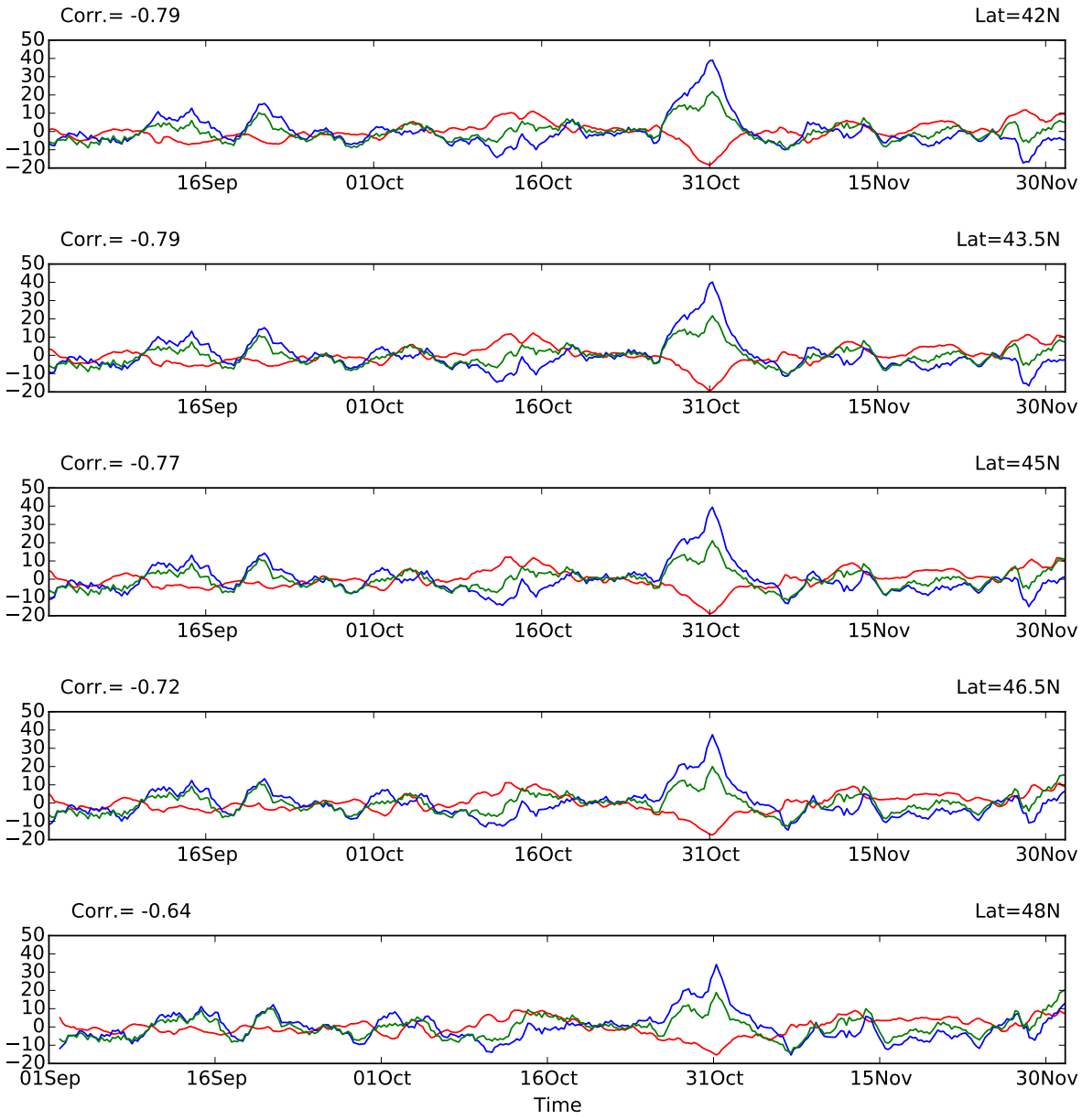

Figure 3.11: Evolution of the anomalies (departure from the seasonal mean) of $\langle u \rangle$ (red), $\langle \tilde{A}^* \rangle + \tilde{B}^*$ (blue), their sum (green) at various latitudes (marked at the top right corner) within $270^\circ - 330^\circ$E. The global zonal average of $\langle u \rangle + \langle \tilde{A}^* \rangle + \tilde{B}^*$ is also shown in black. The unit of the vertical axis is ms^{-1}. The correlation between the time profile of $\langle u \rangle$ and $\langle \tilde{A}^* \rangle + \tilde{B}^*$ are shown at the top left corner. See text for details.

3.7 Summary and discussion

I have generalized the notion of FAWA introduced by NZ10 to LWA, a diagnostic for longitudinally localized wave events, and tested its utility in both a barotropic model and meteorological data. A significant advantage of LWA over the existing wave activity measures is that it carries over the non-acceleration relation of FAWA to regional scales, albeit within the WKB approximation. This explicitly attributes local deceleration of the zonal flow to accumulation of wave activity.

A robust negative correlation is found between $\langle u \rangle$ and $\langle \tilde{A}^* \rangle + \tilde{B}^*$ in both a simulated wave breaking and an observed blocking event, suggesting that the quasi-adiabatic eddy-mean flow interaction is indeed of leading order importance in these weather events. Nevertheless, the variation of $\langle \tilde{A}^* \rangle$ during the blocking event is about twice as much as that of $\langle u \rangle$, which implies that not all LWA growth is accounted for by the simultaneous deceleration of the zonal flow. Diabatic and other non-conservative processes are responsible for half the budget of $\tilde{A}^*$ anomaly. This perspective is consistent with a recent study based on the formalism by NZ10 (Wang and Nakamura, 2015) that shows that the variability of eddy-driven jet in austral summer is largely dictated by conservative dynamics of wave-mean flow interaction but moderated by strong thermal damping of surface wave activity. Strong damping of (negative) $\tilde{B}^*$ would render the values and variability of $\langle \tilde{A}^* \rangle + \tilde{B}^*$ *higher* than those expected under the adiabatic condition, consistent with the present analysis. The precise role of nonadiabatic effects on blocking formation will be a subject of future work.

LWA dynamically connects the two criteria of blocking indices: (1) deceleration or even reversal of westerlies (Lejenäs and Økland, 1983; Tibaldi and Molteni, 1990) and (2) large amplitude of anomalies or gradient reversal in either geopotential height (at 500 hPa) (Barnes et al., 2012; Dunn-Sigouin and Son, 2013) or potential temperature on constant potential vorticity surface (2 PVU) (Pelly and Hoskins, 2003). [A comparison between eddy enstrophy, LWA, and 500 hPa geopotential height for a snapshot on Oct 30, 2012, 18:00UTC is shown in Fig.3.12 for reader's reference.] Hoskins et al. (1985) suggests that meridional gradient

reversal of potential temperature on a constant PV surface could imply a reversal of westerlies via the invertibility principle, but such a relation is not explicit. LWA can potentially serve as a blocking index because a large LWA will automatically leads to a significant deceleration of local zonal wind, to the extent that non-acceleration relation holds.

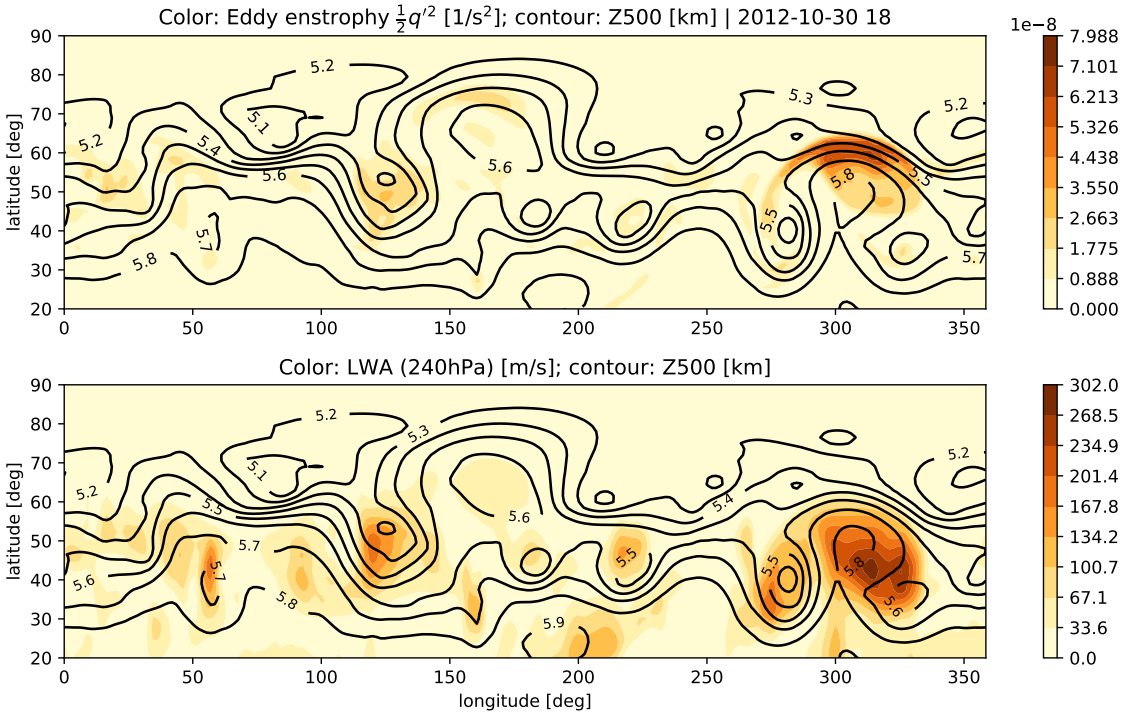

Figure 3.12: Top panel: (Color) local eddy enstrophy $\frac{1}{2}q'^2$ at 240 hPa and (contour) geopotential height at 500 hPa (Z500) for an instantaneous snapshot taken on Oct 30, 2012 18:00UTC. The eddy enstrophy is largest at the poleward side of the block at 300°E, where the Z500 contours are densest. Bottom panel: same as top panel except the quantity displayed in color is $\tilde{A}^*$ at 240 hPa. It captures not only the anti-cyclone, but also the two cyclones at 275°E and 330°E. Compared to the eddy enstrophy, $\tilde{A}^*$ performs better to highlight the regions where the zonal flow is disrupted by eddies.

CHAPTER 4

APPLICATION OF LOCAL WAVE ACTIVITY THEORY TO DIAGNOSE STORM TRACK VARIABILITY IN BOREAL WINTER

4.1 Introduction

Migratory weather systems populate the storm track regions of Earth's midlatitudes and affect the lives of billions (Chang et al., 2002; Shaw et al., 2016). In the Northern Hemisphere, storm tracks are localized over the Pacific and Atlantic sectors, whereas in the Southern Hemisphere, they are more zonally spread over the Southern Ocean (Hoskins and Hodges, 2002, 2005). Surface orography contributes significantly to the difference in the spatial structures of the storm tracks through stationary Rossby waves (Hoskins and Karoly, 1981; Held and Ting, 1990; Held et al., 2002; Wilson et al., 2009). Storm tracks are generally more active in winter when the pole-to-equator and land-sea temperature gradients enhance baroclinicity, although the midwinter suppression of the North Pacific storm activity is a notable exception (Nakamura, 1992).

Commonly used metrics of storm track activities include the Eady growth rate (Lindzen and Farrell, 1980), variance in highpass sea level pressure and geopotential height (Nakamura, 1992), transient eddy kinetic energy (EKE) (Orlanski, 1998; Deng and Mak, 2006) and aggregate potential vorticity (PV) anomalies contributed from individual storms (Hoskins and Hodges, 2002, 2005). To elucidate the underlying dynamics with meteorological data, metrics with known budget components are useful since they allow breakdown of the contributions from different physical processes. For example, Chang (2001) applies the budgets of EKE and wave activity flux to the Southern Hemisphere storm tracks and shows that the upstream generation of baroclinic wave activity maintains the downstream development of wave packets.

The wave activity flux diagnostic (Plumb, 1985; Takaya and Nakamura, 2001) is widely used to describe the 3D propagation of Rossby wave packets. However, its derivation assumes that the wave amplitude is small. While the wave activity flux is readily calculable from data, the budget of wave activity cannot be closed with the small-amplitude assumption: it is dominated by triple products of eddy quantities at finite amplitude, and the (small-amplitude) wave activity itself becomes unreliable as the background PV gradient is reversed [Solomon and Nakamura (2012); also Section 2.3].

In Chapter 3, I introduced finite-amplitude local wave activity (LWA) to describe eddy-mean flow interaction on regional scales. LWA generalizes the small-amplitude theory to eddies of arbitrary amplitude with a simple, closed budget. Both LWA and its eddy forcing terms are calculable from meteorological data, and the residual of the budget quantifies the net non-conservative processes. As demonstrated in Chapter 3, LWA can detect and follow the life cycle of anomalous wave events (see Figs. 3.9 and 3.12), while it distinguishes itself from other detection methods based on the flow geometry [e.g. Sobel and Plumb (1999), Riviere et al. (2010), Barnes and Hartmann (2012), Chen et al. (2015), etc.] in that it possesses a simple budget that applies at arbitrary wave amplitudes.

In this chapter, I analyze the column budget of LWA with the European Centre for Medium-range Weather Forecasts (ECMWF) ERA-Interim product (Dee et al., 2011) for the Northern Hemisphere winter to study the maintenance and variability of the Pacific and Atlantic storm tracks. A method will be introduced to decompose LWA into stationary and transient eddy contributions. As we will see, the transient-eddy component of LWA is consistent with, but better-behaved than, the small-amplitude transient wave activity defined by Plumb (1986). I will also perform spectral analysis of the LWA budget for synoptic to intraseasonal timescales over the two oceans.

4.2 The finite-amplitude local wave activity (LWA)

4.2.1 Definition of LWA in spherical coordinates

As discussed in Chapter 3, LWA extends the finite-amplitude wave activity (FAWA) theory of NZ10, formulated based on the conservation of QGPV on isobaric surface in a rotating, stratified atmosphere. FAWA measures the net 'exchange' of QGPV substance across latitude circles by eddies (Figs. 1.3 and 3.1). In spherical coordinates the interior LWA [(3.8)] becomes

$$\tilde{A}^*(\lambda,\phi,z,t) = -\frac{a}{\cos\phi}\int_0^{\Delta\phi} q_e(\lambda,\phi,\phi',z,t)\cos(\phi+\phi')d\phi' \qquad z>0, \tag{4.1}$$

where a is the radius of the planet, (λ, ϕ, z) defines longitude, latitude and pressure pseudo-height [$z \equiv -H\ln(p/p_0)$, p is pressure, $p_0 = 1000$ hPa and $H = 7$ km is assumed]. $q_e(\lambda,\phi,\phi',z,t) \equiv q(\lambda,\phi+\phi',z,t) - q_{\rm REF}(\phi,z,t)$ is an 'eddy' component of the QGPV q, defined as the departure from a zonally symmetric, Lagrangian-mean reference state $q_{\rm REF}(\phi,z,t)$ at equivalent latitude ϕ [see Appendix C for details]. In the above, ϕ' is the latitudinal displacement from ϕ. $\Delta\phi(\lambda,\phi,z,t)$ is the meridional displacement of the QGPV contour $q = q_{\rm REF}$ from the latitude circle at ϕ (see Fig.3.1). With this definition, $\tilde{A}^*$ is positive definite and its zonal average recovers FAWA [(1.14),(3.7)]. Unlike previous studies with the FAWA formalism [e.g. Nakamura and Solomon (2010), Wang and Nakamura (2015), hereafter NS10 and WN15, respectively], the equivalent latitude and the reference state in this study are defined in a hemispheric domain, with the assumption that the effect of inter-hemispheric exchange of QGPV on the mid-latitude dynamics is insignificant.

Here I focus on the horizontal distribution of the vertical column average of LWA and its fluxes weighted by air density, which I evaluate by the density-weighted averaging operation $\langle(...)\rangle$ defined in (3.29).

4.2.2 Comparison between instantaneous $\langle \tilde{A}^* \rangle$ and $\langle \mathrm{EKE} \rangle$

LWA measures the meridional displacement of the QGPV substance. Unlike EKE, it is not a measure of how energetic eddies are locally: the two metrics quantify different aspects of eddies. To illustrate, Fig.4.1 compares daily snapshots of $\langle \tilde{A}^* \rangle$ and $\langle \mathrm{EKE} \rangle$, together with the 500 hPa geopotential height (Z500) contours. During this period (December 14-17, 2010) there were a persistent anticyclone over the central Pacific ($30-60°$N, 180°) and a cyclone forming over the Gulf of Alaska ($45-60°$N, 160°W). $\langle \tilde{A}^* \rangle$ attains maxima at the centers of both features, where the zonal flows are most obstructed. This is consistent with the theoretical expectation that LWA negatively covaries with the zonal flow (Figs. 3.11). $\langle \mathrm{EKE} \rangle$, in contrast, attains maxima around the features where the Z500 contours are densest (i.e. where the geostrophic flow is most energetic).

To emphasize the relationship between $\langle \tilde{A}^* \rangle \cos\phi$ and $\langle u \rangle \cos\phi$ in the storm track regions, I show in Fig.4.2 a map of seasonal covariance between the two quantities (color) together with the time-mean $\langle u \rangle \cos\phi$ for the months of December-February. The covariance is predominantly negative, as one might expect from the local non-acceleration relation; that is, when LWA is large, westerlies are weak. Furthermore, the negative covariance is strongest (indicated by blue) in the exit (diffluent) region of the jet stream in both storm tracks. Therefore these are the regions in which eddy-zonal flow interaction is most pronounced.

4.2.3 Budget equations of LWA and zonal wind

The column budget equations for the interior zonal wind u and LWA $\tilde{A}^*$ read:

$$\underbrace{\frac{\partial}{\partial t}\langle u \rangle \cos\phi}_{\substack{\text{zonal wind}\\ \text{tendency}}} \approx \underbrace{-\frac{1}{a}\frac{\partial F_u}{\partial \lambda}}_{\substack{\text{zonal wind}\\ \text{zonal flux}\\ \text{conver-}\\ \text{gence}}} \underbrace{-\frac{1}{a\cos\phi}\frac{\partial}{\partial \phi'}\langle u_e v_e \cos^2(\phi+\phi') \rangle}_{\substack{\text{meridional eddy}\\ \text{momentum}\\ \text{flux convergence}}} + \underbrace{G_u}_{\substack{\text{ageostrophic}\\ \text{Coriolis}\\ \text{torque}}} \underbrace{+\langle \dot{u} \rangle \cos\phi}_{\text{residual}}, \quad (4.2)$$

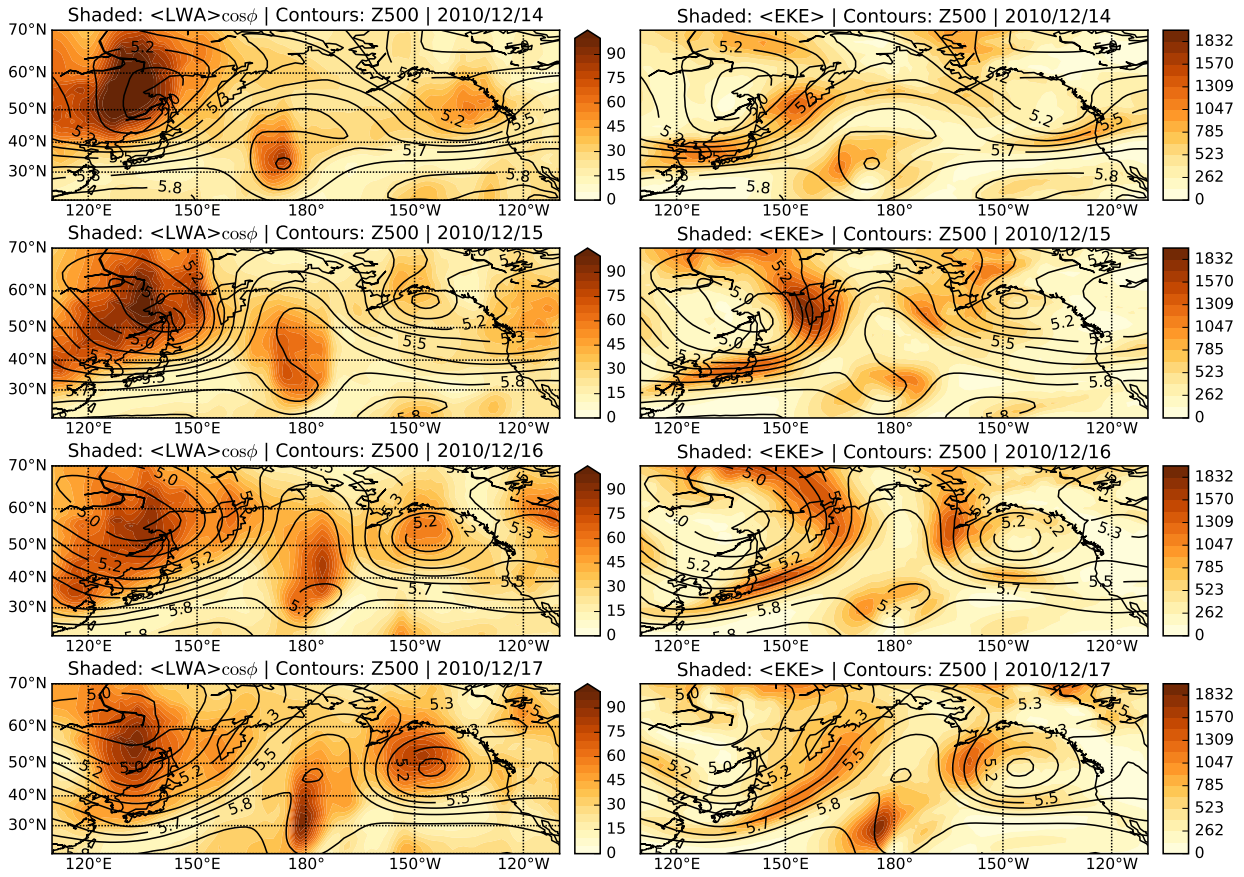

Figure 4.1: Left column: Daily mean of $\langle \tilde{A}^* \rangle \cos\phi$ (shaded) and 500 hPa geopotential height in km (contour) over the Pacific. The four panels correspond to, from top down, December 14, 15, 16 and 17, 2010, respectively. Right column: Same as left except that the shading indicates $\langle \text{EKE} \rangle$. Here EKE=$\frac{1}{2}\overline{u'^2 + v'^2}$, where u and v are the zonal and meridional wind velocities, whereas $\overline{(...)}$ and $(...)'$ denote the zonal mean and departure from it, respectively. The units are ms^{-1} for $\langle \tilde{A}^* \rangle \cos\phi$ and $\text{m}^2\ \text{s}^{-2}$ for $\langle \text{EKE} \rangle$. Data source: ECMWF ERA-Interim reanalysis.

$$\underbrace{\frac{\partial}{\partial t}\langle \tilde{A}^* \rangle \cos\phi}_{\text{LWA tendency}} \approx \underbrace{-\frac{1}{a}\frac{\partial F_A}{\partial \lambda}}_{\substack{\text{zonal LWA} \\ \text{flux con-} \\ \text{vergence}}} + \underbrace{\frac{1}{a\cos\phi}\frac{\partial}{\partial \phi'}\langle u_e v_e \cos^2(\phi+\phi') \rangle}_{\substack{\text{meridional eddy} \\ \text{momentum} \\ \text{flux divergence}}} + \underbrace{\frac{f\cos\phi}{H}\left(\frac{v_e \theta_e}{\partial \tilde{\theta}/\partial z}\right)_{z=0}}_{\substack{\text{low-level eddy} \\ \text{meridional heat flux}}} + \underbrace{\langle \dot{\tilde{A}}^* \rangle \cos\phi}_{\text{residual}}, \tag{4.3}$$

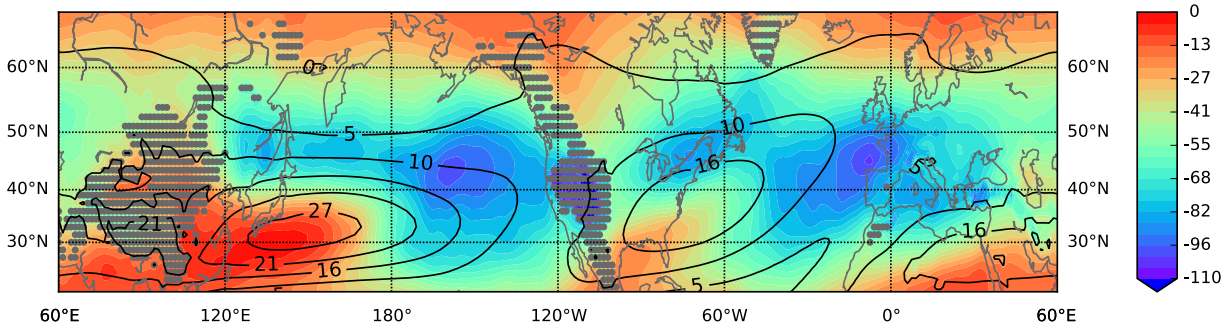

Figure 4.2: Color: December-January-February climatology of covariance of the column averaged LWA $\langle \tilde{A}^* \rangle \cos\phi$ and zonal wind $\langle u \rangle \cos\phi$. Unit: $m^2 s^2$. Note that the maximum value in the color scale (red) is zero. Column averaged LWA and zonal wind is computed with 6-hourly time-series, then their covariance is computed for the 3-month period. Solid contours: DJF climatology of the column averaged zonal wind multiplied by cosine of latitude. Unit: ms^{-1}. Based on the 1979-2015 ECMWF ERA-Interim reanalysis. The stippled regions in which the surface topography exceeds 1 km are excluded from analysis.

where (u, v, θ) define the zonal and meridional wind velocities and potential temperature. The subscript e denotes the departure from the reference state ('eddy'), F_u and F_A are respectively the column-averaged zonal fluxes of zonal wind and LWA, G_u is the Coriolis torque of the ageostrophic meridional wind (see Appendix D for the full expressions), f is the Coriolis parameter, $\tilde{\theta}(z,t)$ is the area-weighted average of potential temperature over the Northern Hemisphere, and $\dot{u}$ and $\dot{\tilde{A}}^*$ represent non-conservative contributions. [See Appendix D to F for derivations and computation.] The above equations generalize (3.30) and (3.28) for spherical coordinates. The zonal LWA flux F_A includes advective fluxes [the first two terms in (D.11) in Appendix D] that are cubic (or higher) in eddy products. A positive zonal LWA flux convergence indicates that wave activity from upstream are accumulating locally instead of being advected downstream. The second RHS term of (4.3) represents the local transfer of barotropic momentum to and from the zonal wind. The third term is the upward wave activity input from the surface. The zonal convergence of the last term in F_A [(D.11)], together with the second and third RHS terms of (4.3) make up the column average of the 3D E-P flux convergence. The last term of (4.3) represents non-conservative sources-sinks of LWA, including diabatic heating, dissipation through mixing, radiative and Ekman

damping. The budget of surface wave activity associated with the meridional displacement of low-level potential temperature will not be analyzed in this study. The main contribution to the column average quantities over the oceans comes from the upper troposphere, where eddy amplitudes are greatest, even with the density-weighing that decreases with height (3.29) (Fig.3.10).

The tendency terms in (4.2)-(4.3) are negligible upon time averaging over a season (December-February in this study). Denoting such time averaging by $[(\cdot)]$, (4.3) becomes:

$$0 \approx -\frac{1}{a}\frac{\partial[F_A]}{\partial\lambda} + \frac{1}{a\cos\phi}\frac{\partial}{\partial\phi'}\left[\langle u_e v_e \cos^2(\phi+\phi')\rangle\right] + \frac{f\cos\phi}{H}\left[\left(\frac{v_e\theta_e}{\partial\tilde{\theta}/\partial z}\right)_{z=0}\right] + \left[\langle\dot{\tilde{A}}^*\rangle\right]\cos\phi. \tag{4.4}$$

This steady-state budget describes the balance between the flux convergence (the first three RHS terms) and sources-sinks of LWA (the last term), which will be evaluated in Fig.4.11 below.

To examine the frequency dependence of the budget, I compute the cospectra (i.e. the in-phase signal of cross-spectra) between the LHS and each of the RHS terms of (4.2) and (4.3). I apply this spectral analysis after averaging each term in the equations over the respective spatial domain. See Appendix G for the definition of the spatial domains of averaging. The aim here is to characterize the LWA budget of an entire region that encompasses a storm track, rather than that of individual weather systems. The cospectrum of two quantities A and B will be denoted by Cosp(A,B) in the figure legends. The overall impact of non-conservative processes on LWA is estimated as the residual of the budget. No further breakdown of the non-conservative processes will be attempted. The residual also contains analysis errors (sampling errors, non-QG effects, truncation errors, etc.), which will not be quantified in this study. As we will see, the residual has nontrivial contributions to the LWA budget.

4.3 Results

4.3.1 Climatology of LWA in the boreal winter

Figure 4.3 shows the December-January-February climatology (1979-2015) of the column averaged LWA $\langle \tilde{A}^* \rangle \cos\phi$ (shades) and zonal wind $\langle u \rangle \cos\phi$ (contours). $\langle \tilde{A}^* \rangle \cos\phi$ is large on the poleward flanks of barotropic zonal jets over the storm track regions. $\langle \tilde{A}^* \rangle \cos\phi$ attains local maxima over (1) the east side of Mongolian Plateau, (2) the Hudson Bay and (3) the Norwegian Sea.

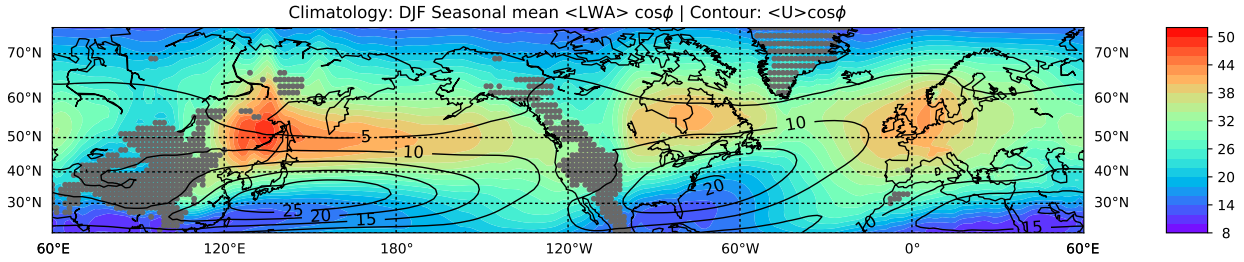

Figure 4.3: (Shaded) Seasonal (DJF) climatology of $\langle \tilde{A}^* \rangle \cos\phi$ and (contours) seasonal (DJF) climatology of $\langle u \rangle \cos\phi$. Both quantities have the unit (ms^{-1}). Regions masked by the gray stipples, where the topography is higher than 1 km (i.e. $z_s > 1$ km), have been excluded from analysis.

Note that this seasonal-mean LWA includes contributions from both stationary and transient eddies. Decomposition of LWA and its fluxes into stationary and transient eddy contributions is not straightforward partly because the definition of LWA [(4.1), see also (C.2) and (C.3) in Appendix C] requires a reference state based on the Lagrangian mean that does not commute with the Eulerian time mean.

One might attempt to define the stationary eddy contribution to LWA by applying (C.2) and (C.3) to the time-mean QGPV field. To ensure positive definiteness of LWA and its zonal mean, FAWA, the reference state q_{REF} must be computed from the time-mean QGPV field using the method outlined in Section 4.2.1 and Appendix C. This q_{REF}, however, is not the same as the time mean of q_{REF} computed from the full QGPV, because the Eulerian time mean does not commute with the Lagrangian mean used to define q_{REF}. In other words,

'stationary eddy' and 'total eddy' LWAs are based on different reference states, undermining the interpretation of the former as a fraction of the latter. To justify such decomposition of LWA into stationary- and transient-eddy components, one shall confirm that the time mean of q_{REF} does not deviate much from q_{REF} computed from the time mean of q. I denote the reference state q_{REF} based on the total QGPV field q as $q_{\mathrm{REF}}(q)$ and the DJF mean as [...]. Figure 4.4 shows (a) climatology of $q_{\mathrm{REF}}([q])$, i.e. the reference state computed from the DJF-mean q, (b) climatology of $[q_{\mathrm{REF}}(q)]$, i.e. the DJF mean of q_{REF} based on the full QGPV, and (c) the ratio of the maximum absolute difference (over 37 winters) between $q_{\mathrm{REF}}([q])$ and $[q_{\mathrm{REF}}(q)]$ to climatology of $[q_{\mathrm{REF}}(q)]$. The solid black line in Fig.4.4c indicates where the ratio is 0.5. One can see that the relative difference between $q_{\mathrm{REF}}([q])$ and $[q_{\mathrm{REF}}(q)]$ is small over $40-70^{\circ}$N for all pseudoheight.

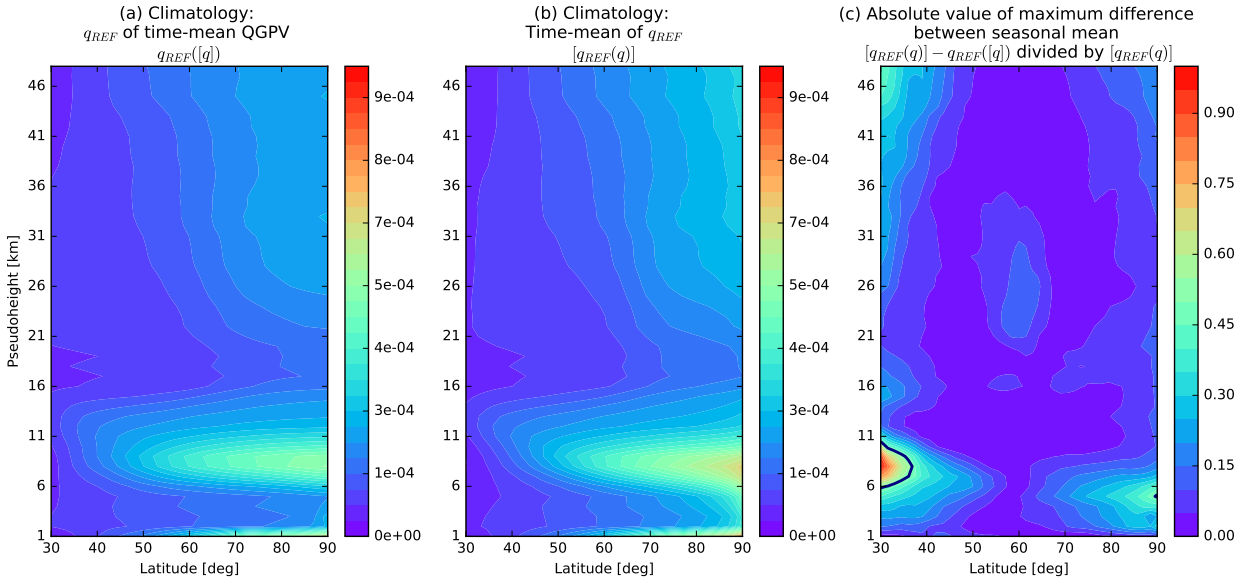

Figure 4.4: (a) Climatology of $q_{\mathrm{REF}}(q)$ computed from the DJF-mean q, i.e. $q_{\mathrm{REF}}([q])$, (b) climatology of DJF-mean $q_{\mathrm{REF}}(q)$, i.e. $[q_{\mathrm{REF}}(q)]$, and (c) the ratio of the maximum absolute difference (over 37 winters) between $q_{\mathrm{REF}}([q])$ and $[q_{\mathrm{REF}}(q)]$ to climatology of $[q_{\mathrm{REF}}(q)]$. The solid black line in Fig.(c) indicates where the ratio is 0.5.

Having the decomposition method justified above, the stationary-eddy component of LWA is estimated by applying (4.1) to the time mean of QGPV field, i.e., $\langle \tilde{A}^*([q]) \rangle$. Figure 4.5 shows the stationary-eddy component of $\tilde{A}^*$ on various isobaric surfaces. As a comparison,

I show in Fig.4.6 the DJF time-mean QGPV on the same isobaric surfaces. In the lower troposphere (e.g. Fig.4.6a), the distribution of QGPV is mostly dictated by the land-sea contrast. From the middle to upper troposphere (Figs. 4.6b and c), the stationary QGPV is dominated by a wave-2 component. In the stratosphere (Figs.4.6d and e), wave-1 component dominates. The peaks observed in Fig.4.3 are located at the latitudes where the stationary waves in the tropposphere are large. As observed in Figs. 4.5 and 4.6, the peaks at the east of the Mongolian Pleateau and Norwegian Sea arise largely from topography-induced meridional excursion of the QGPV contours from low levels.

The climatology of estimated stationary-eddy component of $\langle \tilde{A}^* \rangle$ is shown in Fig.4.7a. The climatology of transient-eddy component of LWA (Fig.4.7b) is estimated as the difference between the total (Fig.4.3) and the estimated stationary-eddy component of LWA (Fig.4.7a), i.e. $[\langle \tilde{A}^*(q) \rangle] - \langle \tilde{A}^*([q]) \rangle$. The longitudinal extent of the transient-eddy LWA over the North Pacific is consistent with other common metrics of storm tracks [e.g. Chang et al. (2002) Fig.2]. Over the Atlantic, where the barotropic jet is tilted northeastward, the LWA maxima for the transient eddies are found on both flanks of the jet, namely, over Quebec and western Europe (Fig.4.7b).

One may question whether a zonally symmetric reference state is suitable to analyze wave dynamics over the northeast-tilted Atlantic storm track. As a comparison, I show in Fig.4.8 the climatology of transient wave activity proposed by Plumb (1986) [his Eq. (2.20)], which is based on a zonally-varying basic state for small-amplitude waves. Our estimated transient LWA (Fig.4.7b) has a spatial structure consistent with Plumb's transient wave activity (Fig.4.8), which implies that the obtained LWA structure, especially the relative minimum over the Atlantic, is not a consequence of a particular choice of the reference state. It is rather an intrinsic property of wave activity that it is suppressed along the jet axis, as seen in the left panels of Fig.4.1. The above comparison also demonstrates the strength of the finite-amplitude LWA formalism: its magnitude is well-constrained by the wind field and much smoother, while the small-amplitude wave activity is plagued with spuriously large

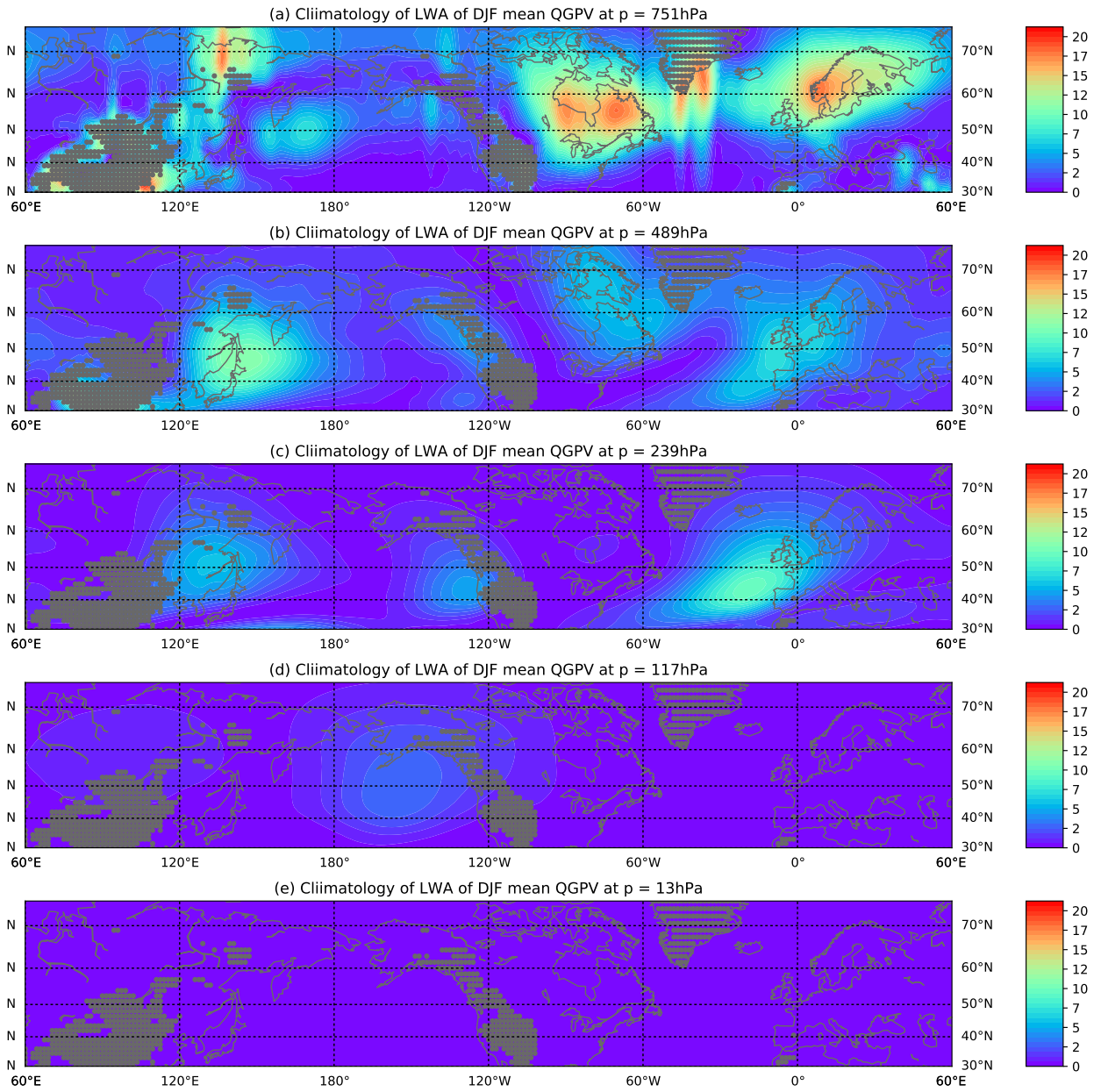

Figure 4.5: Stationary-eddy component of LWA computed from the DJF climatology of QGPV weighted by density ($\sim p/p_0 = e^{-z/H}$) on (a) $p = 751$ hPa (lower troposphere), (b) $p = 489$ hPa (mid-troposphere), (c) $p = 239$ hPa (tropopause), (d) $p = 117$ hPa (lower stratosphere), (e) $p = 13$ hPa (upper stratosphere).

values in regions where the gradient of time-mean QGPV vanishes.

Figures 4.9 and 4.10 show respectively the seasonal-mean wave activities during a positive North Atlantic Oscillation (NAO) phase (1994-1995 DJF) and a negative NAO phase (1984-1985 DJF). During the positive NAO phase, the Atlantic barotropic jet is tilted in the

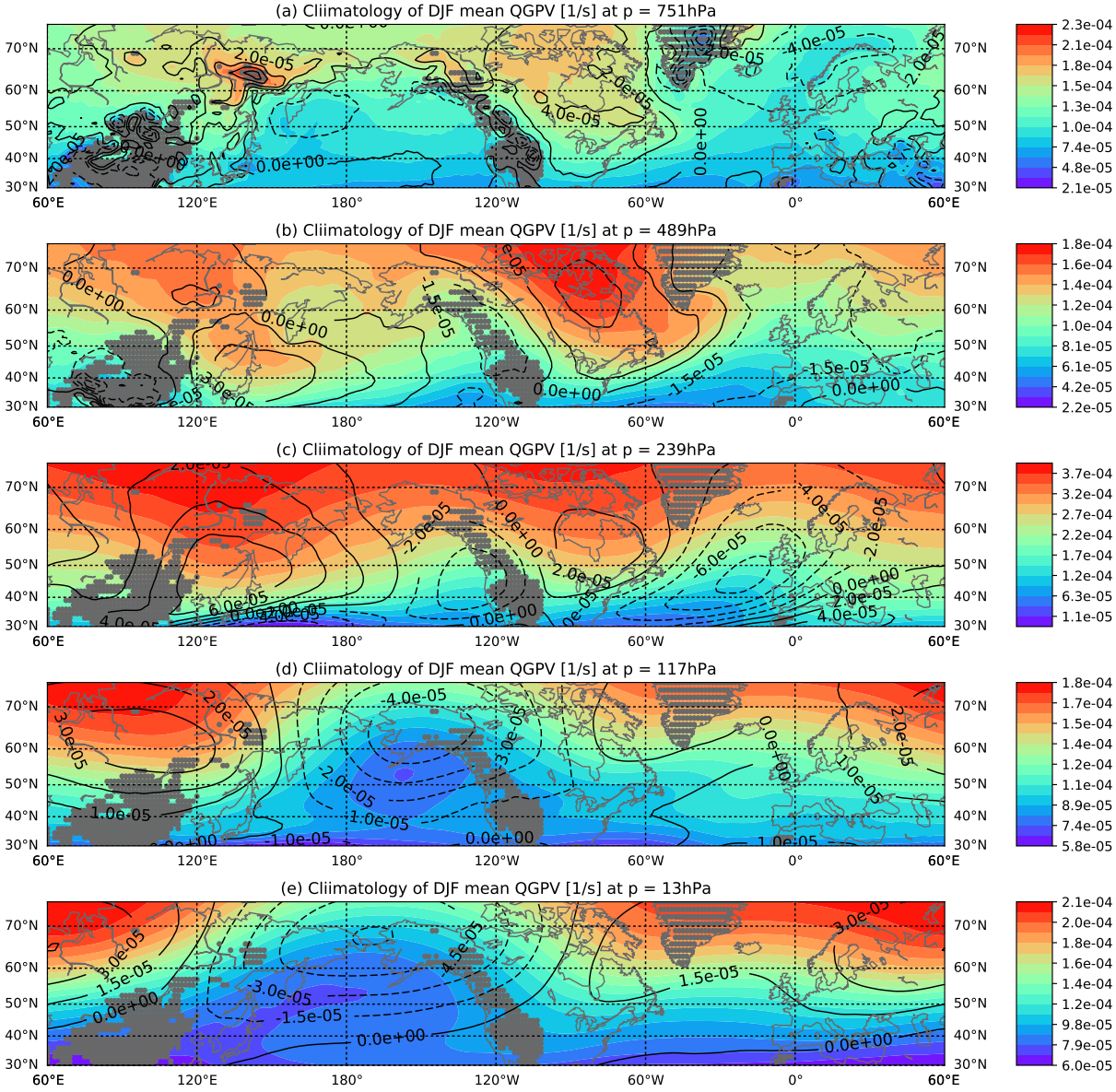

Figure 4.6: Climatology of DJF mean QGPV (shaded) and its deviation from zonal mean (contours) (s^{-1}) computed on the pressure levels corresponding to Fig.4.5.

NE-SW direction and extends further eastward compared to the negative phase. $\langle \tilde{A}^* \rangle \cos\phi$ over the Atlantic ocean is suppressed along the jet core (Fig.4.9a). During the negative NAO phase, the Atlantic jet is more zonal and extends less eastward. Similar tendency is also observed over the Pacific – the jet and transient-eddy component of LWA is disrupted by the stationary-eddy component in the eastern Pacific. In both years $\langle \tilde{A}^* \rangle \cos\phi$

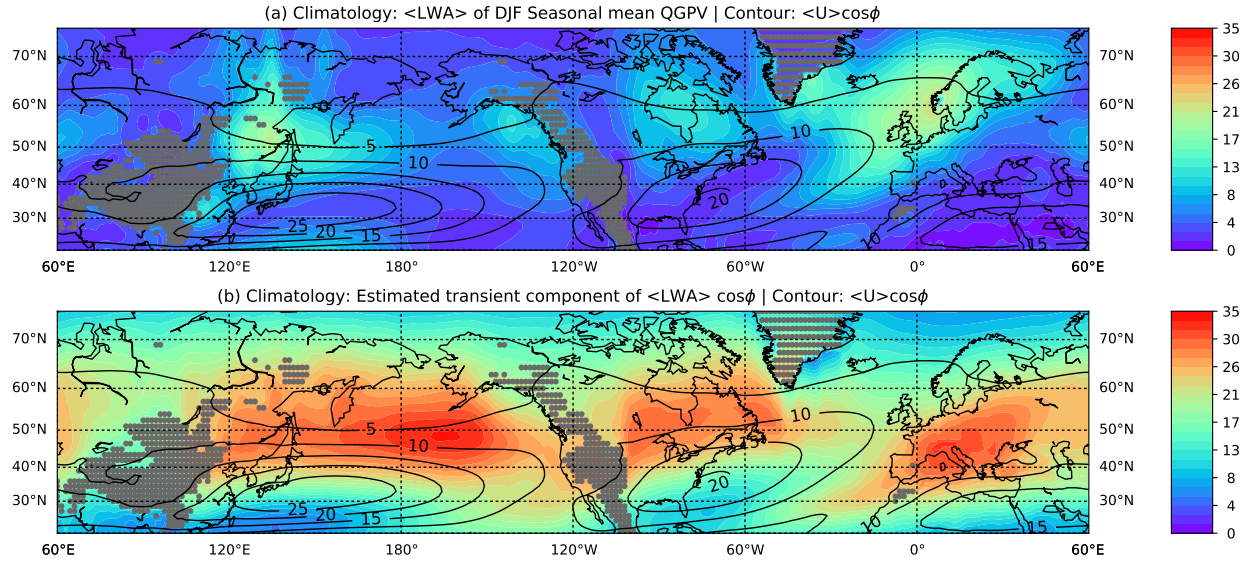

Figure 4.7: (Shaded) Seasonal (DJF) climatology of (a) estimated stationary-eddy component of $\langle \tilde{A}^* \rangle \cos\phi$ in DJF and (b) estimated ransient-eddy component of $\langle \tilde{A}^* \rangle \cos\phi$ taken as the difference between Fig.4.3 and (a). Both quantities have the unit ms^{-1}. Regions masked by the gray stipples, where the topography is higher than 1 km (i.e. $z_s > 1$ km), have been excluded from analysis.

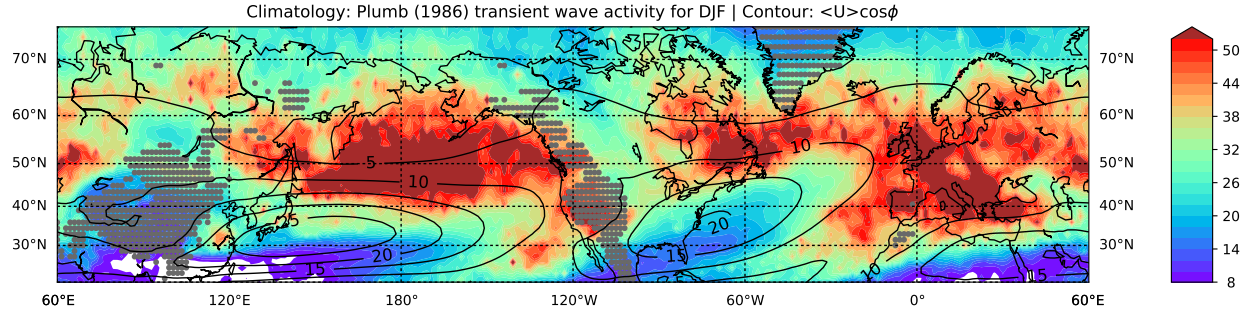

Figure 4.8: (Shaded) Seasonal (DJF) climatology of small-amplitude QG transient LWA computed with a zonally varying reference state based on Plumb (1986). It have the unit (ms^{-1}). Regions masked by the gray stipples, where the topography is higher than 1 km (i.e. $z_s > 1$ km), have been excluded from analysis.

is large at the diffluent region of the jet, but the peak of $\langle \tilde{A}^* \rangle \cos\phi$ over northern Europe is larger in magnitude in the negative NAO phase as the jet is not so extended into inland regions (Fig.4.10a). Figure 4.10b shows that this enhanced peak in LWA consists mostly of stationary-eddy component of $\langle \tilde{A}^* \rangle \cos\phi$. Transient-eddy component of $\langle \tilde{A}^* \rangle \cos\phi$ over northern Europe has similar values in both years, but the regions of high transient wave

activities are more separated meridionally to the flanks of the jet during the positive phase (Figs.4.9c and 4.10c). The above comparison shows that the total $\langle \tilde{A}^* \rangle \cos\phi$ is suppressed in high latitudes ($> 45°$N) of the Euro-Atlantic sector during the positive NAO phase. This is verified by the regression analysis in Section 4.4 below. LWA is suppressed at the jet core regardless of whether the jet is tilted or zonal. Small-amplitude transient wave activity by Plumb (1986) (Figs. 4.9d and 4.10d) has spatial structures consistent with that of $\langle \tilde{A}^* \rangle \cos\phi$ for these two seasons presented as well.

4.3.2 Climatology of wave activity budgets

As a first estimate of how the LWA budget is maintained, Fig.4.11 shows the climatology of the terms on the RHS of (4.4). The positive (poleward) low-level meridional heat flux (Fig.4.11c) is the major source of wave activity for both storm tracks. Over the North Pacific, its peaks are localized to the storm track entrance (from the Sea of Japan to the Kuroshio extension) and along the Alaska current. In contrast, large values of low-level poleward heat flux span over the majority of the Atlantic north of 40°N. Much of this signal is due to the quasi-stationary zonal asymmetry in the low-level potential temperature forced by the underlying SST distribution and the associated meridional flow. The spatial structure of the low-level meridional heat flux (Fig.4.11c) is similar to that of the estimated stationary component of $\langle \tilde{A}^* \rangle \cos\phi$ (Fig.4.7a).

Over the Atlantic, the low-level poleward heat flux is largely balanced by the zonal divergence of the LWA flux (blue in Fig.4.11a). Note that the peak values of LWA are displaced downstream of the peak low-level heat flux (Figs. 4.3 and 4.11c), indicating that LWA is moved away from the source region by the zonal flux into the downstream regions of convergence over Europe (red in Fig.4.11a). The meridional momentum flux convergence (blue in Fig.4.11b) also partially compensates the zonal flux convergence on the southern flank of the storm track, but the degree of this compensation is relatively small.

Over the Pacific, there is considerable spatial variation in the balance of RHS terms

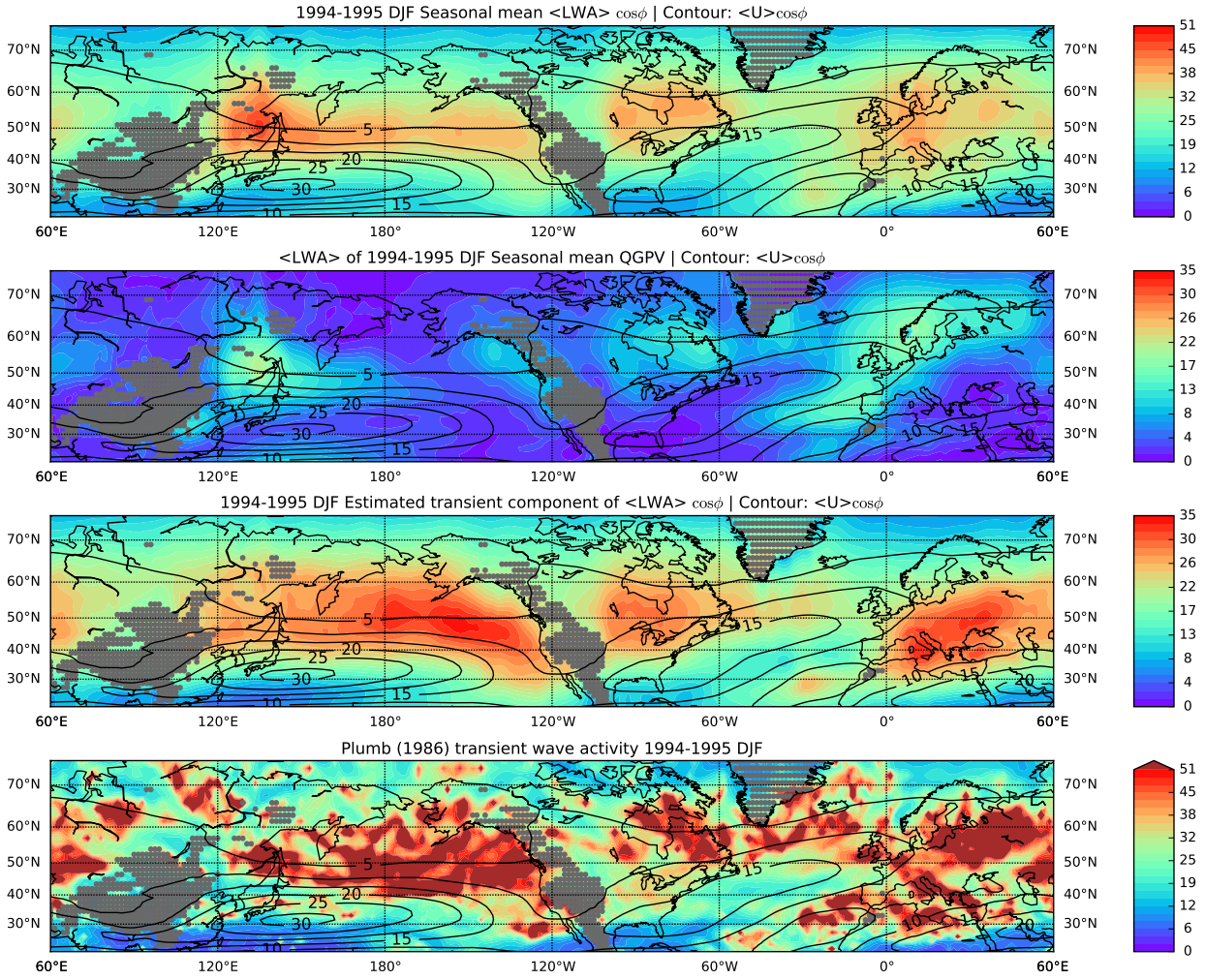

Figure 4.9: (Shaded) Seasonal (DJF) mean for a positive NAO year (1994-95 winter) of (a) $\langle \tilde{A}^* \rangle \cos\phi$, (b) estimated stationary-eddy component of $\langle \tilde{A}^* \rangle \cos\phi$ in DJF, (c) estimated transient-eddy component of $\langle \tilde{A}^* \rangle \cos\phi$ taken as the difference between (a) and (b), and (d) small-amplitude QG transient LWA computed with a zonally varying reference state based on Plumb (1986). In (d), a weak horizontal smoothing is applied to the seasonal-mean QGPV field before computing the horizontal gradient. Note that (b) and (c) share a colorscale of narrower range of values compared to that of (a) and (d). Values exceeding the color range in (d) are indicated in brown. Contours indicate the barotropic zonal wind $\langle u \rangle$. Both quantities have the unit [ms^{-1}]. Regions masked by the gray stipples, where the topography is higher than 1 km (i.e. $z_s > 1$ km), have been excluded from analysis.

of (4.4). In the source regions (e.g. the Sea of Japan and the Alaska current) a strong cancellation is still observed between the low-level poleward heat flux (Fig.4.11c) and the zonal divergence of the LWA flux (Fig.4.11a) as in the Atlantic. In the Central Pacific, where the low-level poleward heat flux is relatively weak, the zonal convergence of the LWA flux as

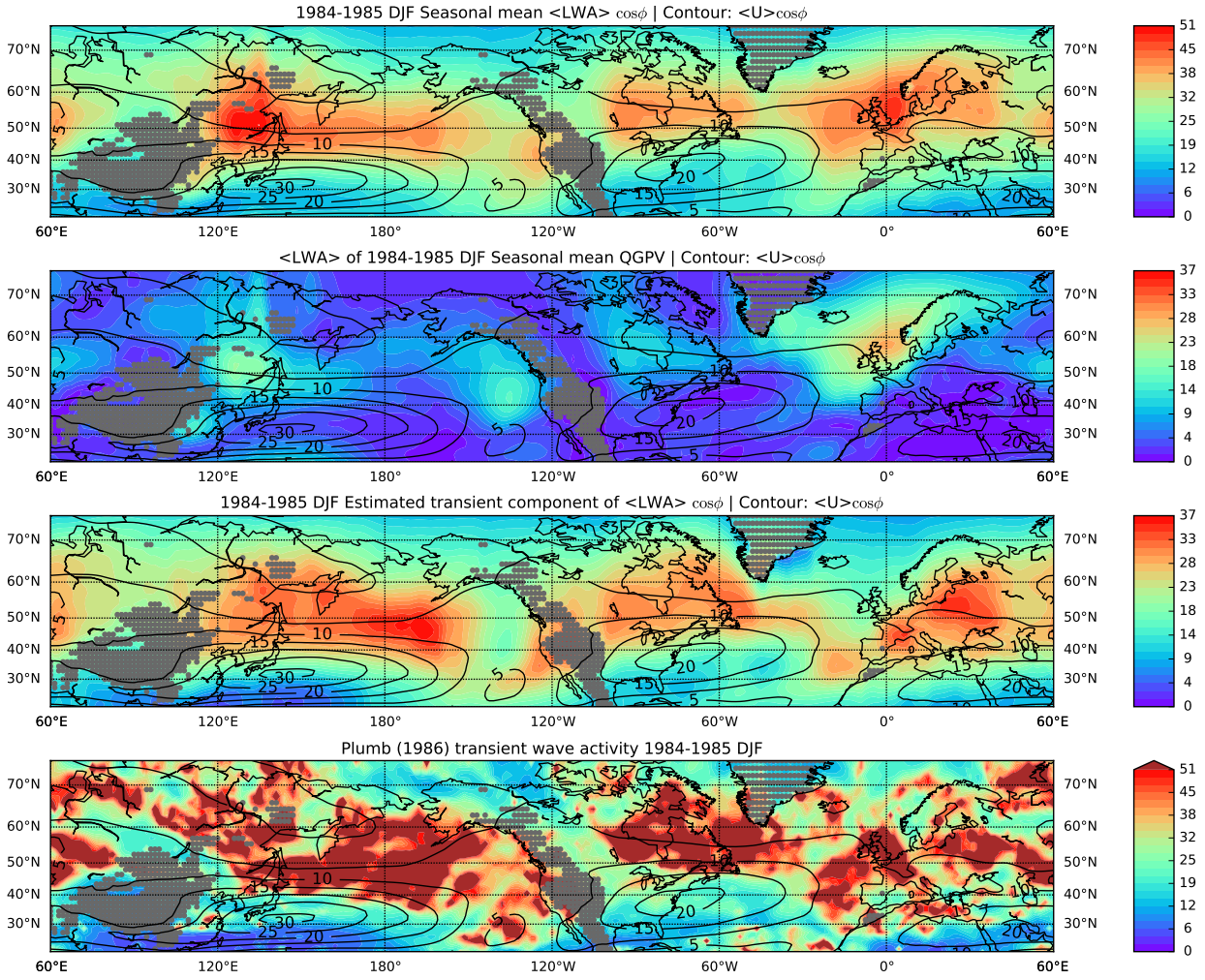

Figure 4.10: Same as Fig.4.9 but for a negative NAO year (1984-85 winter).

a gain, as well as the meridional convergence of the eddy momentum flux associated with the equatorward radiation of LWA (Fig.4.11b) and the negative residual (Fig.4.11d) as losses, all contribute to the LWA budget. The magnitude of the residual is quite significant that it is comparable to the horizontal LWA flux convergence (sum of Figs.4.11a and b). Assuming that the negative residual represents a linear damping of LWA, the ratio of the area averaged residual to that of the column LWA gives a mean damping timescale of $\sim$ 12 days. Since this is much shorter than the typical radiative damping timescale in the troposphere ($\sim$30 days), it may be related to Ekman damping or enstrophy dissipation (mixing) by wave breaking.

The residual (Fig.4.11d) over the continental regions is largely negative, which suggests

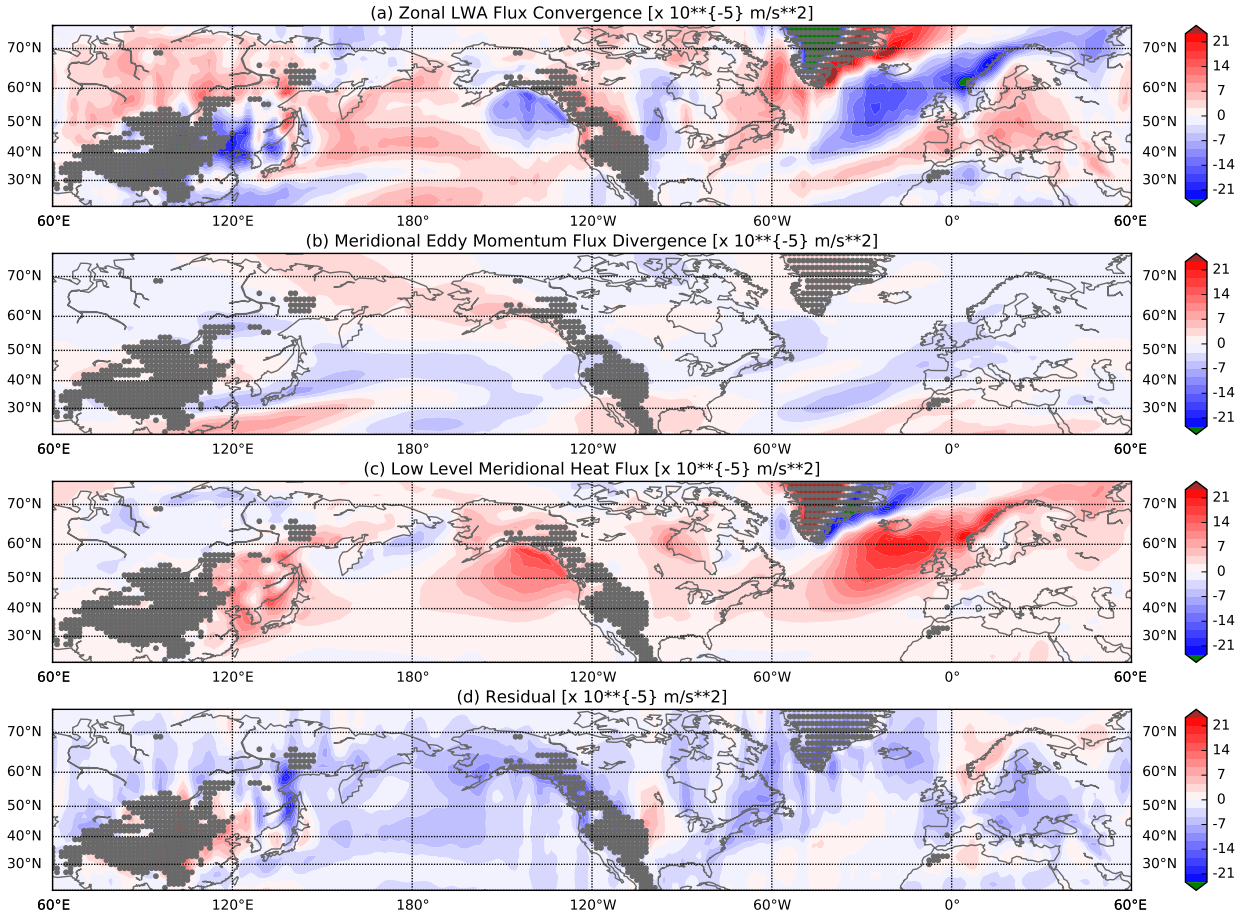

Figure 4.11: The December-February climatology (ERA-Interim 1979-2015) of vertical column-average (with cosine weighting) of (a) zonal LWA flux convergence, (b) meridional eddy momentum flux divergence, (c) low-level meridional heat flux, and (d) residual [see (4.4)]. The color scales for (a) to (d) are the same, with values greater than the maximum given by the color bar is displayed in brown, while that less than the minimum given by the color bar is displayed in green.

that friction over land surfaces promotes the demise of LWA. Exceptions are found on the lee side of mountains (e.g. the Mongolian Plateau and the Rockies). Over the oceans, the residual is generally weakly negative. However, there are pockets of weakly positive values over the Atlantic Ocean and the Norwegian Sea, hinting that the underlying warm ocean is providing appreciable diabatic sources of LWA (primarily through latent heat of condensation) that override the effect of surface damping. I suspect that this partial cancellation causes the average residual less negative over the Atlantic than over the Pacific.

4.3.3 Synoptic to intraseasonal variability

Much of the weather-related LWA variability occurs over synoptic to intraseasonal timescales, which are filtered out in the seasonal mean in the foregoing analysis. To delineate the wave activity budget on these timescales, I compute the cospectra of LWA tendency [the LHS of (4.3)] with each term on the RHS and compare it with the power spectrum of LWA tendency (Fig.4.12a, b). Note that the sum of the cospectra resembles the power spectrum (black line). The solid lines indicate the budget over a regular box domain including both land and ocean grids, while the shading indicates the budget change if the domain shrinks to oceanic regions only (Appendix G). Comparing Figs.4.12a and 4.12b, one sees that the variance in the Atlantic is more than twice larger than that in the Pacific but the spectral shapes are largely similar between the two regions. The power spectrum of LWA tendency maximizes around 0.15-0.25 cpd (4-7 days); over half of that is explained by the in-phase components of the zonal LWA flux convergence (blue) with a similar spectral shape. Cospectra with the meridional eddy momentum flux divergence (cyan) are an order of magnitude smaller than those with the zonal flux convergence (blue) for both regions, indicating that the LWA budget is dominated by the zonal passage of synoptic weather systems in and out of the regions. Even though the low-level poleward heat flux dominates the LWA budget in the seasonal mean (Fig.4.11), it plays only a minor role in the LWA tendency except at low frequencies (< 0.05 cpd, red). The heat flux cospectrum over the Atlantic is broader than that over the Pacific, which is more right-shewed. Somewhat surprisingly, the residual (green) contributes to the LWA tendency much more than the heat flux over synoptic timescales. Its contribution is comparable to the zonal advective flux convergence (blue) over the land-oceanic domain, while a bit smaller over oceanic domain. This suggests that there is significant diabatic forcing of wave activity in both regions.

Given that the meridional eddy momentum flux divergence accounts for only a small fraction of LWA tendency, to what extent do LWA and the zonal wind covary through this term [(4.2) and (4.3)]? Figures 4.13a and 4.13b compare the cospectra of the meridional eddy

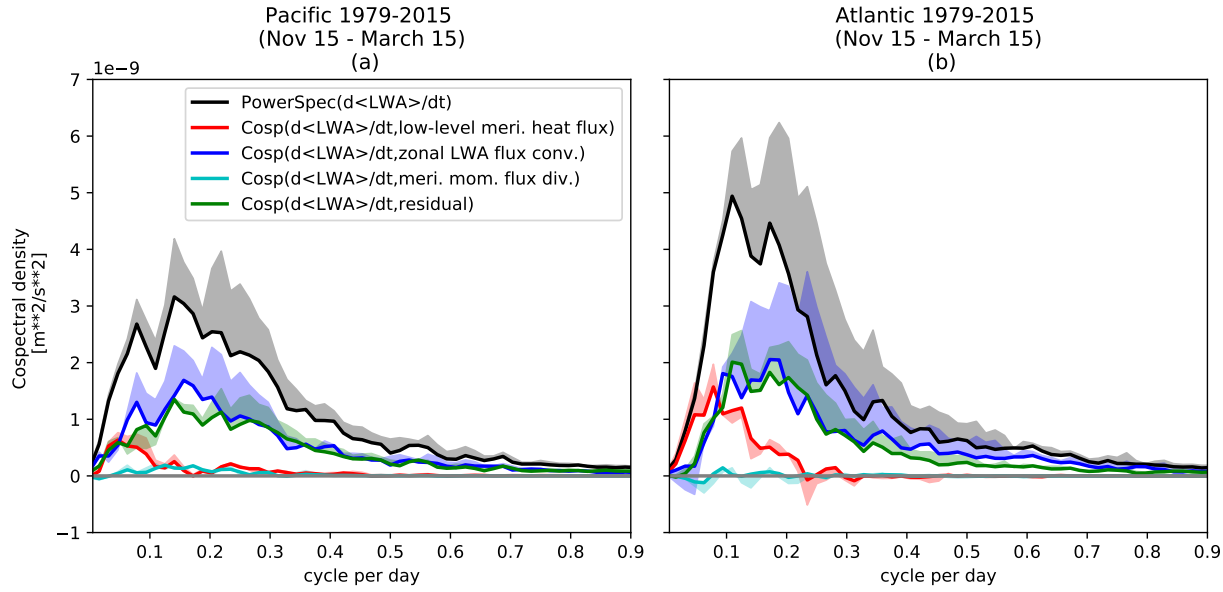

Figure 4.12: Comparison between power spectra of LWA tendency (black) with the cospectra between LWA tendency and the four terms on the RHS of (4.3) for (a) North Pacific and (b) North Atlantic. See legend for the corresponding line colors. The power spectra/cospectra analysis was done with the Hann window from November 15 to March 15 every year, and then it was averaged over the years in 1979-2015. The shading of the same color indicates the change in results if the spatial averaging domain is shrunk to oceans only. (See Appendix G.)

momentum flux convergence with the LWA tendency (blue), with the zonal wind tendency (green), the cospectra of LWA tendency and the zonal wind deceleration (red), and the power spectrum of the zonal wind tendency (black) for the two storm track regions. The power spectrum of the zonal wind tendency peaks at around 0.05 cpd in both regions. Over the Pacific, the close alignment of blue, green, and black curves on synoptic timescales indicates that the convergence of the meridional momentum flux accomplishes barotropic conversion between $\langle \tilde{A}^* \rangle$ and $\langle u \rangle$ as suggested by (4.2) and (4.3), and it accounts for most of the zonal wind tendency. This is not the case with the Atlantic, where the meridional eddy momentum flux divergence has a negative contribution to the LWA tendency and it accounts for much less fraction of zonal wind tendency. Interestingly, the cospectra between the LWA tendency and the zonal wind deceleration (red) are *positive* throughout the frequency domain shown and deviate significantly from the other three curves at higher frequencies in both regions,

particularly when the domain includes only oceanic regions: that is, the negative covariation of LWA and zonal wind is robust regardless of the contribution from the meridional eddy momentum flux divergence. This implies that there are other budget terms in (4.2) and (4.3) contributing to such positive covariation.

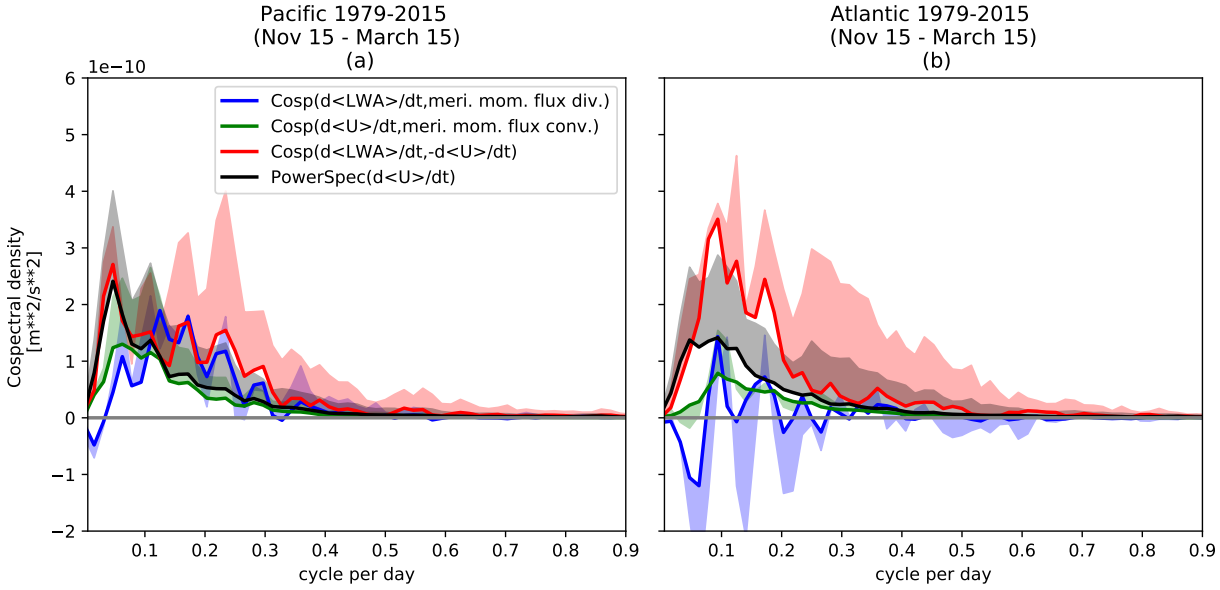

Figure 4.13: Comparison between power spectra of zonal wind tendency (black) with Cosp(LWA tendency, meridional momentum flux divergence) (blue), Cosp(zonal wind tendency, meridional momentum flux convergence) (red) and Cosp(LWA tendency, zonal wind tendency) (green) for (a) North Pacific and (b) North Atlantic. The power spectra/cospectra analysis was done with the Hann window from November 15 to March 15 every year, and then it was averaged over the years in 1979-2015. The shading of the same color indicates the change in results if the spatial averaging domain is shrinking to oceans only. (See Appendix G.)

Recall that Fig.4.2 shows the DJF climatology of covariance of the column-averaged LWA $\langle \tilde{A}^* \rangle \cos\phi$ and the column-averaged zonal wind $\langle u \rangle \cos\phi$ (color), together with the seasonal-mean column averaged zonal wind $[\langle u \rangle] \cos\phi$ (contours). Consistent with the red curves in Figs. 4.13a and b, the covariance is largely negative. Furthermore, its magnitude is strongest in the jet exit (diffluent) regions where the transient-eddy LWA maximizes (Fig.4.7b). The localization together with the dominance of the zonal LWA flux convergence in the cospectra of the LWA tendency suggests that the regional interaction between the eastward propagating

synoptic eddies and the zonal wind as the former enter the diffluent regions of the jet plays a significant role in the synoptic to intraseasonal variability in both LWA and the zonal wind.

4.4 Regression of LWA with different modes of teleconnections (NAO, AO and PNA indices)

To investigate the relationship between LWA and the more traditional indices of climate variability, I regress daily mean $\langle \tilde{A}^* \rangle$ on the daily values of indices retrieved from the NOAA Climate Prediction Center (CPC) database (NOAA, 2016). The following figures show respectively the regression patterns on the North Atlantic Oscillation (NAO) index (Hurrell et al., 1995) (Fig.4.14), Arctic Oscillation (AO) index (Thompson and Wallace, 1998) (Fig.4.15) and the Pacific/North-Atlantic (PNA) index (Wallace and Gutzler, 1981) (Fig.4.16). In Fig.4.14, the dipole signature of NAO emerges robustly over the Atlantic with its position slightly displaced equatorward compared to the leading pattern of NAO in geopotential height. As the Atlantic jet is split [with cores located at $\sim 15°$N and $\sim 50°$N, see for example Ambaum et al. (2001), Fig.7], wave activity is suppressed at the jet cores but enhanced between the split jets. Therefore, a positive NAO correlates with an increased wave activity southward ($\phi \leq 40°$) of the high-latitude jet core and decrease in wave activity at the jet core. Empirical orthogonal function (EOF) analysis of regional $\langle \tilde{A}^* \rangle$ reveals that the first two leading patterns of variance in $\langle \tilde{A}^* \rangle$, which explain in total 23% and 32% of variance over the Pacific and the Atlantic respectively, are associated with the zonal propagation of waves (not shown). The modes associated with meridional radiation of wave activity (i.e. a meridional dipole pattern) do not produce large variance. This explains the small correlation resulted from the regression (contours in Fig.4.14). Similarly robust regression patterns but small correlation coefficients are obtained from regression analyses done on the AO (Fig.4.15) and PNA (Fig.4.16) indices. The results indicate that these global climate patterns do exist in the LWA field, but their signals are weak compared to those of the

transient weather systems.

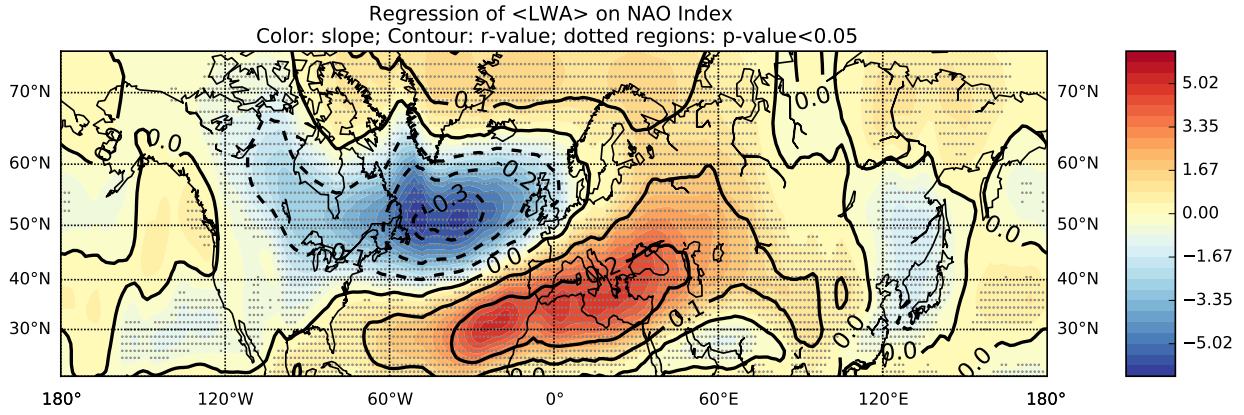

Figure 4.14: Regression of daily mean $\langle \tilde{A}^* \rangle$ on daily NAO index. Color indicates the regression slope. The contours indicate the r-value ranging from -0.3 to 0.3 at intervals of 0.1. The stippled regions are where the p-value < 0.05 such that the null hypothesis that $\langle \tilde{A}^* \rangle$ not being related to NAO index is rejected with a 95% confidence.

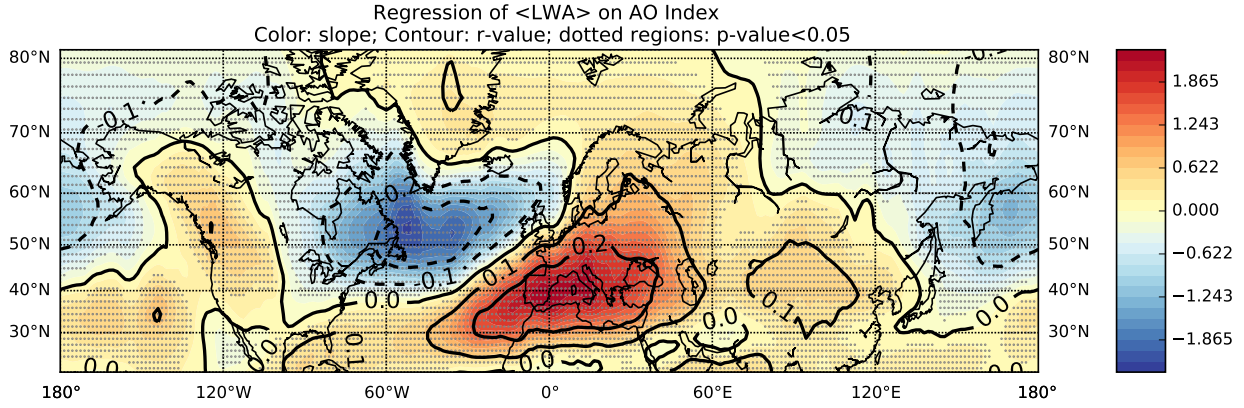

Figure 4.15: Same as 4.14 but for AO index.

4.5 Summary

In the literature, there has hitherto been no formal attempt to close the *local* angular momentum-wave activity budget for the midlatitude atmosphere. I have applied the column budget of finite-amplitude LWA, a density of angular pseudomomentum, to the winter storm tracks over the North Pacific and the North Atlantic using meteorological data. The

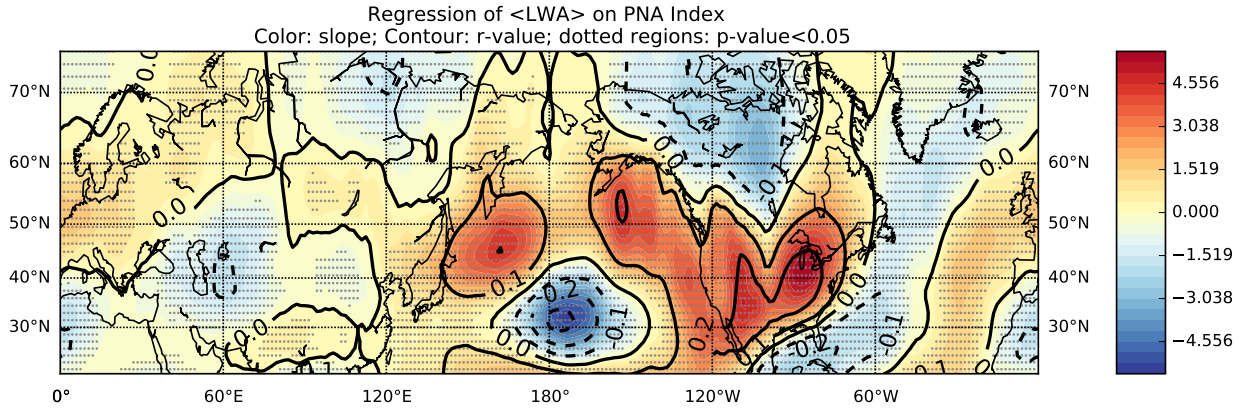

Figure 4.16: Same as 4.14 but for PNA index.

regional budget of LWA is simpler than the budget of small-amplitude wave activity. The latter is often hard to close without large nonlinear terms, and particularly problematic where the time-mean PV gradient vanishes. As a result, only the wave activity fluxes, but not the wave activity itself, have been used for diagnosis in this context (Plumb, 1985; Takaya and Nakamura, 2001; Chang, 2001).

Complementary to EKE, LWA maximizes where waves attain greatest cross-stream displacement of QGPV and weak zonal wind speeds (Fig.4.1). I have proposed an approximate partitioning of LWA into transient and stationary eddy contributions by decomposing the QGPV fields used in (4.1). The estimated transient-eddy LWA climatology has spatial distribution consistent with that of Plumb's small-amplitude transient wave activity (Plumb, 1986) with zonally-asymmetric basic state.

The climatology of seasonal-mean LWA flux convergence gives a first estimate of how the LWA budget is maintained. In both storm track regions, the low-level poleward heat flux is a major source of LWA. The balancing mechanisms are nevertheless different. Over the Atlantic, the loss is primarily through the zonal divergence. Over the Pacific, the LWA input by the heat flux is localized to the western and northeastern ends of the ocean basin, where it is largely balanced by the zonal LWA flux divergence. However, over the Central Pacific, the flux convergence is largely balanced by the loss through the residual (damping).

On synoptic timescales, the area-averaged LWA tendency is closely associated with the

convergence of the zonal LWA flux in both regions, corresponding to the transient passage of weather systems. However, the residual term representing the net diabatic source has a comparable magnitude whereas the low-level poleward heat flux plays a relatively small role. Whilst LWA and the zonal wind covary negatively at all scales, the barotropic conversion of zonal momentum plays only a limited role for this and is only significant over the Pacific.

Since the net non-conservative sources and sinks of LWA are only inferred from the residual of the budget in this study, more direct assessment of the diabatic sources of LWA in relation to the storm track maintenance (Hoskins and Valdes, 1990) requires the aid of general circulation models. Nevertheless, this work provides a promising framework to delineate tendency of longitudinally localized wave activity with arbitrary amplitudes, which is potentially useful for comparing wave responses in models in climate change scenarios.

CHAPTER 5

CONCLUSION AND FUTURE DIRECTIONS

5.1 Summary

In this thesis, I have laid out a diagnostic formalism suitable for longitudinally localized, finite-amplitude wave events such as Rossby wave breaking and atmospheric blocking. These events are often associated with extreme and persistent weather anomalies in the midlatitudes, but most existing detection methods are empirical and sometimes produce contradicting results. Furthermore, most detection metrics are not derived from first principles of fluid dynamics. Therefore, they do not provide mechanistic understanding of finite-amplitude wave events. On the other hand, application of the wave-mean flow interaction theory to finite-amplitude wave events through meteorological data has been limited – former theories were constructed based on the assumption of small-amplitude waves, with the exception of finite-amplitude wave theories by McIntyre and collaborators (Andrews and McIntyre, 1978; Killworth and McIntyre, 1985) which have issues on practicality discussed in Chapter 1 and 3.

The finite-amplitude Rossby wave activity (FAWA) formalism developed by Nakamura and collaborators (Nakamura and Zhu, 2010; Nakamura and Solomon, 2010, 2011; Solomon and Nakamura, 2012) is amenable to Rossby waves and QG eddies of arbitrary amplitude and possesses a simple, closed budget of fluxes. It is however limited to the zonal-mean statistics and thus unable to distinguish longitudinally isolated events.

This thesis generalizes FAWA to a function of longitude, namely, the local wave activity (LWA), which measures a longitude-by-longitude contribution to FAWA. The regional budget of LWA for the boreal winter may be closed using data, which was not achievable with previously developed local wave activity flux formalisms (Andrews and McIntyre, 1976; Plumb, 1985, 1986; Takaya and Nakamura, 2001) based on the small-amplitude assumptions. LWA provides a promising diagnostic framework for studying *local* finite-amplitude phenomena in

meteorological data and climate model outputs.

Chapter 2 of the thesis was a recapitulation of the merits of the FAWA theory, and demonstrated for the first time how FAWA budget can be closed with gridded data. I demonstrated with an idealized simulation of barotropic decay in a shear flow (Held and Phillipps, 1987) how FAWA can capture breaking waves when the linear wave activity is ill-defined. The experiment also revealed the inadequacy of critical line theory (for linear waves) in predicting the latitude of wave breaking for finite-amplitude waves. Most importantly, the FAWA budget in the model output was shown to be closed with the E-P flux (advection) and the diffusive flux (irreversible mixing, in terms of effective diffusivity) of vorticity.

In Chapter 3, I generalized FAWA to LWA and tested its utility for diagnosing longitudinally localized wave events in both a barotropic model and meteorological data. LWA is superior to any small-amplitude wave metric in that the conservative part of its *local* budget can be closed with fewer, simpler flux terms. Compared to an existing finite-amplitude wave formalism (Killworth and McIntyre, 1985; Haynes, 1988), LWA was shown to be more easily interpreted and satisfy more closely the approximate non-acceleration relation (albeit within the WKB approximation). Application to the Atlantic blocking of October 2012 revealed a stark ability of LWA in isolating the center of blocking action. The analysis also captured a very robust anti-phase covariation between LWA and the local zonal flow, consistent with the non-acceleration relation.

Chapter 4 developed the methodology to implement the budget analysis for the *barotropic components* of LWA and its fluxes with reanalysis data. The regional LWA budget analysis over the North Pacific and the North Atlantic revealed the spatio-temporal structure and the relative importance of the flux terms. This is the very first study to associate the variability of wave activity with the *local* wave activity budget based on meteorological data. [Previous works by Wang and Nakamura (2015, 2016) delineate the *zonal mean* FAWA budget in the Southern Hemisphere.] The relative contributions of the flux terms to the synoptic variability of LWA along the storm track regions were found to be (in the order of importance): (1)

zonal LWA flux convergence, (2) non-conservative source/sink (diabatic heating), (3) low-level meridional heat flux, and (4) meridional momentum flux divergence. This represents a significant departure from the zonal-mean picture, in which the contribution from the zonal LWA flux vanishes. It highlights the importance of zonal inhomogeneity in the flow and eddy fluxes for large wave events that are longitudinally localized. I will expound on this idea further in the next section.

There are some limitations to the LWA diagnostic mostly inherent to the QG assumption that this work has not attempted to overcome. They include: (1) the breakdown of QG assumption near the equator (e.g., horizontal wind that advects PV is no longer area-preserving), (2) errors in evaluating advecting wind (I used full horizontal winds instead of their geostrophic components), (3) a flat lower boundary assumed (which, I attempted to remedy with modified potential temperature at the surface). There is also a resolution dependence of the calculation method. As shown in Chapter 2, the effect of numerical errors in box-counting algorithm becomes significant when the wave amplitude is small. In fact, the computed budget improves as wave amplitude increases. For waves with a very small amplitude, a method based on the linear wave activity might be more accurate. Finally, whereas the LWA analysis is fully amenable to meteorological data, the full budget analysis does entail more complicated computation than the traditional Eulerian mean formalisms. This includes computation of equivalent latitude and inversion algorithms for the reference state. These are the factors that one has to take into account when choosing a diagnostic framework.

5.2 Future Directions

5.2.1 Onset of blocking and the regional wave-zonal flow interaction

Robust features of the boreal winter storm tracks that emerged in the analysis of Chapter 4 include: (1) zonal LWA flux convergence plays a leading role in the synoptic- to intraseasonal

variation of barotropic LWA (Fig.4.12); (2) transient-eddy LWA tends to maximize in the jet exit (diffluent) regions of both storm tracks (Fig.4.7); (3) in the same regions the covariance of LWA and zonal flow is most strongly negative (Fig.4.2). This leads to a hypothesis that the large eddy activity in the jet exit regions is governed by the variation of the zonal LWA flux associated with a regional wave-zonal flow interaction. In particular, a positive feedback may exist between (1) the deceleration of the zonal flow with amplifying LWA through non-acceleration relation and (2) stagnation and accumulation of LWA in a slowed advecting zonal flow.

Recently, Nakamura and Huang (2017) (NH17) explored the possibility of such positive feedback playing a role in the onset of blocking, using a highly idealized QG equivalent barotropic model of a PV front. They demonstrated with a 1D quasi-linear theory that a train of transient waves continuously forced in the upstream and traveling along a zonally varying jet can develop a LWA shock (discontinuity) once the local zonal flow is decelerated (but not reversed) beyond a threshold value. The threshold behavior arises in the model of NH17 because the zonal LWA flux is proportional to $[U(X) - \tilde{A}^*]\tilde{A}^*$, where $U(X)$ is the initial zonal flow speed along the jet axis. The nonlinear term represents the effect of (local) wave-zonal flow interaction. This flux maximizes at $\tilde{A}^* = U(X)/2$. Once $\tilde{A}^*$ grows beyond this value and increases downstream, the zonal gradient in $\tilde{A}^*$ grows without bound, creating a shock. Further numerical tests with a 2D model showed that once this threshold is reached, the transient waves roll up a quasi-stationary block, provided that there is sufficient cross-stream layer thickness variation (which there is in the extratropical tropopause region) (NH17). These suggest that the onset of blocking can indeed be understood in terms of a runaway accumulation of LWA caused by local wave-zonal flow interaction.

Preliminary analysis on reanalysis data shows promising evidence that such interaction between local zonal flow and LWA exists. The left column of Fig.5.1 samples 5-day average zonal LWA flux $\langle F_A \rangle$ in (4.3) (blue) and the sum of the first and last terms of F_A in (D.11) (orange) at 15°W, 45°N (top) and 147°W, 42°N (bottom) as a function of 5-day average

$\langle \tilde{A}^* \rangle$ over 38 DJF seasons. These locations are close to the center of blue regions in Fig.4.2, i.e., where the anti-covariation between the zonal flow and LWA is strongest (marked by stars in Fig.5.2). The orange diamonds roughly cluster around a line. The slope of the line is roughly equal to the effective zonal group velocity of the waves passing over the respective locations. By including the second (i.e. nonlinear) flux in (D.11), the total zonal LWA flux significantly deviates from the orange diamonds. Although there is significant scatter, the majority of the blue diamonds lie below the orange ones, particularly at large LWA.

The right panels of Fig.5.1 simplify the corresponding left panels by curve fits and quartile plots. The orange lines are the least square fits to the orange diamonds in the left panels. The bars indicate the maximum, minimum, and the upper and lower quartiles of F_A for each 10 ms^{-1} LWA bin. (The last bin in both panels does not contain enough samples for the quartile analysis.) The blue curves are the χ^2-fit of quadratic curves to the blue diamonds. Despite the large uncertainties, it is fair to say that the zonal LWA flux tends to maximize at *intermediate values of LWA* (40-50 ms^{-1}). A few samples with a negative (westward) LWA flux occur at large LWA values. In the left panels of Fig.5.1, 19 such events [$\langle \tilde{A}^* \rangle \cos\phi >$ 60 ms^{-1}, $\langle F_A \rangle < 0$] are identified for the Atlantic and 7 for the Pacific, all marked in red diamonds.

There is a close correspondence between Fig.5.1 and the so-called fundamental diagram of traffic flow in transportation engineering, which plots traffic flux as a function of traffic density. It is well known that, for a major highway, local traffic flux maximizes at an intermediate value of traffic density. Once the traffic density exceeds this threshold, a sudden traffic jam occurs (Lighthill and Whitham, 1955; Richards, 1956). By analogy, a LWA larger than the threshold with a small (or even negative) zonal LWA flux would be like an atmospheric 'traffic jam' or a blocking event.

Figure 5.2 shows the DJF climatology and the composites of the events identified in Fig.5.1 (red diamonds) for 500 hPa geopotential height (contours) and $\langle \tilde{A}^* \rangle \cos\phi$. The climatology shows a slow undulation of the jet stream by a wavenumber-2 stationary wave. The

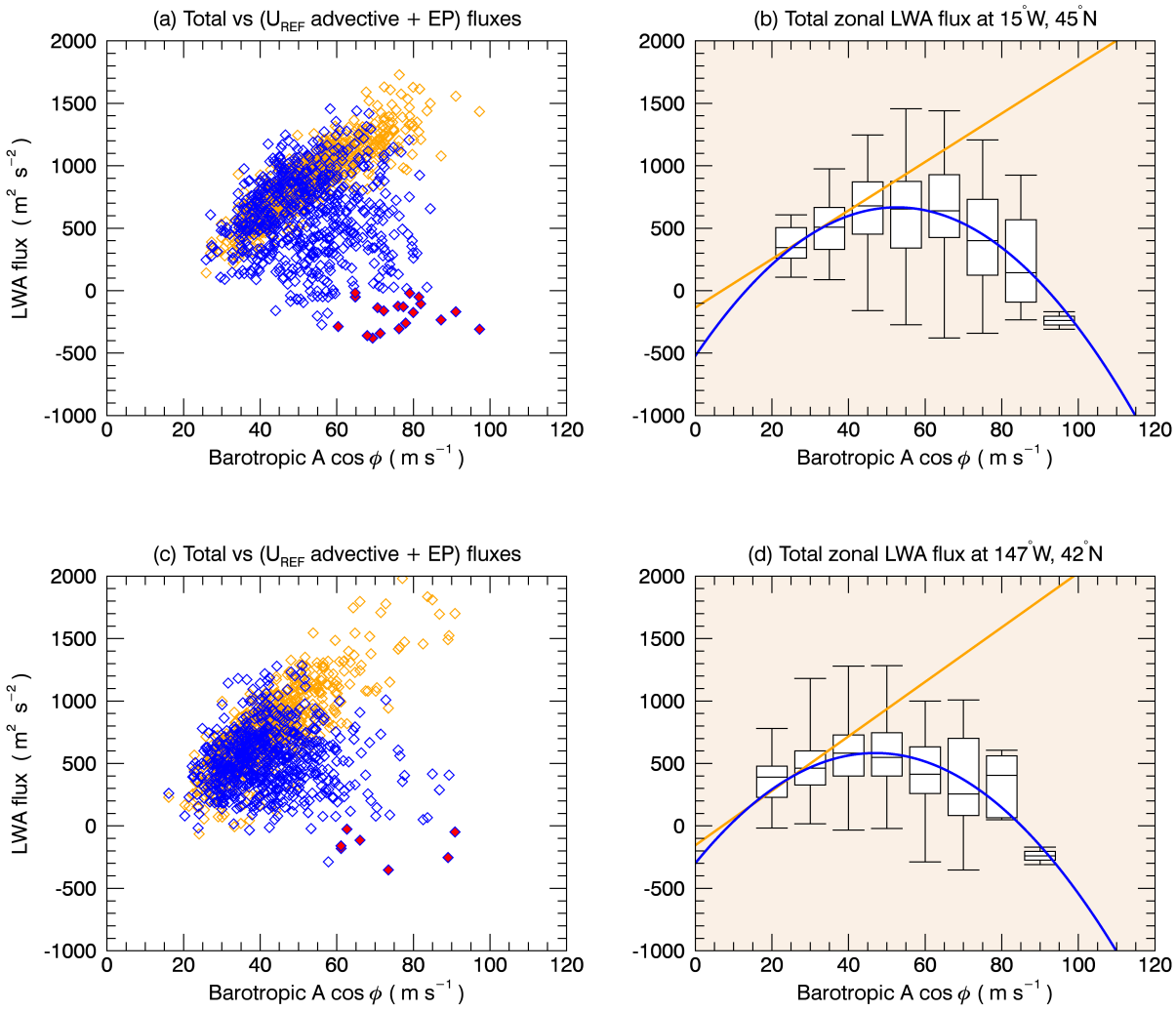

Figure 5.1: Five-day average column-mean zonal LWA fluxes $\langle F_A \rangle$ (ordinate) versus 5-day average column-mean wave activity $\langle \tilde{A}^* \rangle \cos\phi$ (abscissa) for DJF 1979-2016. Source: ECMWF ERA Interim. Top: 15°W, 45°N. Bottom: 147°W, 42°N. (a), (c): Blue: total zonal flux. Orange: zonal advective flux by u_{REF} plus the zonal component of E-P flux [see (E.11)]. Each diamond represents one 5-day period. Red: periods in which the total flux is negative and $\langle \tilde{A}^* \rangle \cos\phi > 60$ m s^{-1}. (b), (d): curve fits and quartile plots to $\langle F_A \rangle$ in (a) and (c). See text for details.

composites of the strongest wave events at respective locations capture markedly enhanced ridges and displaced jets, as well as large values of LWA – a clear signature of blocking. The next step in the investigation will be to study the evolution of those events and identify the trigger points of the runaway accumulation that distinguish these events from normal flow scenarios.

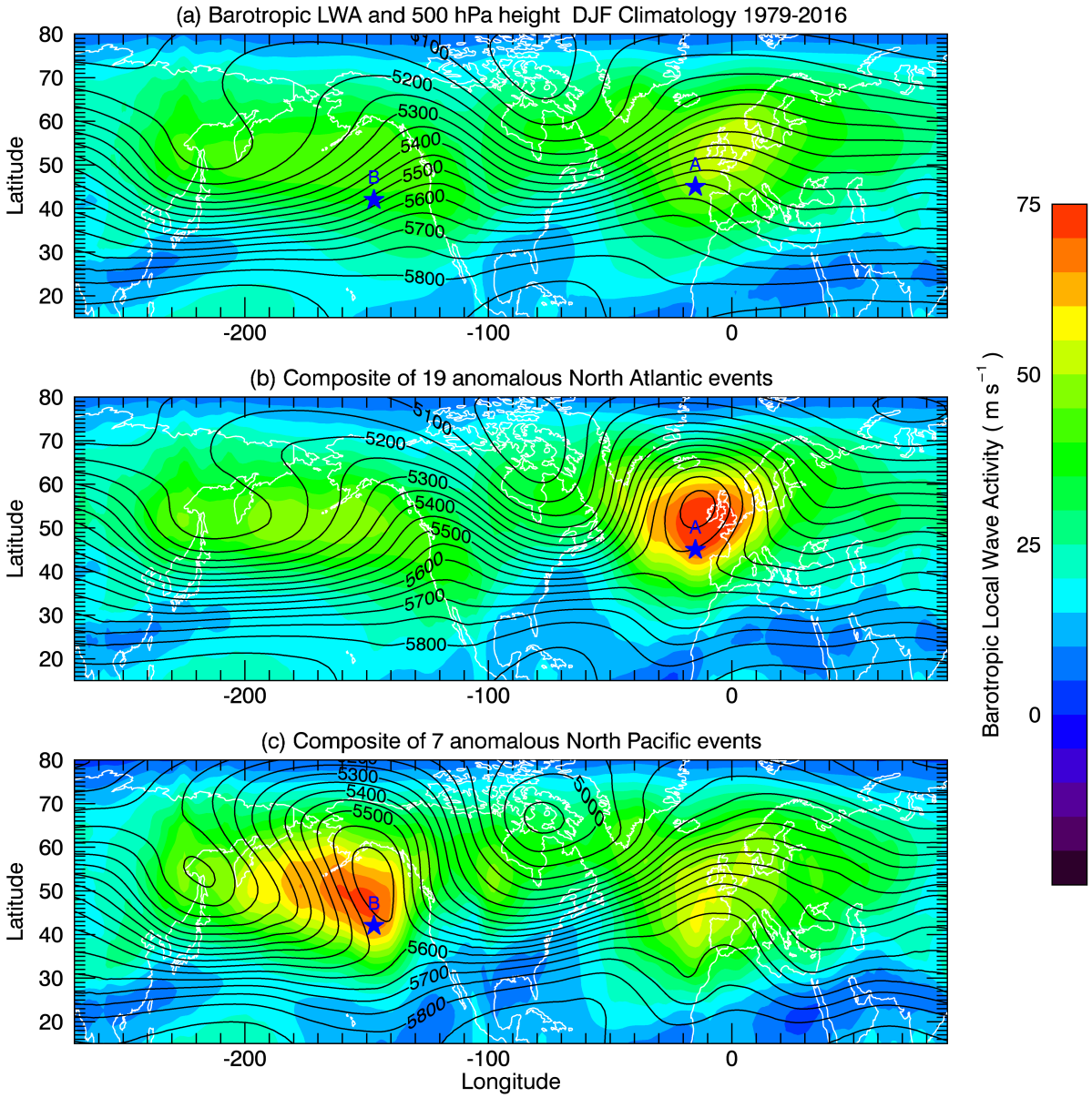

Figure 5.2: (a) DJF climatology (1979-2016) of 500 hPa geopotential height (Z500) (contours) and $\langle \tilde{A}^* \rangle \cos\phi$ (color). (b) Composite of Z500 and $\langle \tilde{A}^* \rangle \cos\phi$ for 19 5-day events over the North Atlantic at 15°W, 45°N (indicated by star 'A') for which $\langle \tilde{A}^* \rangle \cos\phi > 60$ m s^{-1} and $\langle F_A \rangle < 0$. (c) same as (b) but for seven 5-day events over the North Pacific at 147°W, 42°N (indicated by star 'B').

5.2.2 Budget analysis in idealized models

One of the surprises in the results of Chapter 4 was that the residual term in the budget plays a significant contribution as a LWA source over the synoptic timescale. Its magni-

tude suggests that the signal is likely real, that is, it quantifies the role of non-conservative processes rather than analysis errors. Therefore, the LWA budget is useful for estimating the importance of non-conservative processes, but the diagnostic does not reveal what these processes are. To fully understand the forcing mechanism of LWA, one needs to conduct careful comparisons of general circulation model (GCM) simulations.

An obvious candidate for the non-conservative sources of LWA is latent heating associated with moist convection. The first step to test this hypothesis would be to implement the same analysis on outputs from GCM simulation that realistically produces the Pacific and the Atlantic storm tracks, in which the diabatic terms are also output. I will compare the residual obtained using the wave activity with the diabatic heating term to see if the latent heat component over the Atlantic is larger than that over the Pacific.

Another important question is the decadal trend in the LWA budget. Figure 5.3 shows the yearly trend in seasonal means of $\langle \tilde{A}^* \rangle \cos\phi$ and $\langle u \rangle \cos\phi$ computed from the 1979-2016 ERA-Interim reanalysis data. There are significant geographical and seasonal variations in the trends of LWA. For example, there is a decreasing trend in the eastern North Pacific. In the Atlantic, the trend in summer is positive in latitudes higher than 50°N and negative to the south, but the signal is much weaker in winter. There are clearly opposite trends in the zonal flow, namely, where LWA increases the flow decreases and vice versa. Preliminary analyses show that over regions with significant trends (either increasing or decreasing), there are shifts in the breakdown of LWA budget terms that suggests long term changes in the non-conservative forcing (residual term). Simulations with GCMs are necessary to parse out the relative contributions of non-conservative processes such as frictional dissipation and increased diabatic heating to the shift of LWA budget.

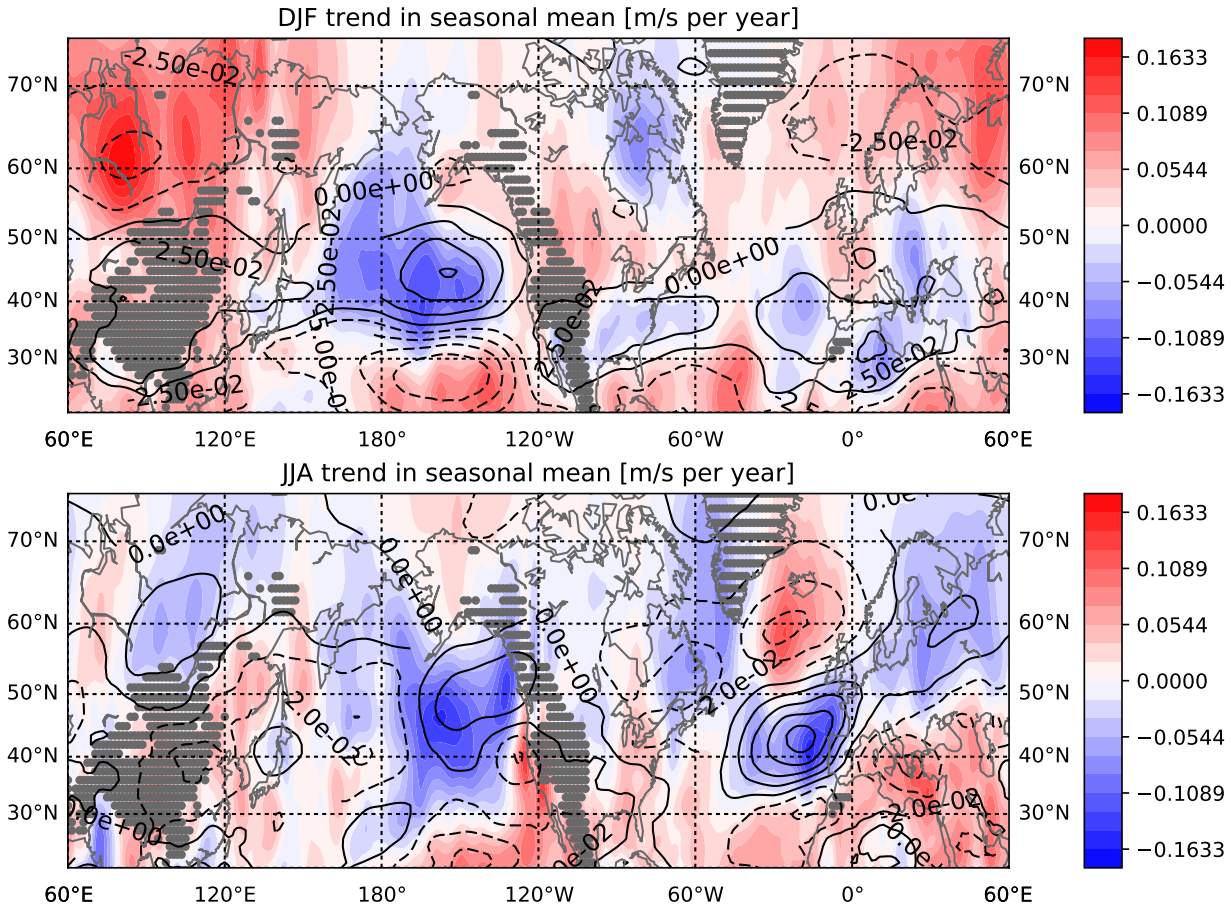

Figure 5.3: Color: Trend in DJF (left) and JJA (right) mean $\langle \tilde{A}^* \rangle \cos\phi$ over 1979-2016 [m/s per year]. Contours: Trend in DJF (left) and JJA (right) mean $\langle u \rangle \cos\phi$ over the same period. Dashed lines indicate negative values. Dotted region indicates trends with $p < 0.05$ from regression. Source: ERA-Interim reanalysis.

Appendices

APPENDIX A

NUMERICAL SOLVER FOR THE EIGENVALUE PROBLEM (2.10)

In this initial value problem, the initial vorticity gradient is

$$\begin{aligned}\gamma(\phi) &= \frac{1}{a}\frac{\partial}{\partial\phi}\left(2\Omega\sin\phi - \frac{1}{a\cos\phi}\frac{\partial}{\partial\phi}(\bar{u}\cos\phi)\right) \\ &\text{`} = \frac{1}{a}\frac{\partial}{\partial\phi}\left[2\Omega\sin\phi - \frac{1}{a}(2A - 4B\cos^2\phi + 7C\cos^5\phi - 9C\cos^7\phi)\right] \end{aligned} \tag{A.1}$$

The laplacian operator ∇_m^2 in (2.11) is discretized as

$$\begin{aligned}\nabla_m^2\zeta \approx \frac{1}{(a\mu_j)^2}\frac{1}{(2\Delta\phi)^2}\Big[&\mu_j\mu_{j+1/2}\zeta_{j+1} - \left(\mu_j\mu_{j+1/2} + \mu_j\mu_{j-1/2} + (2m\Delta\phi)^2\right)\zeta_j \\ &+\mu_j\mu_{j-1/2}\zeta_{j-1}\Big]\end{aligned} \tag{A.2}$$

The inverse of (A.2) is obtained numerically with the `scipy.sparse.linalg.inv` function in the Scipy package (Jones et al., 2014). The eigenvalue problem is solved with `scipy.sparse.linalg.eigs`.

APPENDIX B

DEFINITION OF QUASI-GEOSTROPHIC POTENTIAL VORTICITY (QGPV)

The QGPV q is defined by

$$q \equiv f + \zeta + f e^{z/H} \frac{\partial}{\partial z} \left(e^{-z/H} \frac{\theta - \tilde{\theta}}{\partial \tilde{\theta} / \partial z} \right), \tag{B.1}$$

where z is the pressure pseudo-height [$z \equiv -H \ln(p/p_0)$; p is pressure, $p_0 = 1000$ hPa and $H = 7$ km is assumed], $f = 2\Omega \sin\phi$ is the Coriolis parameter, $\Omega \equiv 7.29 \times 10^{-5}$ s^{-1} is the planet's rotation rate, ζ is relative vorticity, θ is potential temperature, $\tilde{\theta}(z,t)$ is the area-weighted hemispheric average of θ (in this thesis average over the Northern Hemisphere), and $\partial\tilde{\theta}/\partial z$ is static stability.

APPENDIX C

DEFINITION AND CALCULATION OF FINITE-AMPLITUDE LOCAL WAVE ACTIVITY (LWA) IN SPHERICAL COORDINATES

The small-amplitude wave activity (negative pseudomomentum density) is defined as the square of eddy QGPV $q' \equiv q - \bar{q}$ divided by twice the zonal-mean QGPV gradient. In spherical coordinates (see for example Solomon and Nakamura (2012))

$$A = \frac{a}{2}\frac{{q'}^2}{\partial\bar{q}/\partial\phi} \approx \frac{a}{2}\frac{\partial\bar{q}}{\partial\phi}(\Delta\phi)^2, \tag{C.1}$$

where $\overline{(...)}$ and $(...)'$ denote the zonal mean and the departure from it; a (=6378 km) and ϕ are the radius and latitude of the planet; and $\Delta\phi$ specifies the meridional displacement of the contour of q relative to ϕ.

Finite-amplitude local wave activity (LWA) quantifies the meridional displacement of QGPV from a zonally symmetric reference state at given longitude λ, latitude ϕ, pressure pseudoheight z, and time t. Reformulating Eq. (12) of Huang and Nakamura (2016) (hereafter HN16) for spherical coordinates, LWA in the interior is defined as

$$\tilde{A}^*(\lambda,\phi,z,t) = -\frac{a}{\cos\phi}\int_0^{\Delta\phi} q_e(\lambda,\phi,\phi',z,t)\cos(\phi+\phi')d\phi', \tag{C.2}$$

where $q_e(\lambda,\phi,\phi',z,t)$ measures the meridional displacement of QGPV field relative to a zonally symmetric reference state $q_{REF}(\phi,z,t)$:

$$q_e(\lambda,\phi,\phi',z,t) \equiv q(\lambda,\phi+\phi',z,t) - q_{REF}(\phi,z,t). \tag{C.3}$$

The definition of q_{REF} will be discussed shortly. In (C.3) ϕ' is the latitude relative to ϕ: this is the coordinate that describes the meridional structure of q_e, whereas ϕ is simply a

reference latitude (q_e needs to be redefined for different ϕ since q_{REF} varies with ϕ). Note that $\phi' = \Delta\phi(\lambda, \phi, z, t)$ specifies the meridional deviation of the QGPV contour $q = q_{REF}$ from latitude ϕ, so $q_e(\lambda, \phi, \Delta\phi, z, t) = 0$. Note also that $\Delta\phi$ can be multivalued at a given longitude λ (see Fig.1 of HN16). As shown by HN16, the zonal average of $\tilde{A}^*$ equals finite-amplitude wave activity (FAWA) of Nakamura and Zhu (2010) (hereafter NZ10). In the small-amplitude limit (C.2) approaches (C.1).

Computation of LWA thus entails the following steps: (i) compute q and q_{REF}; (ii) compute q_e with (C.3) and then evaluate (C.2) for $\tilde{A}^*$. Following Nakamura and Solomon (2010) (hereafter NS10), we first interpolate vertically the horizontal velocity (u, v) and temperature T from the ERA-Interim reanalysis product (Dee et al., 2011) at each longitude-latitude grid (i, j) onto a uniformly spaced 49 pseudoheight levels [$z_k = (k-1)\Delta z$, $\Delta z =$ 1 km, $1 \le k \le 49$]. Then for each (i, j, k) we compute potential temperature $\theta_{ijk} = T_{ijk}e^{\kappa z_k/H}$, where T_{ijk} is the interpolated temperature, $\kappa = R/c_p, R = 287\ JK^{-1}kg^{-1}, c_p = 1004\ JK^{-1}kg^{-1}, H \equiv 7$ km. We also compute the area-weighted hemispheric-mean potential temperature $\tilde{\theta}_k$ over the Northern Hemisphere. QGPV q is then computed using the formula

$$q_{ijk} = 2\Omega \sin\phi_j + \frac{1}{a\cos\phi_j}\frac{v_{i+1jk} - v_{i-1jk}}{2\Delta\lambda} - \frac{1}{a\cos\phi_j}\frac{u_{ij+1k}\cos\phi_{j+1} - u_{ij-1k}\cos\phi_{j-1}}{2\Delta\phi} + 2\Omega\sin\phi_j e^{z_k/H}\left[\frac{e^{-z_{k+1}/H}\left(\theta_{ijk+1} - \tilde{\theta}_{k+1}\right)}{\tilde{\theta}_{k+2} - \tilde{\theta}_k} - \frac{e^{-z_{k-1}/H}\left(\theta_{ijk-1} - \tilde{\theta}_{k-1}\right)}{\tilde{\theta}_k - \tilde{\theta}_{k-2}}\right], \quad \text{(C.4)}$$

where $\Delta\lambda = \Delta\phi = 1.5^\circ \times (\pi/180^\circ)$, and $\phi_j = (j-1)\Delta\phi - 0.5\pi$, $1 \le j \le 121$. Note that (C.4) applies only to the 'interior' points ($1 < j < 121, 1 < k < 49$), and at $k = 48$ the denominator of the first term in the square bracket is replaced by $2\left(\tilde{\theta}_{k+1} - \tilde{\theta}_k\right)$ and at $k = 2$ the denominator of the last term is replaced by $2\left(\tilde{\theta}_k - \tilde{\theta}_{k-1}\right)$.

The reference state q_{REF} is obtained by zonalizing the instantaneous QGPV through an area-preserving map. At each level k, the horizontal grids (i, j) in the Northern Hemisphere are sorted according to equally spaced 121 values of q between the minimum and maximum

values at that level [$Q_{nk} = (n-1)\Delta Q_k,\ 1 \le n \le 121,\ \Delta Q_k = (\max(q_{ijk}) - \min(q_{ijk}))/120$]. Typically there is a small portion of the Northern Hemisphere tropics in which $q_{ijk} < 0$, so the minimum value is slightly less than 0. We then compute the area of the region in which $q_{ijk} \ge Q_{nk}$ [$\equiv A_{nk}(Q_{nk})$] by conditional box counting, weighting each grid with a fractional area $a^2 \cos\phi_j \Delta\lambda\Delta\phi$. In doing so, we exclude the points that lie underneath the surface topography. The area $A_{nk}(Q_{nk})$ is then mapped to equivalent latitude with the formula

$$\phi_{nk} \equiv \sin^{-1}\left(1 - \frac{A_{nk}}{A_{1k}}\right), \tag{C.5}$$

which effectively associates the minimum QGPV with the equator and the maximum QGPV with the North Pole. This establishes the one-to-one relation between latitude and QGPV $\phi_{nk} = \phi_{nk}(Q_{nk})$ on kth level. Finally by inverting this relationship one obtains QGPV as a function of latitude for given height and time, which defines $q_{REF}(\phi_j, z_k, t)$ for the Northern Hemisphere. To the extent that QGPV is materially conserved by a nondivergent (i.e. area-preserving) flow at each height, q_{REF} is invariant in time (NZ10, NS10).

After obtaining q_e from q and q_{REF} using (C.3), we compute LWA by evaluating (C.2). Since q_{REF} increases with latitude, $q_e < 0$ where the QGPV contour $q = q_{REF}$ is displaced northward from ϕ (i.e. $\Delta\phi > 0$), and $q_e > 0$ where it is displaced southward ($\Delta\phi < 0$), either way making (C.2) positive. Care must be taken when $\Delta\phi$ is multivalued due to an overturned or cutoff QGPV contour. To take care of this situation automatically, the line integral in (C.2) is evaluated for each λ by scanning the entire latitudes from the equator to the North Pole and collecting all contributions from ($q_e < 0, \phi' > 0$) and ($q_e > 0, \phi' < 0$) (see Fig.1 of HN16).

APPENDIX D

DERIVATION OF THE ZONAL WIND AND LWA EQUATIONS IN SPHERICAL COORDINATES

The equation for angular momentum in the (λ, ϕ, z) coordinate reads

$$\frac{\partial}{\partial t}(u\cos\phi)+\frac{u}{a}\frac{\partial u}{\partial \lambda}+\frac{v\cos\phi}{a}\frac{\partial u}{\partial \phi}+w\cos\phi\frac{\partial u}{\partial z}-\left(f\cos\phi+\frac{u\sin\phi}{a}\right)v=-\frac{1}{a}\frac{\partial \psi}{\partial \lambda}+\dot{u}\cos\phi, \quad \text{(D.1)}$$

where $(u, v, w) \equiv (a\cos\phi\, d\lambda/dt, a d\phi/dt, dz/dt)$ is wind velocity, ψ is geopotential, $\dot{u}$ is non-conservative sources-sinks of zonal momentum. Similar to q, we partition u and v as

$$u_e(\lambda, \phi, \phi', z, t) \equiv u(\lambda, \phi+\phi', z, t) - u_{REF}(\phi, z, t), \quad \text{(D.2)}$$

$$v_e(\lambda, \phi, \phi', z, t) \equiv v(\lambda, \phi+\phi', z, t). \quad \text{(D.3)}$$

See section 4 below for the definition of u_{REF}. Since

$$\frac{\partial u}{\partial \phi}=\frac{\partial u_e}{\partial \phi'}, \quad \frac{\partial v}{\partial \phi}=\frac{\partial v_e}{\partial \phi'}, \quad \text{(D.4)}$$

(D.1) becomes:

$$\frac{\partial}{\partial t}(u\cos\phi)+\frac{u}{a}\frac{\partial u_e}{\partial \lambda}+\frac{v_e\cos\phi}{a}\frac{\partial u_e}{\partial \phi'}+w\cos\phi\frac{\partial u}{\partial z}-\left(f\cos\phi+\frac{u\sin\phi}{a}\right)v_e=-\frac{1}{a}\frac{\partial \psi}{\partial \lambda}+\dot{u}\cos\phi. \quad \text{(D.5)}$$

With mass continuity

$$\frac{1}{a\cos(\phi+\phi')}\frac{\partial u_e}{\partial \lambda}+\frac{1}{a\cos(\phi+\phi')}\frac{\partial}{\partial \phi'}\left(v_e\cos(\phi+\phi')\right)+e^{z/H}\frac{\partial}{\partial z}\left(e^{-z/H}w\right)=0 \quad \text{(D.6)}$$

(D.5) can be written in the flux form evaluated at latitude ϕ ($\phi' = 0$):

$$\frac{\partial}{\partial t}(u\cos\phi) + \frac{u_{REF}}{a}\frac{\partial u_e}{\partial \lambda} + \frac{1}{a}\frac{\partial u_e^2}{\partial \lambda} + \frac{1}{a}\frac{\partial\left(u_e\, v_e \cos(\phi+\phi')\right)}{\partial \phi'} + e^{z/H}\frac{\partial}{\partial z}\left(w\, e^{-z/H} u_e \cos\phi\right)$$
$$= -w\cos\phi\frac{\partial u_{REF}}{\partial z} + \left(f\cos\phi + \frac{u\sin\phi}{a}\right)v_e - \frac{1}{a}\frac{\partial \psi}{\partial \lambda} + \dot{u}\cos\phi. \tag{D.7}$$

Further rearranging terms

$$\begin{aligned} & \frac{\partial}{\partial t}\left(u\cos\phi\right) + \frac{1}{a}\frac{\partial}{\partial \lambda}\left(u_{REF}u_e + u_e^2\right) \\ + \;& \frac{1}{a\cos\phi}\frac{\partial}{\partial \phi'}\left(u_e v_e \cos^2(\phi+\phi')\right) + e^{z/H}\frac{\partial}{\partial z}\left(we^{-z/H}u_e\cos\phi\right) \\ = \;& -w\cos\phi\frac{\partial u_{REF}}{\partial z} + \left(f\cos\phi + \frac{u_{REF}\sin\phi}{a}\right)v_e - \frac{1}{a}\frac{\partial\psi}{\partial\lambda} + \dot{u}\cos\phi. \end{aligned} \tag{D.8}$$

By applying the density weighted vertical average [(3.29) in the main text] and assuming that the vertical velocity vanishes at the boundaries

$$\begin{aligned} & \frac{\partial}{\partial t}\langle u\cos\phi\rangle + \frac{1}{a}\frac{\partial}{\partial\lambda}\left\langle u_{REF}u_e + u_e^2\right\rangle + \frac{1}{a\cos\phi}\frac{\partial}{\partial\phi'}\left\langle u_e v_e\cos^2(\phi+\phi')\right\rangle \\ = \;& -\left\langle w\cos\phi\frac{\partial u_{REF}}{\partial z}\right\rangle + \left\langle\left(f\cos\phi + \frac{u_{REF}\sin\phi}{a}\right)v_e\right\rangle - \frac{1}{a}\frac{\partial\langle\psi\rangle}{\partial\lambda} + \langle\dot{u}\cos\phi\rangle. \end{aligned} \tag{D.9}$$

With the QG scaling, the first term on the RHS and the correction term to the Coriolis acceleration are negligible. Therefore,

$$\begin{aligned} & \frac{\partial}{\partial t}\langle u\cos\phi\rangle + \frac{1}{a}\frac{\partial}{\partial\lambda}\underbrace{\langle(u_{REF}+u_e)u_e\rangle}_{F_u} + \frac{1}{a\cos\phi}\frac{\partial\left\langle u_e\, v_e\cos^2(\phi+\phi')\right\rangle}{\partial\phi'} \\ = \;& \underbrace{\langle f\, v_e\cos\phi\rangle - \frac{1}{a}\frac{\partial\langle\psi\rangle}{\partial\lambda}}_{G_u} + \langle\dot{u}\cos\phi\rangle\,. \end{aligned} \tag{D.10}$$

F_u and G_u represent, respectively, the zonal advective flux of eddy angular momentum and the Coriolis torque of the ageostrophic meridional velocity. This is a generalization of Eq. (29) of HN16.

Likewise, the spherical version of the LWA equation (3.28) evaluated at latitude ϕ ($\phi' = 0$) is

$$\begin{aligned}
&\frac{\partial}{\partial t}\langle \tilde{A}^* \rangle \cos\phi \\
&= -\frac{1}{a}\frac{\partial F_A}{\partial \lambda} + \frac{1}{a\cos\phi}\frac{\partial}{\partial \phi'}\left(\langle u_e v_e \rangle \cos^2(\phi+\phi')\right) + \frac{f\cos\phi}{H}\left(\frac{v_e\theta_e}{\partial\tilde{\theta}/\partial z}\right)_{z=0} + \left\langle \dot{\tilde{A}}^* \right\rangle \cos\phi,
\end{aligned} \tag{D.11}$$

where

$$F_A = \left\langle u_{REF}\, \tilde{A}^* \right\rangle - \frac{a}{\cos\phi}\left\langle \int_0^{\Delta\phi} u_e q_e \cos(\phi+\phi') d\phi' \right\rangle + \frac{1}{2}\left\langle v_e^2 - u_e^2 - \frac{R}{H}\frac{e^{-\kappa z/H}\theta_e^2}{\partial\tilde{\theta}/\partial z} \right\rangle. \tag{D.12}$$

The last term in (D.11) represents nonconservative sources-sinks of LWA, whereas the sum of the last term in $-\frac{1}{a}\frac{\partial F_A}{\partial \lambda}$ and the following two terms arises from the vertical average of the meridional QGPV flux through Taylor's identity:

$$\begin{aligned}
\cos\phi\,\langle v_e q_e \rangle = \frac{1}{a}\frac{\partial}{\partial\lambda}\left\langle \frac{1}{2}\left(v_e^2 - u_e^2 - \frac{R}{H}\frac{e^{-\kappa z/H}\theta_e^2}{\partial\tilde{\theta}/\partial z}\right)\right\rangle - \frac{1}{a\cos\phi}\frac{\partial}{\partial\phi'}\left\langle u_e v_e \cos^2(\phi+\phi')\right\rangle \\
- \frac{f\cos\phi}{H}\left(\frac{v_e\theta_e}{\partial\tilde{\theta}/\partial z}\right)_{z=0} \qquad \text{evaluated at } \phi' = 0,
\end{aligned} \tag{D.13}$$

in which the RHS is the column average of the divergence of the 3D EP flux and will play an important role in the LWA budget. Note in the above

$$\theta_e(\lambda,\phi,\phi',z,t) \equiv \theta(\lambda,\phi+\phi',z,t) - \theta_{REF}(\phi,z,t), \tag{D.14}$$

where θ_{REF} is the reference-state potential temperature to be defined in Appendix E.

APPENDIX E

SOLVING FOR THE REFERENCE STATE

To evaluate (u_e, v_e, θ_e) in (D.11) from (D.2), (D.3), and (D.14), one needs to first compute the zonally uniform reference state (u_{REF}, θ_{REF}). This reference state is related to q_{REF} through

$$q_{REF}(\mu, z, t) = 2\,\Omega\,\mu - \frac{1}{a}\frac{\partial}{\partial \mu}\left(u_{REF}\cos\phi\right) + 2\,\Omega\,\mu\, e^{z/H}\frac{\partial}{\partial z}\left(\frac{e^{-z/H}(\theta_{REF} - \tilde{\theta})}{\partial\tilde{\theta}/\partial z}\right), \quad \text{(E.1)}$$

where $\mu \equiv \sin\phi$. Using thermal wind balance

$$2\,\Omega\,\mu\,\frac{\partial\left(u_{REF}\cos\phi\right)}{\partial z} = -\frac{R(1-\mu^2)\,e^{-\kappa z/H}}{Ha}\frac{\partial\theta_{REF}}{\partial\mu} \quad \text{(E.2)}$$

(E.1) may be transformed into an elliptic equation for $u_{REF}\cos\phi$

$$\begin{aligned} &\frac{\partial}{\partial\mu}\left[\frac{1}{2\Omega\mu}\frac{\partial\left(u_{REF}\cos\phi\right)}{\partial\mu}\right] + \frac{2\Omega H a^2\mu}{R(1-\mu^2)}e^{z/H}\frac{\partial}{\partial z}\left[\frac{e^{(\kappa-1)z/H}\partial\left(u_{REF}\cos\phi\right)/\partial z}{\partial\tilde{\theta}/\partial z}\right] \\ = \;& -a\frac{\partial}{\partial\mu}\left(\frac{q_{REF}}{2\Omega\mu}\right). \end{aligned} \quad \text{(E.3)}$$

Alternatively (and equivalently) NS10 derive an equation [their Eq. (12)] for u_{REF} using the zonal-mean wind and finite-amplitude wave activity:

$$\left[\frac{\partial^2}{\partial\mu^2} + e^{z/H}\frac{\partial}{\partial z}\left(e^{-z/H}\epsilon\frac{\partial}{\partial z}\right)\right]\left(\frac{(\bar{u} - u_{REF})\cos\phi}{2\,\Omega\,\mu}\right) = -\frac{\partial^2}{\partial\mu^2}\left(\frac{A^*\cos\phi}{2\,\Omega\,\mu}\right), \quad \text{(E.4)}$$

where

$$\epsilon \equiv \frac{4\,\Omega^2\,\mu^2\,a^2 H e^{\kappa z/H}}{R(1-\mu^2)\partial\tilde{\theta}/\partial z}, \quad \text{(E.5)}$$

and $\bar{u}$ and A^* are the zonal mean of instantaneous u and $\tilde{A}^*$, respectively. Note that the above expression of ϵ corrects for a typo in NS10. In this study we use (E.4) to solve for u_{REF}. Unlike NS10 we restrict the domain to the Northern Hemisphere and discretize it

using equally spaced grids in μ and z. Then $\bar{u}$ and A^* are interpolated onto each (μ, z) grid. Equation (E.4) is discretized on the interior grids using central finite difference.

The assumed boundary conditions are: (i) $u_{REF} \cos\phi = 0$ at the North Pole; (ii) $(\bar{u} - u_{REF})/\mu = A^*/\mu = 0$ at the equator; (iii) u_{REF} at the top level ($k = 49$) is extrapolated from $k = 47$ using the vertical shear at $k = 48$ based on the thermal wind relation (E.2), where θ_{REF} at $k = 48$ is estimated with a procedure similar to the one used for computing q_{REF} from q; (iv) no slip lower boundary condition, i.e., $u_{REF} = 0$ at $z = 0$.

Of the four boundary conditions, the second condition at the equator is least defensible since $\mu = 0$ there, and in reality A^* does not vanish at the equator. This choice artificially suppresses the eddy-mean flow interaction in the deep tropics, but the QG assumption is questionable there in the first place. We have tested other forms of southern boundary condition and found that they do not affect the solution in the extratropics significantly. The no-slip lower boundary condition for u_{REF} is chosen because a non-zero surface zonal wind would imply the effect of angular momentum transport by the eddy against surface friction and therefore contradicts the assumption of an eddy-free reference state. NS10 and Methven and Berrisford (2015) also consider an adiabatic lower boundary condition and find some significant quantitative difference from the no-slip boundary condition. The difference accounts for the arrangement of angular momentum by an implied meridional displacement caused by surface friction.

After discretizing (E.4) and obtaining a system of linear equations, we use `spsolve` available in the *Scipy* python library (Jones et al., 2014) to invert the sparse matrix to solve for u_{REF}. We reconstruct θ_{REF} using the thermal wind relation (E.2). For the lower boundary the vertical shear is estimated from the difference between $k = 2$ and $k = 1$. On each k a constant is added to θ_{REF} such that its area-weighted hemispheric mean value equals $\tilde{\theta}_k$.

APPENDIX F

EVALUATION OF THE TERMS IN THE LWA EQUATION FROM DATA

Once the reference state (u_{REF}, θ_{REF}) is obtained, (u_e, v_e, θ_e) may be computed from (D.2), (D.3), and (D.14) using data, and hence the terms in (D.11) may be evaluated. We approximate the density weighted vertical average $\langle(\cdots)\rangle$ [(3.29) in the main text] with the summation

$$\langle(\cdots)\rangle \approx \frac{\sum_{k=2}^{48}(\cdots)_k e^{-z_k/H}\Delta z}{\sum_{k=2}^{48} e^{-z_k/H}\Delta z} = \frac{\sum_{k=2}^{48}(\cdots)_k e^{-z_k/H}\Delta z}{6.5 \text{ km}}. \tag{F.1}$$

Note that $H = 7$ km in the denominator has been truncated to 6.5 km due to discretization. With this approximation, the low-level meridional heat flux, the last term in (D.13), will consist of the contributions from $k = 1$ and $k = 2$ ($z = 0$ and 1 km) due to the form of vertical discretization of QGPV (C.4).

$$\frac{f\cos\phi}{H}\left(\frac{v_e\theta_e}{\partial\tilde{\theta}/\partial z}\right)_{z=0} \approx \frac{2\Omega\sin\phi_j\cos\phi_j}{6.5 \text{ km}}\left(\frac{e^{-z_2/H}v_{e\,ij2}\theta_{e\,ij2}}{\tilde{\theta}_3-\tilde{\theta}_1}+\frac{v_{e\,ij1}\theta_{e\,ij1}}{2(\tilde{\theta}_2-\tilde{\theta}_1)}\right)\Delta z. \tag{F.2}$$

Since the sea-level temperature may not be reliable where topography is high, points at which the surface elevation is higher than 1 km are excluded from the analysis. For modest topography (i.e. $0 < z_s < 1$ km), we used the surface 2-meter potential temperature $\theta_{2m} = T_{2m}\,(p_0/p_s)^\kappa$ evaluated with the values provided by the ERA-Interim, where p_s is surface pressure and $p_0 = 1000$ hPa, to compute θ_{eij1} in (F.2) above. Besides this method, we have also tried: (1) using the sea-level temperature values available in the ERA-Interim dataset (based on vertical extrapolation with an assumed lapse rate), (2) replacing $\theta(z = 0)$ with $\theta(z = 0) + z_s\frac{\partial\tilde{\theta}}{\partial z}|_{z=0}$, and (3) when computing the column average LWA and fluxes in (D.11), replace QGPV values at 'underground' points with those at the lowest-level 'above-ground' point assuming that QGPV is not strongly stratified. The spatial distribution and relative

magnitudes of wave activity and fluxes over the oceanic regions do not change significantly, indicating the results presented above are robust and not sensitive to the boundary treatment chosen.

To evaluate the RHS terms of (F.2), we compute $\theta_{e\,ijk} = \theta_{ijk} - \theta_{REF,jk}$ for k=1,2. $\theta_{REF,j2}$ has been obtained by the method outlined in section 4, whereas $\theta_{REF,j1}$ is obtained by the box-counting method analogous to the calculation of q_{REF}.

APPENDIX G

SENSITIVITY ANALYSIS: CHOICES OF SPATIAL-AVERAGING DOMAIN IN COSPECTRAL ANALYSES

To test the robustness of the regional cospectra presented in Figs.4.12 and 4.13 of the main text against the choice of averaging domain, we repeat the analysis with different domain definitions listed in Table G.1. The maps of the corresponding domains are shown in Figs.G.1, G.3 and G.5, whereas the resulting cospectra are shown in Figs.G.2, G.4 and G.6, respectively. Relative magnitudes and the shapes of the cospectra over the synoptic timescales are similar: in all cases, tendency of LWA $>$ zonal LWA flux convergence $\geq$ residual (i.e. net diabatic contributions) $\gg$ low-level meridional heat flux $>$ meridional momentum flux divergence. The results from Set 2 and 3 are combined to be presented in Figs.4.12 and 4.13 of the main text with the shades and lines.

Table G.1: Choices of oceanic domain for spatial averaging

Set of choices		**Pacific**	**Atlantic**
Set 1	Longitude Range	$120^\circ - 237^\circ$ E	75° W -15° E
	Latitude Range	$30^\circ - 60^\circ$ N	$30^\circ - 60^\circ$ N
	Excluding Land Grids	Yes	Yes
Set 2	Longitude Range	$120^\circ - 237^\circ$ E	90° W -30° E
(Bounds of shades in	Latitude Range	$30^\circ - 75^\circ$ N	$30^\circ - 75^\circ$ N
Figs.4.12 and 4.13)	Excluding Land Grids	Yes	Yes
Set 3	Longitude Range	$120^\circ - 237^\circ$ E	90° W -30° E
(Solid lines in Figs.4.12 and 4.13)	Latitude Range	$30^\circ - 75^\circ$ N	$30^\circ - 75^\circ$ N
	Excluding Land Grids	No	No

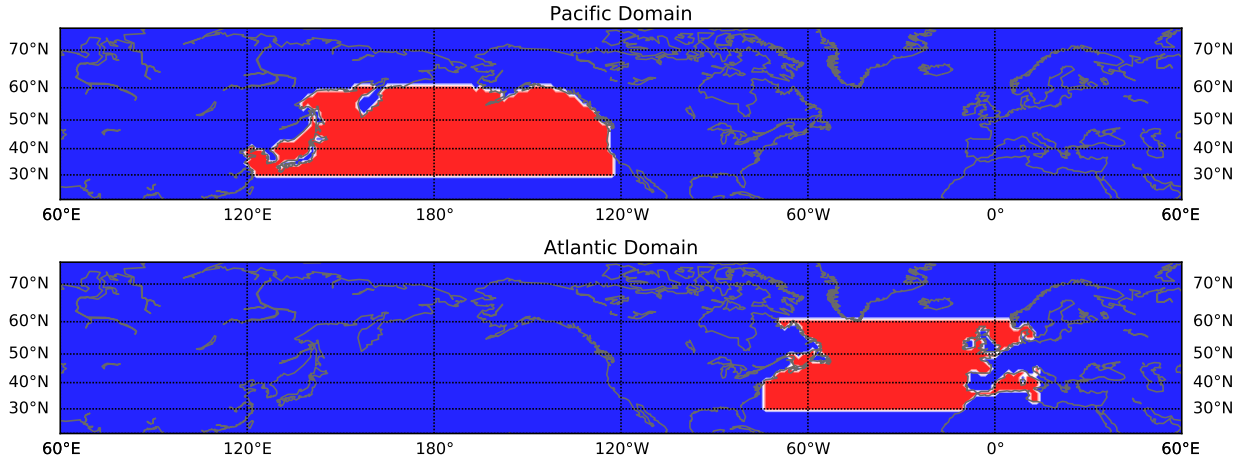

Figure G.1: Pacific and Atlantic domains for Test Set 1.

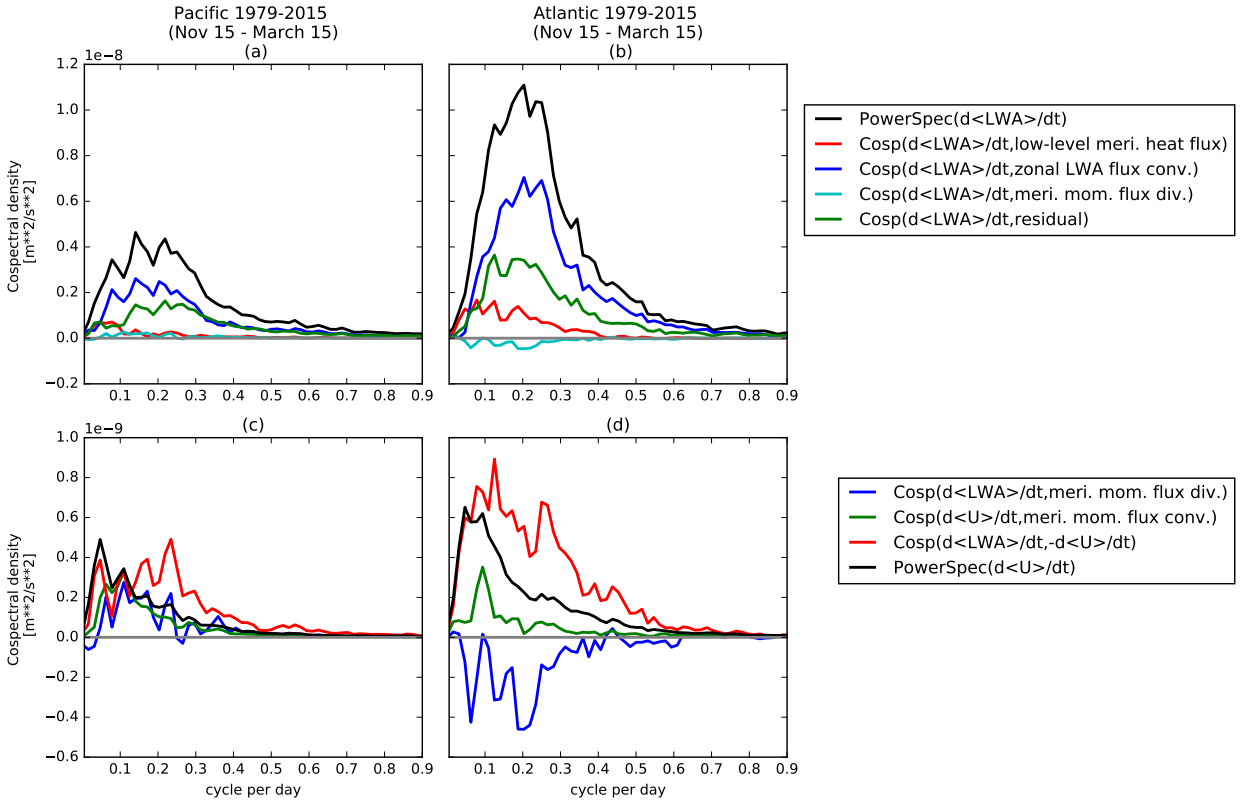

Figure G.2: Cospectra computed with averaging domain Set 1.

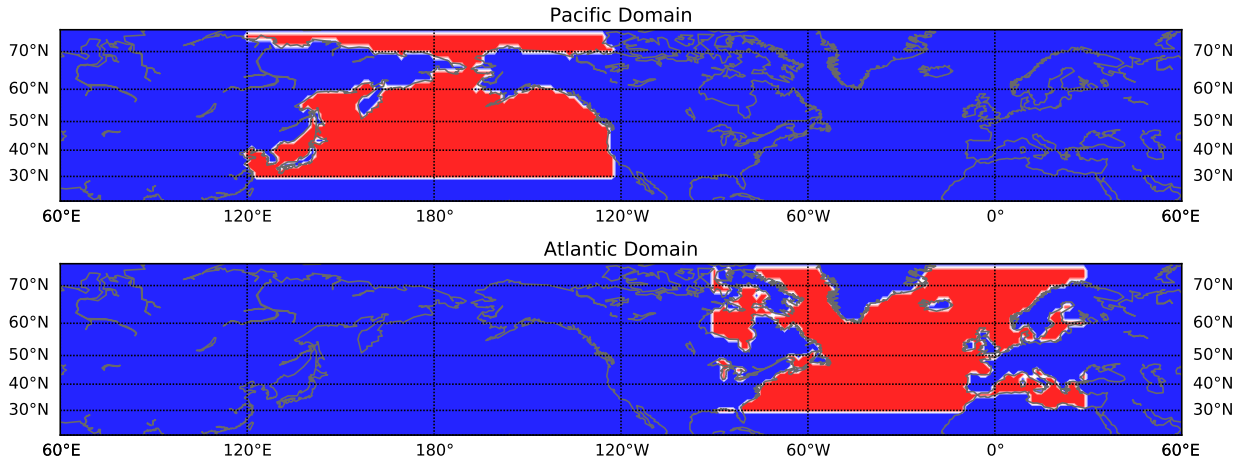

Figure G.3: Pacific and Atlantic domains for Test Set 2.

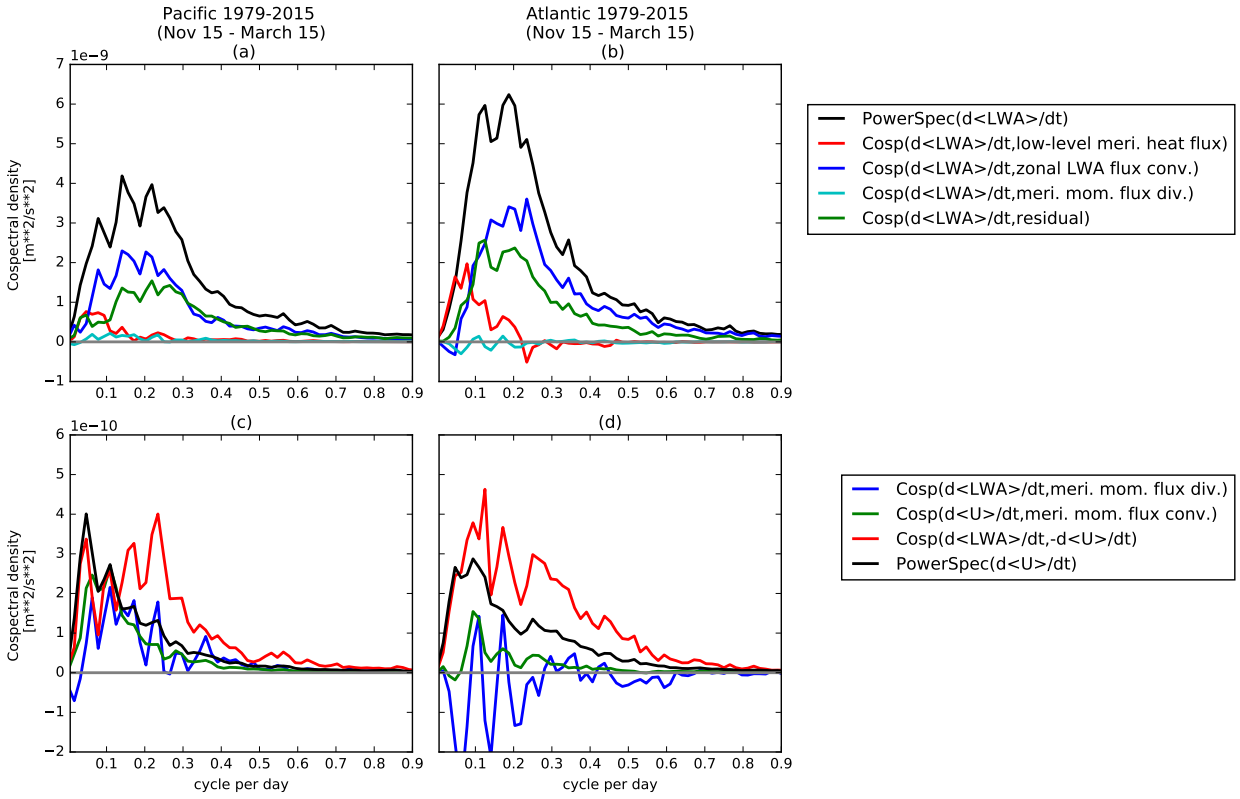

Figure G.4: Cospectra computed with averaging domain Set 2.

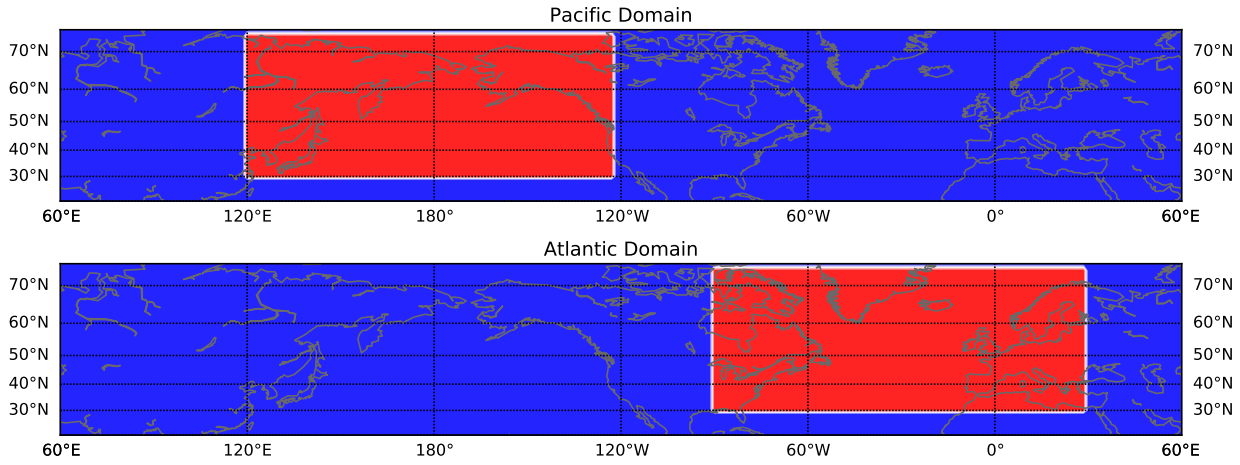

Figure G.5: Pacific and Atlantic domains for Test Set 3.

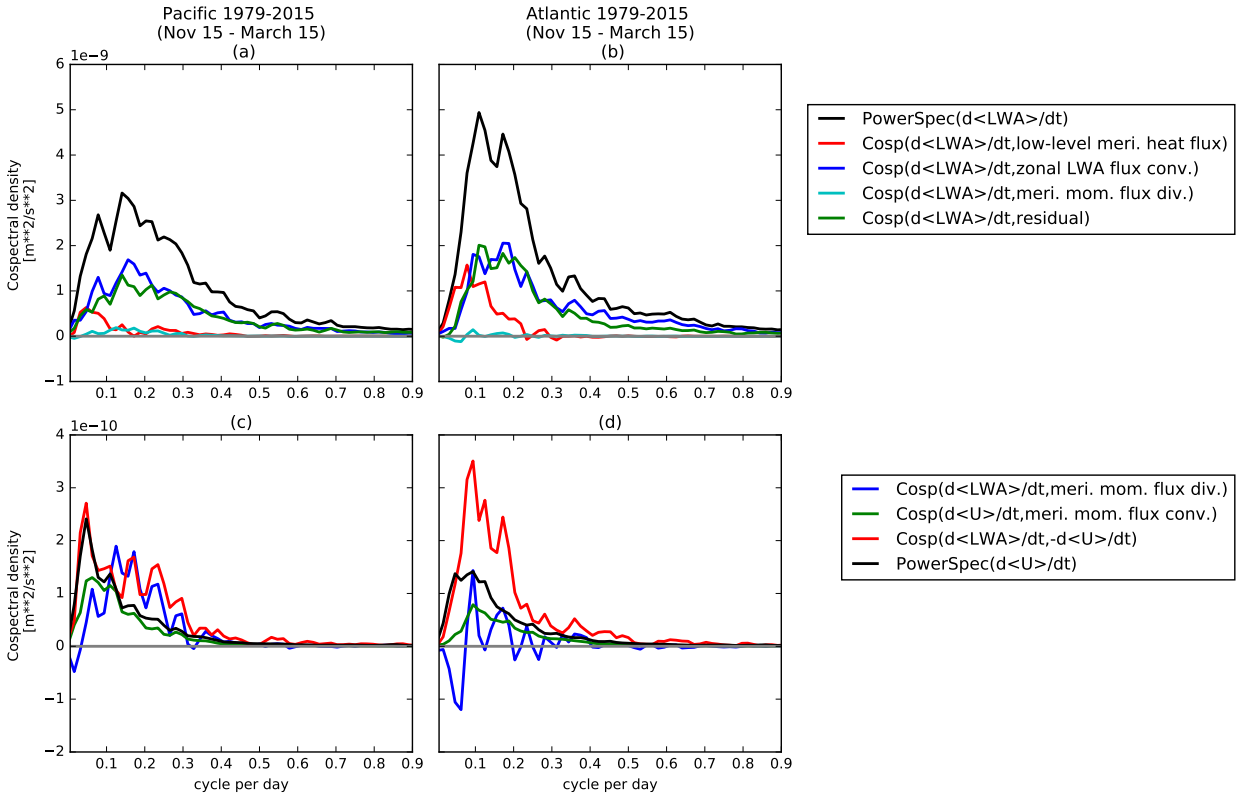

Figure G.6: Cospectra computed with averaging domain Set 3.

REFERENCES

Allen, D. R. and Nakamura, N. (2003). Tracer equivalent latitude: A diagnostic tool for isentropic transport studies. *Journal of the atmospheric sciences*, 60(2):287–304.

Altenhoff, A. M., Martius, O., Croci-Maspoli, M., Schwierz, C., and Davies, H. C. (2008). Linkage of atmospheric blocks and synoptic-scale rossby waves: a climatological analysis. *Tellus A*, 60(5):1053–1063.

Ambaum, M. H., Hoskins, B. J., and Stephenson, D. B. (2001). Arctic oscillation or north atlantic oscillation? *Journal of Climate*, 14(16):3495–3507.

Andrews, D. and McIntyre, M. E. (1976). Planetary waves in horizontal and vertical shear: The generalized eliassen-palm relation and the mean zonal acceleration. *J. Atmos. Sci.*, 33:2031–2048.

Andrews, D. G. and McIntyre, M. (1978). An exact theory of nonlinear waves on a lagrangian-mean flow. *Journal of Fluid Mechanics*, 89(4):609–646.

Barnes, E. A., Dunn-Sigouin, E., Masato, G., and Woollings, T. (2014). Exploring recent trends in northern hemisphere blocking. *Geophysical Research Letters*, 41(2):638–644.

Barnes, E. A. and Hartmann, D. L. (2012). Detection of rossby wave breaking and its response to shifts of the midlatitude jet with climate change. *Journal of Geophysical Research: Atmospheres*, 117(D9):n/a–n/a. D09117.

Barnes, E. A., Slingo, J., and Woollings, T. (2012). A methodology for the comparison of blocking climatologies across indices, models and climate scenarios. *Climate dynamics*, 38(11-12):2467–2481.

Barriopedro, D., García-Herrera, R., Lupo, A. R., and Hernández, E. (2006). A climatology of northern hemisphere blocking. *Journal of Climate*, 19(6):1042–1063.

Berrisford, P., Hoskins, B., and Tyrlis, E. (2007). Blocking and rossby wave breaking on the dynamical tropopause in the southern hemisphere. *Journal of the Atmospheric Sciences*, 64(8):2881–2898.

Blake, E. S., Kimberlain, T. B., Berg, R. J., Cangialosi, J., and Beven II, J. L. (2013). Tropical cyclone report: Hurricane sandy. *National Hurricane Center*, 12:1–10.

Bretherton, F. P. (1966). The propagation of groups of internal gravity waves in a shear flow. *Quarterly Journal of the Royal Meteorological Society*, 92(394):466–480.

Bühler, O. (2014). *Waves and mean flows*. Cambridge University Press.

Butchart, N. and Remsberg, E. E. (1986). The area of the stratospheric polar vortex as a diagnostic for tracer transport on an isentropic surface. *Journal of the atmospheric sciences*, 43(13):1319–1339.

Chang, E. K. (2001). The structure of baroclinic wave packets. *Journal of the atmospheric sciences*, 58(13):1694–1713.

Chang, E. K., Lee, S., and Swanson, K. L. (2002). Storm track dynamics. *Journal of Climate*, 15(16):2163–2183.

Charney, J. G. and Drazin, P. G. (1961). Propagation of planetary-scale disturbances from the lower into the upper atmosphere. *Journal of Geophysical Research*, 66(1):83–109.

Chen, G., Lu, J., Burrows, D. A., and Leung, L. R. (2015). Local finite-amplitude wave activity as an objective diagnostic of midlatitude extreme weather. *Geophysical Research Letters*, 42(24).

Dee, D. P., Uppala, S. M., Simmons, A. J., Berrisford, P., Poli, P., Kobayashi, S., Andrae, U., Balmaseda, M. A., Balsamo, G., Bauer, P., Bechtold, P., Beljaars, A. C. M., van de Berg, L., Bidlot, J., Bormann, N., Delsol, C., Dragani, R., Fuentes, M., Geer, A. J., Haimberger, L., Healy, S. B., Hersbach, H., Hólm, E. V., Isaksen, L., Kållberg, P., Köhler, M., Matricardi, M., McNally, A. P., Monge-Sanz, B. M., Morcrette, J., Park, B., Peubey, C., de Rosnay, P., Tavolato, C., Thépaut, J., and Vitart, F. (2011). The era-interim reanalysis: configuration and performance of the data assimilation system. *Q. J. R. Meteorol. Soc.*, 137:553–597.

Deng, Y. and Mak, M. (2006). Nature of the differences in the intraseasonal variability of the pacific and atlantic storm tracks: A diagnostic study. *Journal of the atmospheric sciences*, 63(10):2602–2615.

Dickinson, R. E. (1968). Planetary rossby waves propagating vertically through weak westerly wind wave guides. *Journal of the Atmospheric Sciences*, 25(6):984–1002.

Dickinson, R. E. (1970). Development of a rossby wave critical level. *Journal of the Atmospheric Sciences*, 27(4):627–633.

Dritschel, D. and McIntyre, M. (2008). Multiple jets as pv staircases: the phillips effect and the resilience of eddy-transport barriers. *Journal of the Atmospheric Sciences*, 65(3):855–874.

Dritschel, D. G. (1988). The repeated filamentation of two-dimensional vorticity interfaces. *J. Fluid Mech.*, 194:511–547.

Dunn-Sigouin, E. and Son, S.-W. (2013). Northern hemisphere blocking frequency and duration in the CMIP5 models. *J. Geophys. Res.*, 118:1179–1188.

Durran, D. R. (2013). *Numerical methods for wave equations in geophysical fluid dynamics*. Springer Science & Business Media.

Eliassen, A. and Palm, E. (1961). On the transfer of energy in stationary mountain waves. *Geofysiske Publikasjoner*, 22:1–23.

Feldstein, S. B. and Held, I. M. (1989). Barotropic decay of baroclinic waves in a two-layer beta-plane model. *Journal of the Atmospheric Sciences*, 46(22):3416–3430.

Fyfe, J. and Held, I. M. (1990). The two-fifths and one-fifth rules for rossby wave breaking in the wkb limit. *Journal of the Atmospheric Sciences*, 47(6):697–706.

Hanley, J. and Caballero, R. (2012). The role of large-scale atmospheric flow and rossby wave breaking in the evolution of extreme windstorms over europe. *Geophysical Research Letters*, 39(21).

Haynes, P. H. (1988). Forced, dissipative generalizations of finite-amplitude wave-activity conservation relations for zonal and nonzonal basic flows. *J. Atmos. Sci.*, 45:2352–2362.

Held, I. M. (1983). Stationary and quasi-stationary eddies in the extratropical troposphere: Theory. *Large-scale dynamical processes in the atmosphere*, pages 127–168.

Held, I. M. (1985). Pseudomomentum and the orthogonality of modes in shear flows. *Journal of the atmospheric sciences*, 42(21):2280–2288.

Held, I. M. and Phillipps, P. J. (1987). Linear and nonlinear barotropic decay on the sphere. *J. Atmos. Sci.*, 44:200–207.

Held, I. M. and Ting, M. (1990). Orographic versus thermal forcing of stationary waves: The importance of the mean low-level wind. *Journal of the Atmospheric Sciences*, 47(4):495–500.

Held, I. M., Ting, M., and Wang, H. (2002). Northern winter stationary waves: theory and modeling. *Journal of climate*, 15(16):2125–2144.

Hodges, K. (1995). Feature tracking on the unit sphere. *Monthly Weather Review*, 123(12):3458–3465.

Hodges, K. (1999). Adaptive constraints for feature tracking. *Monthly Weather Review*, 127(6):1362–1373.

Hodges, K. I., Hoskins, B. J., Boyle, J., and Thorncroft, C. (2003). A comparison of recent reanalysis datasets using objective feature tracking: Storm tracks and tropical easterly waves. *Monthly Weather Review*, 131(9):2012–2037.

Hoskins, B. J. and Hodges, K. I. (2002). New perspectives on the northern hemisphere winter storm tracks. *Journal of the Atmospheric Sciences*, 59(6):1041–1061.

Hoskins, B. J. and Hodges, K. I. (2005). A new perspective on southern hemisphere storm tracks. *Journal of Climate*, 18(20):4108–4129.

Hoskins, B. J., James, I. N., and White, G. H. (1983). The shape, propagation and mean-flow interaction of large-scale weather systems. *J. Atmos. Sci.*, 40:1595–1612.

Hoskins, B. J. and Karoly, D. J. (1981). The steady linear response of a spherical atmosphere to thermal and orographic forcing. *J. Atmos. Sci.*, 38:1179–1196.

Hoskins, B. J., McIntyre, M., and Robertson, A. W. (1985). On the use and significance of isentropic potential vorticity maps. *Quarterly Journal of the Royal Meteorological Society*, 111:877–946.

Hoskins, B. J. and Valdes, P. J. (1990). On the existence of storm-tracks. *Journal of the atmospheric sciences*, 47(15):1854–1864.

Hovmöller, E. (1949). The trough-and-ridge diagram. *Tellus*, 1:62–66.

Huang, C. S. Y. and Nakamura, N. (2016). Local finite-amplitude wave activity as a diagnostic of anomalous weather events. *Journal of the Atmospheric Sciences*, 73(1):211–229.

Huang, C. S. Y. and Nakamura, N. (2017). Local wave activity budgets of the wintertime northern hemisphere: Implication for the pacific and atlantic storm tracks. *Geophysical Research Letters*, 44(11):5673–5682. 2017GL073760.

Hurrell, J. W. et al. (1995). Decadal trends in the north atlantic oscillation: regional temperatures and precipitation. *Science-AAAS-Weekly Paper Edition*, 269(5224):676–678.

Jones, E., Oliphant, T., and Peterson, P. (2014). {SciPy}: open source scientific tools for {Python}.

Killworth, P. D. and McIntyre, M. E. (1985). Do rossby-wave critical layers absorb, reflect, or over-reflect? *J. Fluid Mech.*, 161:449–492.

Lejenäs, H. and Økland, H. (1983). Characteristics of northern hemisphere blocking as determined from a long time series of observational data. *Tellus A*, 35A:350–362.

Lighthill, M. J. and Whitham, G. B. (1955). On kinematic waves. ii. a theory of traffic flow on long crowded roads. In *Proceedings of the Royal Society of London A: Mathematical, Physical and Engineering Sciences*, volume 229, pages 317–345. The Royal Society.

Lindzen, R. and Farrell, B. (1980). A simple approximate result for the maximum growth rate of baroclinic instabilities. *Journal of the atmospheric sciences*, 37(7):1648–1654.

Lindzen, R. S. and Tung, K. K. (1978). Wave overreflection and shear instability. *Journal of the Atmospheric Sciences*, 35(9):1626–1632.

Liu, C. and Barnes, E. A. (2015). Extreme moisture transport into the arctic linked to rossby wave breaking. *Journal of Geophysical Research: Atmospheres*, 120(9):3774–3788.

Magnusdottir, G. and Haynes, P. H. (1996). Wave activity diagnostics applied to baroclinic wave life cycles. *J. Atmos. Sci.*, 53.

Masato, G., Hoskins, B., and Woollings, T. J. (2012). Wave-breaking characteristics of midlatitude blocking. *Quarterly Journal of the Royal Meteorological Society*, 138(666):1285–1296.

McIntyre, M. and Palmer, T. (1984). The surf zonein the stratosphere. *Journal of atmospheric and terrestrial physics*, 46(9):825–849.

McIntyre, M. and Shepherd, T. (1987). An exact local conservation theorem for finite-amplitude disturbances to non-parallel shear flows, with remarks on hamiltonian structure and on arnol'd's stability theorems. *J. Fluid Mech.*, 181:527–565.

McIntyre, M. E. (1982). How well do we understand the dynamics of stratospheric warmings? *Journal of the Meteorological Society of Japan. Ser. II*, 60(1):37–65.

McIntyre, M. E. and Palmer, T. (1983). Breaking planetary waves in the stratosphere. *Nature*, 305(5935):593–600.

Methven, J. and Berrisford, P. (2015). The slowly evolving background state of the atmosphere. *Q. J. R. Meteorol. Soc.*

Nakamura, H. (1992). Midwinter suppression of baroclinic wave activity in the pacific. *Journal of the Atmospheric Sciences*, 49(17):1629–1642.

Nakamura, N. (1996). Two-dimensional mixing, edge formation, and permeability diagnosed in an area coordinate. *Journal of the atmospheric sciences*, 53(11):1524–1537.

Nakamura, N. and Huang, C. S. Y. (2017). Local wave activity and the onset of blocking along a potential vorticity front. *Journal of the Atmospheric Sciences*, 74(7):2341–2362.

Nakamura, N. and Solomon, A. (2010). Finite-amplitude wave activity and mean flow adjustments in the atmospheric general circulation. part i: Quasigeostrophic theory and analysis. *J. Atmos. Sci.*, 67:3967–3983.

Nakamura, N. and Solomon, A. (2011). Finite-amplitude wave activity and mean flow adjustments in the atmospheric general circulation. part ii: analysis in isentropic coordinate. *J. Atmos. Sci.*, 68:2783–2799.

Nakamura, N. and Zhu, D. (2010). Finite-amplitude wave activity and diffusive flux of potential vorticity in eddy-mean flow interaction. *J. Atmos. Sci.*, 67:2701–2716.

NOAA (2016). Daily nao/ao/pna index since january 1950.

Orlanski, I. (1998). Poleward deflection of storm tracks. *Journal of the atmospheric sciences*, 55(16):2577–2602.

Orlanski, I. and Katzfey, J. (1991). The life cycle of a cyclone wave in the southern hemisphere. part i: Eddy energy budget. *Journal of the Atmospheric Sciences*, 48(17):1972–1998.

Pelly, J. L. and Hoskins, B. J. (2003). A new perspective on blocking. *J. Atmos. Sci.*, 60:743–755.

Plumb, R. A. (1985). On the three-dimensional propagation of stationary waves. *J. Atmos. Sci.*, 42:217–229.

Plumb, R. A. (1986). Three-dimensional propagation of transient quasi-geostrophic eddies and its relationship with the eddy forcing of the timemean flow. *Journal of the atmospheric sciences*, 43(16):1657–1678.

Polvani, L. M. and Plumb, R. A. (1992). Rossby wave breaking, microbreaking, filamentation, and secondary vortex formation: The dynamics of a perturbed vortex. *J. Atmos. Sci.*, 49:462–476.

Randel, W. J. and Held, I. M. (1991). Phase speed spectra of transient eddy fluxes and critical layer absorption. *J. Atmos. Sci.*, 48:688–697.

Richards, P. I. (1956). Shock waves on the highway. *Operations research*, 4(1):42–51.

Riviere, G., Laine, A., Lapeyre, G., Salas-Mélia, D., and Kageyama, M. (2010). Links between rossby wave breaking and the north atlantic oscillation–arctic oscillation in present-day and last glacial maximum climate simulations. *Journal of Climate*, 23(11):2987–3008.

Schubert, S. D., Wang, H., Koster, R. D., Suarez, M. J., and Groisman, P. Y. (2014). Northern eurasian heat waves and droughts. *Journal of Climate*, 27(9):3169–3207.

Shaw, T., Baldwin, M., Barnes, E., Caballero, R., Garfinkel, C., Hwang, Y.-T., Li, C., O'Gorman, P., Rivière, G., Simpson, I., et al. (2016). Storm track processes and the opposing influences of climate change. *Nature Geoscience*.

Sillmann, J., Croci-Maspoli, M., Kallache, M., and Katz, R. W. (2011). Extreme cold winter temperatures in europe under the influence of north atlantic atmospheric blocking. *Journal of Climate*, 24(22):5899–5913.

Sobel, A. H. and Plumb, R. A. (1999). Quantitative diagnostics of mixing in a shallow water model of the stratosphere. *Journal of the atmospheric sciences*, 56(16):2811–2829.

Solomon, A. (2014). Wave activity events and the variability of the stratospheric polar vortex. *J. Climate*, 27:7796–7806.

Solomon, A. and Nakamura, N. (2012). An exact lagrangian-mean wave activity for finite-amplitude disturbances to barotropic flow on a sphere. *Journal of Fluid Mechanics*, 693:69.

Stewartson, K. (1977). The evolution of the critical layer of a rossby wave. *Geophys. Astrophys. Fluid Dyn.*, 9:185–200.

Strong, C. and Magnusdottir, G. (2008). Tropospheric rossby wave breaking and the nao/nam. *Journal of the atmospheric sciences*, 65(9):2861–2876.

Swanson, K. (2000). Stationary wave accumulation and the generation of low-frequency variability on zonally varying flows. *J. Atmos. Sci.*, 57:2262–2280.

Takaya, K. and Nakamura, H. (2001). A formulation of a phase-independent wave-activity flux for stationary and migratory quasigeostrophic eddies on a zonally varying basic flow. *J. Atmos. Sci.*, 58:608–627.

Tamarin, T. and Kaspi, Y. (2016). The poleward motion of extratropical cyclones from a potential vorticity tendency analysis. *Journal of the Atmospheric Sciences*, 73(4):1687–1707.

Tamarin, T. and Kaspi, Y. (2017). Mechanisms controlling the downstream poleward deflection of midlatitude storm tracks. *Journal of the Atmospheric Sciences*, 74(2):553–572.

Taylor, G. (1932). The transport of vorticity and heat through fluids in turbulent motion. *Proceedings of the Royal Society of London. Series A, Containing Papers of a Mathematical and Physical Character*, 135(828):685–702.

Thompson, D. W. and Wallace, J. M. (1998). The arctic oscillation signature in the wintertime geopotential height and temperature fields. *Geophysical research letters*, 25(9):1297–1300.

Thuburn, J. and Lagneau, V. (1999). Eulerian mean, contour integral, and finite-amplitude wave activity diagnostics applied to a single-layer model of the winter stratosphere. *J. Atmos. Sci.*, 56:689–710.

Tibaldi, S. and Molteni, F. (1990). On the operational predictability of blocking. *Tellus A*, 42:343–365.

Wallace, J. M. and Gutzler, D. S. (1981). Teleconnections in the geopotential height field during the northern hemisphere winter. *Monthly Weather Review*, 109(4):784–812.

Wang, L. and Nakamura, N. (2015). Covariation of finite-amplitude wave activity and the zonal mean flow in the midlatitude troposphere: 1. theory and application to the southern hemisphere summer. *Geophys. Res. Lett.*, 42(19):8192–8200.

Wang, L. and Nakamura, N. (2016). Covariation of finite-amplitude wave activity and the zonal-mean flow in the midlatitude troposphere. part ii: Eddy forcing spectra and the periodic behavior in the southern hemisphere summer. *J. Atmos. Sci.*, 73(12):4731–4752.

Warn, T. and Warn, H. (1976). On the development of a rossby wave critical level. *Journal of the Atmospheric Sciences*, 33(10):2021–2024.

Warn, T. and Warn, H. (1978). The evolution of a nonlinear critical level. *Studies in Applied Mathematics*, 59:37–71.

Wernli, H. and Sprenger, M. (2007). Identification and era-15 climatology of potential vorticity streamers and cutoffs near the extratropical tropopause. *Journal of the atmospheric sciences*, 64(5):1569–1586.

Whan, K., Zwiers, F., and Sillmann, J. (2016). The influence of atmospheric blocking on extreme winter minimum temperatures in north america. *Journal of Climate*, 29(12):4361–4381.

Williams, I. N. and Colucci, S. J. (2010). Characteristics of baroclinic wave packets during strong and weak stratospheric polar vortex events. *J. Atmos. Sci.*, 67:3190–3207.

Wilson, C., Sinha, B., and Williams, R. G. (2009). The effect of ocean dynamics and orography on atmospheric storm tracks. *Journal of Climate*, 22(13):3689–3702.